CAMBRIDGE UNIVERSITY PRESS GeologicalMagazine

Burial and exhumation history of the Daday Unit (Central Pontides, Turkey): implications for the closure of the Intra-Pontide oceanic basin.

Journal:	*Geological Magazine*
Manuscript ID	GEO-16-1583.R2
Manuscript Type:	Article
Date Submitted by the Author:	n/a
Complete List of Authors:	Frassi, Chiara; Università di Pisa, Dipartimento di Scienze della terra Marroni, Michele; Università di Pisa, Dipartimento di Scienze della Terra; Istituto di Geoscienze e Georisorse, CNR Pandolfi, Luca; Università di Pisa, Dipartimento di Scienze della Terra; Istituto di Geoscienze e Georisorse, CNR Goncuoglu, Cemal; Middle East Technical University, Department of Geological Engineering Ellero, Alessandro; Istituto di Geoscienze e Georisorse, CNR Ottria, Giuseppe; Istituto di Geoscienze e Georisorse, CNR Sayit, Kaan; Middle East Technical University, Department of Geological Engineering McDonald, Christopher ; Arizona State University, School for Earth and Space Exploration Balestrieri, Maria; Istituto di Geoscienze e Georisorse, CNR Malasoma, Alessandro; TSLab & Geoservices
Keywords:	P-T-d-t path, HP metamorphism, exhumation, Intra-Pontide suture zone, northern Turkey

Original Article for the Special Issue: *Birth and Death of Oceanic Basins*

Burial and exhumation history of the Daday Unit (Central Pontides, Turkey): implications for the closure of the Intra-Pontide oceanic basin.

Chiara Frassi[(1, *)], Michele Marroni[(1, 2)], Luca Pandolfi[(1, 2)], M. Cemal Göncüoğlu[(3)], Alessandro Ellero[(2)], Giuseppe Ottria[(2)], Kaan Sayit[(3)], Christopher S. McDonald[(4)], Maria Laura Balestrieri[(5)], Alessandro Malasoma[(6)]

[(1)] Dipartimento di Scienze della Terra, Università di Pisa, Pisa, Italy.

[(2)] Istituto di Geoscienze e Georisorse, CNR, Pisa, Italy.

[(3)] Department of Geological Engineering, Middle East Technical University, Ankara, Turkey.

[(4)] School for Earth and Space Exploration, Arizona State University, Tempe AZ 85287, USA.

[(5)] Istituto di Geoscienze e Georisorse, CNR, Firenze, Italy.

[(6)] TSLab & Geoservices, Via Vecchia Fiorentina, 10, Cascina, Pisa, Italy.

(*) Corresponding author.

Chiara Frassi. E-mail: chiararassi@gmail.com; chiarafrassi@yahoo.it

Running title: Burial and exhumation in Central Pontides

ABSTRACT

In northern Turkey, the Intra-Pontide suture zone represents one of the first-order tectonic structures located between the Istanbul-Zonguldak and the Sakarya continental terranes. It consists of an east-west trending assemblage of deformed and variably metamorphosed tectonic units, including sedimentary rocks and ophiolites derived from a NeoTethyan oceanic basin, known as Intra-Pontide oceanic basin.

One of these units is represented by the Daday Unit that consists of an assemblage of block-in-matrix derived from a supra-subduction oceanic crust and related deep-sea sedimentary cover of Middle Jurassic age. This setting has been acquired during the Late Jurassic by tectonic underplating at 35-42 km of depth associated with blueschist facies metamorphism (D1 phase). The following D2, D3 and D4 phases produced the exhumation of the Daday Unit up to shallower structural levels in a time span running from Albian to late Paleocene. The high geothermal gradient detected during the D2 phase indicates that the Daday Units was exhumed during a continent arc collisional setting. The tectonic structures of the Intra-Pontide suture zone, resulting from the previously described tectonic history, are unconformably sealed by the upper Paleocene - Eocene deposits. This tectonic setting was intensely reworked by the activity of the North Anatolian Fault Zone, producing the present-day geometrical relationships of the Intra-Pontide suture zone of central Pontides.

Keywords: P-T-d-t path, HP metamorphism, exhumation, Intra-Pontide suture zone, northern Turkey

1. Introduction

The study of the ophiolite-bearing suture zones preserved within orogenic collisional belts can provide important information on the pre-collisional geodynamic setting. They, in fact, bear fore- and back-arc ophiolite sequences (non-metamorphosed or affected by low- to high-pressure metamorphism) and/or magmatic rocks originated in a volcanic arc whose study may improve considerably the pre-collisional paleogeographic reconstructions.

The Intra-Pontide suture (IPS) zone represents one of the first-order tectonic structures in northern Turkey (Sengör & Yılmaz, 1981). It is located between the Istanbul-Zonguldak Terrane (IZ) to the north, and the Sakarya Terrane (SK) to the south (e.g. Göncüoğlu *et al.* 1997; 2000) (Fig. 1) and consists of an east-west trending assemblage of deformed and variably metamorphosed units, including sedimentary and magmatic rocks derived from a NeoTethyan oceanic basin (e.g. Göncüoğlu *et al.* 2008). Despite the IPS zone covers a key role in the Mesozoic geodynamics reconstructions for the Eastern Mediterranean region, the tectono-metamorphic history of its units of oceanic affinity has been poorly investigated.

We here present the results of a multidisciplinary research carried out on the Daday Unit from the Central Pontides (northern Turkey) introducing new constraints on the tectonic evolution of the IPS zone. This research combines lithological, structural and metamorphic investigations, and geochemical and radiometric (apatite fission track and ^{40}Ar-^{39}Ar dating) studies. The resulting dataset is discussed in order to provide new insights for the reconstruction of the tectonic history of the IPS zone in the frame of the Mesozoic-Tertiary geodynamic evolution of the eastern Mediterranean region.

2. The Intra-Pontide suture zone: an overview

The geological setting of Turkey (Fig. 1a) is characterized by an assemblage of continental terranes separated by several ophiolite-bearing suture zones whose ages range from late Neoproterozoic to Cretaceous (Göncüoğlu *et al.* 1997 and quoted references). This tectonic setting derives from the progressive accretion to the Eurasian plate of Gondwana-derived fragments as a consequence of the closure of several Paleo- and Neo-Tethyan oceanic basins (e.g. Göncüoğlu *et al.* 1997). The result is an assemblage of continental terranes bounded by suture zones of different ages that marks the areas where the Paleo-Tethyan and Neo-Tethyan oceanic basins were opened and subsequently destroyed by subduction and/or obduction processes (e.g. Okay & Whitney, 2010). The IPS zone is one of these ophiolitic-bearing suture zones. It is an assemblage of oceanic and continental units, extending more than 400 km in Northern Turkey from the Aegean Sea to the Black Sea (Sengör & Yılmaz 1981; Göncüoğlu *et al.* 1997; Robertson & Ustaömer 2004) (Fig. 1a).

The published data (Sengör & Yılmaz, 1981; Göncüoğlu *et al.* 1987, 2008, 2012, 2014; Yılmaz 1990; Göncüoğlu & Erendil 1990; Robertson *et al.* 1991; Okay *et al.* 1996; Yılmaz *et al.* 1997; Okay & Tüysüz 1999; Okay 2000; Robertson & Ustaömer 2004; Akbayram *et al.* 2013; Marroni *et al.* 2014) indicate that the IPS zone was formed by the closure of an oceanic basin, known as the Intra-Pontide Ocean (IPO) basin, located between two continental margins today represented by the IZ Terrane, to the north, and the SK Terrane, to the south (Fig. 1a). The IPO basin was opened in the Middle Triassic time (Tekin *et al.* 2012) and was characterized since Middle Jurassic by supra-subduction oceanic lithosphere (Göncüoğlu *et al.* 2012). The final closure of the Intra-Pontide oceanic basin leading to the collision between Istanbul-Zonguldak and Sakarya terranes was recently constrained before late Paleocene in central Pontides (Catanzariti *et al.* 2013) whereas before the Santonian in the Marmara region (Özcan *et al.* 2012; Akbayram *et al.* 2013). Since the late Miocene, the IPS zone has been overprinted by the North Anatolian Fault (NAF) zone, a still active transform fault characterized by a wide damage zone that almost completely obliterate the pristine

architecture of the IPS zone (e.g. Ellero *et al.* 2015a). Where the original structure of the IPS zone is preserved the tectonic units are bounded by east-west trending, low-angle shear zones (e.g. Frassi *et al.* 2016).

The assemblage of tectonic units belonging to the IPS zone is thrusted by the IZ Terrane that includes a Neoproterozoic basement (e.g. Ustaömer & Rogers, 1999) unconformably overlain by a continuous, very thick sedimentary sequence spanning from Ordovician to Carboniferous (e.g. Görür *et al.* 1997). The non-metamorphic Paleozoic sequence of the IZ Terrane (i.e. the Zonguldak Unit) is in turn unconformably overlain by a thick sequence of upper Permian-Triassic continental clastic deposits topped by Middle to Upper Jurassic carbonate deposits. They are in turn covered by Upper Cretaceous–Paleocene turbidite deposits (Akveren Flysch) interleaved with andesitic volcanic flows (e.g. Dizer & Meriç, 1983; Aydın *et al.* 1986).

In turn, the units from the IPS zone and the IZ Terrane are thrust on the SK Terrane consisting of a Variscan continental basement associated with a strongly deformed and metamorphosed Triassic subduction complex (i.e. the Karakaya Complex) which is unconformably covered by a non-metamorphic Lower Jurassic - middle Paleocene sedimentary cover. The lower portion of the Karakaya Complex was deformed and metamorphosed (from blueschists to eclogite facies conditions) during the Upper Triassic (Okay & Monié, 1997; Okay *et al.* 2002). The deformation and metamorphism documented in the Karakaya Complex testify the subduction of the PaleoTethys oceanic lithosphere mainly below the Laurasia continental margin during the 'Cimmerian orogeny' (e.g. Robertson & Ustaömer, 2011). The resulting tectonic structures are unconformably sealed by Lower Jurassic continental to shallow-marine clastic rocks. They are in turn unconformably topped by Middle Jurassic to Lower Cretaceous neritic carbonates and Albian-Cenomanian pelagic limestones passing upward to turbidite deposits (here reported as Tarakli Flysch) ranging in age from early Maastrichtian to middle Paleocene. The uppermost levels of the Tarakli Flysch

show carbonate and ophiolite slide-blocks derived from both IZ Terrane and IPS zone (Catanzariti *et al.* 2013). The geological time scale follows the International Chronostratigraphic Chart v2016/04 (Cohen et al., 2013, updated)

3. A snapshot of the Intra-Pontide suture zone in the Central Pontides

In the Central Pontides, the IPS zone is an assemblage of several tectonic units characterized by different age, metamorphic imprint and deformation history (Fig. 1b). The present-day tectonic setting can be described as a pre- late Paleocene imbricate stack where an ophiolite unit (Ayli Dağ ophiolite Unit) and an ophiolite-bearing mèlange (known with different names: Kirazbasi by Tüysüz 1990; Araç Formation by Ozcan *et al.* 2007 and Arkot Dağ Mèlange by Tokay, 1973, Göncüoğlu *et al.* 2014) are associated with four metamorphic units (Fig. 1b). In the pristine tectonic setting, the ophiolite unit and the ophiolite-bearing mèlange were probably at the top of the imbricate stack, above the metamorphic units.

The Ayli Dağ ophiolite Unit is characterized by a Middle Jurassic back-arc ophiolite sequence (Göncüoğlu *et al.* 2012) whereas the ophiolite-bearing mèlange is a sedimentary mèlange characterized by slide blocks of continental and oceanic origin set in a Upper Cretaceous sedimentary matrix. The four metamorphic units (i.e. Central Pontide Structural Complex CPSC by Tekin *et al.* 2012 or Central Pontides Supercomplex, CPS, by Okay *et al.* 2013; hereafter both referred as CPSC, Fig. 1b) are characterized by fragments of oceanic lithosphere deformed and metamorphosed in a subduction setting (e.g. Okay *et al.* 2006; 2013; Marroni *et al.* 2014, Aygül *et al.* 2015a).

The metamorphic unit affected by the highest metamorphic grade (i.e. Domuz Dağ Unit; Okay *et al.* 2006) is an assemblage of slices of metasedimentary rocks, metabasites and metaserpentinites cropping out in the Kargi Massif (Fig. 1b). The metabasites include eclogites, garnet- and glaucophane-bearing amphibolites and albite- and chlorite- bearing

schists. On the basis of ^{40}Ar-^{39}Ar dating the eclogite facies metamorphism took place in the Early Cretaceous (~105 Ma, Okay *et al.* 2006). A second high-grade metamorphic unit is represented by the Saka Unit (cf. the Devrekani Unit of Marroni *et al.* 2014 and Saka Complex of Okay *et al.* 2013). This unit, less than 300 m in thickness, was recognized exclusively in the Daday Massif (Figs. 1b, 2). It consists of slices of garnet-bearing amphibolites (affected by a retrograde metamorphism ranging from greenschist to sub-greenschist facies conditions; Marroni *et al.* 2013), coarse-grained banded amphibolites, garnet-bearing micaschists and coarse-grained impure marbles. In the garnet-bearing amphibolites P = 0.8-0.99 GPa and T = 600 °C calculated at metamorphic peak occurred during Late Jurassic (~163Ma: ^{40}Ar-^{39}Ar dating, Marroni *et al.* 2014). The third metamorphic unit is represented by the Daday Unit (cf. Martin Complex of Okay *et al.* 2013) that is described in detail in the sections below. The Emirköy Unit represents the fourth metamorphic unit of the CPSC. It is made by a monotonous succession of metaturbidites affected by very low-grade metamorphic conditions. No ophiolite bodies and/or clasts have been found in this unit. The upper Paleocene- middle Eocene shallow-water deposits of Karabük-Kastamonu Basin (Ozcan *et al.* 2007) unconformably sealed the relationships among the metamorphic units of the CPSC, the Ayli Dağ ophiolite Unit and the Arkot Dağ Melange.

It is important to outline the sharp metamorphic gap existing among the non-metamorphosed Ayli Dağ ophiolite Unit and the Arkot Dağ Melange, and the four metamorphic units. This gap clearly indicates the association in the same tectonic stack of tectonic units deformed and metamorphosed at different structural levels.

In addition, a weakly metamorphosed volcanics-bearing succession was documented within elongated blocks bounded by strike-slip faults along the NAF zone south of Tosya (the Tafano Unit: Ellero *et al.* 2015b; Fig. 1b). This unit consists of basalts to basaltic andesites topped by uppermost Santonian-middle Campanian turbidites. The geochemistry of the volcanic rocks (Ellero *et al.* 2015b; Sayit *et al.* 2016) indicates that this succession represents

the remains of a continental arc, whose palaeographical location inside the IPO domain is still undetermined. Moreover, in another block along the NAF zone, Berber *et al.* (2014) and Aygül *et al.* (2015b) documented a succession consisting of Cenomanian - Turonian andesites and sedimentary rocks, metamorphosed during the Maastrichtian under low greenschist facies conditions. On the whole, the picture arising from the IPS zone seems to indicate the occurrence of elements of a convergent margin whose geodynamic history is still matter of debate.

4. The Daday Unit

In the Daday Massif (north-central Turkey; Fig. 1b), the easternmost segment of the IPS zone crops out in the mountains between Daday town, in the north, and Hatipköy and Cavusköy, in the south (Fig. 2). In this area, the metamorphic units of the IPS zone are imbricated with slices of the Ayli Dağ ophiolite Unit and the Arkot Dağ Mélange (Tokay, 1973) onto the Tarakli Flysch (Late Cretaceous-middle Paleocene age: Catanzariti *et al.* 2013) that represents the sedimentary cover of the SK Terrane (Fig. 2). In turn, the units from IPS zone are topped by klippens of the IZ Terrane as documented *c.* 20 km east of Araç. The uppermost Paleocene – middle Eocene deposits of Karabük-Kastamonu basin seal the relationships among the IZ and SK terranes and the IPS zone. Two different metamorphic units crop out in the study area: the Saka Unit and the Daday Unit. The latter is the object of this study and is described in detail in the two sections below: in the first section, we present the results of our lithological, geochemical and structural investigations whereas in the second, we reconstruct its pressure-temperature-time (P-T-t) path using new pressure-temperature estimates and new ^{40}Ar-^{39}Ar and apatite fission track (AFT) ages.

4.a. Lithological and structural overview

The study of the Daday Unit started with classical field investigations during which we conducted a detailed description of lithotypes and mesostructures as well as the measurements of the different structural elements (e.g. foliations, folds, mineral lineations and faults) (Figs. 2 and 3). A total of 45 samples, representative of each lithotype and fabrics, were collected in the Daday Unit. They were cut parallel to the mineral lineation and orthogonal to the main foliation and investigated using a polarized light microscopy.

Five samples of mafic rocks were selected to conduct geochemical analyses (see Fig. 2 for sample location and Supplementary Material S2 for GPS coordinates) (Sayit *et al.* 2016). Analyses of major elements were determined by inductively coupled plasma emission spectrometry (ICP-ES) and trace elements (including REE-rare earth element) were determined by inductively coupled plasma mass spectrometry (ICP-MS) at the ACME analytical labs (Canada) (see Supplementary Material S3 for geochemical analyses).

4.a.1. Lithological overview

In the field, the Daday Unit is characterized by a block-in-matrix fabric derived from a strong partitioning of the ductile deformation (D2 phase, see section below). The result is in an assemblage of m- to km-thick tectonic slices with a lozenge shape, bounded by ductile to brittle-ductile shear zones. The tectonic slices have a monogenic composition that consists of different lithotypes including fine-grained micaschists (~35%vol) (Fig. 4a), fine- to coarse-grained paragneisses (~25% vol), (impure) marbles (~20%vol) (Fig. 4b), actinolite-bearing schists (~15% vol) (Fig. 4c) and dark to white quarzites (~5% vol) (Fig. 4d). The protoliths of the fine-grained micaschists and the fine- to coarse-grained paragneisses are shales, siltites and arenites, whereas those of the actinolite-bearing schists are mafic rocks. The protoliths of the fine-grained dark and thin-bedded quartzites are probably represented by cherts whereas those of white, thick-bedded quartzites display typical stratigraphic, micro-textural and mineralogical features of quartz-arenites. No fossils were found in the sedimentary rocks of

the Daday Unit. However, U-Pb dating of detrital zircons obtained by Okay *et al.* (2013) from a sample of paragneiss suggests minimum depositional age of 171Ma.

The mylonitic foliation within the shear zones bounding the tectonic slices is the main foliation documented in the field (i.e. S2 foliation, see section below). As a consequence, the original relationships among the different lithotypes cannot be detected. Non-deformed and non-metamorphosed basic dykes intrude the metamorphic rock assemblage.

The field distribution of the different lithotypes is not homogenous across the whole study area and often the thickness of the tectonic slices is too small to be represented in the map. As a consequence, in Fig. 2 we represented only the biggest bodies of marbles and actinolite-bearing micaschists.

4.a.2. Geochemistry of the metamorphic mafic rocks

The immobile element systematics indicates that the protoliths of the metamorphic mafic rocks sampled in the study area (see Fig. 2 for sample location) are of basaltic composition and display subalkaline characteristics (Nb/Y = 0.07-0.27) (Fig. 5). The trace element characteristics further reveal that the protoliths can be subdivided into two distinct chemical types. The first type (Type 1) is characterized by the highly depleted HFSE (high field strength elements) concentrations, reflecting boninitic, island arc basalt (IAB)-like characteristics (Zr_M = 0.07-0.22, Hf_M = 0.1-0.2, Y_M = 0.06-0.27, where 'M' denotes normal mid-ocean ridge (N-MORB)-normalized) (Fig. 6). The second type (Type 2) displays BABB-like features, as reflected by N-MORB-like HFSE and HREE (heavy rare earth element) distribution associated with negative Nb anomaly (Nb/Nb* = 0.5-0.6) (Fig. 6).

The presence of these distinct chemical types within the Daday Unit may be attributed to derivation at distinct mantle source regions and/or various degrees of partial melting. Type 1, with highly depleted HFSE features, requires a mantle source that has experienced a previous melt extraction. Type 2, with relatively more enriched signatures compared to the

former group, reflects a mantle source region relatively similar to that of N-MORBs (i.e. depleted asthenospheric mantle source). The extreme depletions reflected by Type 1 Daday metamorphic mafic rocks are typical in boninitic magmas generated largely in the fore-arc regions of oceanic arcs (e.g. Crawford *et al.* 1981; Cameron *et al.* 1983; Bedard, 1999). The trace element signatures of Type 2 samples, on the other hand, appear to be similar to the magmas formed at back-arc regions of intra-oceanic subduction systems (e.g. Pearce *et al.* 2005).

4.a.3. Deformation history

The oldest deformation phase recognized in the field, D1 phase, is testified by S1 continuous foliation folded by rare centimetre-sized F2 isoclinal folds. At the microscopic scale, S1 foliation was documented within D2 microlithons in the fine-grained micaschists, paragneisses and marble. In fine-grained micaschists, it is highlighted by 1 to 3 mm-thick granoblastic layers made by elongate quartz and feldspar grains and oxides and less than 1 mm-thick lepidoblastic layers of white micas (phengite) and chlorite crystals (70-120 μm) (Fig. 7a-c) whereas in the actinolite-bearing schists and impure marbles is marked by 60-130 μm white micas and chlorite flakes oriented and/or folded at high angle respect to the external S2 foliation (Fig. 7b).

The second deformation phase (D2) produced the main structures documented in the field and results strongly partitioned in folded and sheared domains. The latter are localized at the boundaries of the lozenge-shape tectonic slices, so at the boundaries between the different lithotypes, whereas the formers are preserved within each slices. The mylonitic domains are marked by cm-scale S-C structures pointing to a top-to-the S sense of shear. Tight to isoclinal F2 folds, well developed within fine-grained micaschists and paragneisses, have symmetric profile with thickened hinge, thinned and delaminated limbs and sub-rounded up to sub-angular hinges profile (Fig. 7c). A2 fold axes mostly trends from NW-SE to NNE-SSW with a

main trend of 115-140° plunging 20-40° toward SW (Fig. 2). The main D2 structure documented in the field is the S2 foliation (Fig. 4). It develops heterogeneously as axial plane and mylonitic foliation and shows variable orientation from W-E to SW-NE and dips mainly toward west (Fig. 2). Along the limbs of the F2 folds, the parallelism between S1 and S2 foliation leads to a composite foliation whereas in the hinge zone, the S2 axial plane foliation wraps relicts of S1.

In marble, S2 foliation is highlighted by spaced (from 0.2 to 0.5 cm) fractures and/or pressure solution surfaces. At the microscopic scale, in fine-grained micaschists S2 foliation is a continuous foliation highlighted by compositional layers made of very fine-grained muscovite ± rutile (± chlorite) and quartz + albite ± calcite ± chlorite. In paragneisses, it is marked by an irregular network of 100 µm -thick layers of white mica and rutile wrapping quartz + feldspar aggregates and quartz (0.5-2 mm) grains. Quartz shows undulatory extinction, deformation bands, rare shape preferred orientation and evidences of both subgrains rotation and grain boundary migration intracrystalline recrystallization. In impure marbles, S2 foliation is marked by less than 80 µm -thick discontinuous layers of fine-grained white micas (phengite and chlorite), oriented calcite crystals (30-50 µm) and locally, irregular and discontinuous dark seems of oxides and insoluble materials along dissolution surfaces. In impure marbles, quartz shows evidences of weak intracrystalline deformation with undulatory extinction, deformation bands and evidences of subgrain rotation and dynamic recrystallization. In actinolite-bearing micaschists, S2 foliation is a continuous foliation marked by chlorite + actinolite + epidote ± ilmenite and elongated quartz and albite grains (Fig. 7d, e). It wraps relicts of brown amphibole, pyroxene, plagioclase (Fig. 7d), kinked muscovite and rare biotite (almost completely replaced by chlorite), ranging in size from 100 to 400 µm. Quartz shows both shape and crystal preferred orientation, a bimodal grain size distribution, undulatory extinction, deformation bands and evidences of subgrains rotation recrystallization, indicating deformation temperatures of 400-500°C (Stipp et al., 2002).

D3 phase is mainly represented by cylindrical F3 folds that show interlimb angles ranging from 30° to 120° and sub-angular to sub-rounded hinge zones (Fig. 7f-h). Within schists/paragneiss multilayers (i.e. metaturbidites), they can be classified as types 3 and 1B folds (Ramsay 1967). The $L_{(S0-S3)}$ intersection lineation is mainly represented by S3 foliation-S0 bedding intersection and mullion structures. A3 fold axis trend mainly from NW-SE to NNW-SSE, steeply plunging (50-80°) mainly toward SW (Fig. 2). S3 foliation is a spaced axial plane crenulation cleavage (Fig. 7g) mainly oriented NNE-SSW to NE-SW with gently dip (<20°) mainly toward SE (Fig. 2). At the microscopic scale, it is marked by rough to smooth cleavage domains highlighted by thin films of opaque minerals and oxides along dissolution surfaces (Fig. 7g). No evidence of mineralogical lineation has been detected on the S3 foliation. F3 folds are associated with ~WNW-ESE-trending thrusts dipping from 20° to 60° toward north associated to cm-thick brittle shear zones pointing to top-to-the S sense of shear.

The D4 phase produced parallel folds (type 3, Ramsay, 1967) with interlimb angles ranging from 160° to 80° and rounded hinges (Fig. 7h). They show sub-horizontal axial planes and A4 axis variably trending from W-E to NW-SE shallow plunging mainly toward W. The axial plane foliation is represented by a disjunctive cleavage without sin-kinematic re-crystallization (Fig. 7g). Associated with F4 folds, extensional brittle shear zones reactivated the pre-existing D3 thrusts indicating a top-to-the N sense of shear.

The last deformation phase, D5, was documented only at the map scale. It produced kilometre-scale open folds with sub-vertical axial plane and ~ NNE-SSW trending axes (Figs. 2 and 3). They are associated to high-angle strike-slip or oblique faults belonging to the Araç Fault zone (Ellero *et al.* 2015a) that dissect both the tectonic nappe stack and the Eocene deposits (Figs. 2 and 3). The main fault system is represented by dextral faults oriented ~WSW-ENE that result dissected by antithetical faults oriented ~NNE-SSW. A minor fault

system is directed ~WNW-ESE. Locally, N-dipping low-angle thrust faults where documented in the Eocene deposits in the north of Siragömü Village.

4.b. Constraining the P-T-t path of the Daday Unit

Thin sections obtained from the collected samples were used to investigate the relationship between deformation and metamorphism. In order to characterize the mineral chemistry of equilibrium phase assemblages, three samples were selected and investigated using a JEOL JXA-8200 Super Probe electron microprobe (EMP), equipped with four wavelength-dispersive spectrometers located at the Dipartimento di Scienze della Terra – Università di Milano, Milano (Italy). Chemical composition of chlorites and white micas were used to obtained chlorite-phengite multi-equilibrium thermodynamic calculations on one selected samples (see Table 2 for representative analyses).

In order to constrain the age of metamorphism, ^{40}Ar-^{39}Ar analyses were conducted on two white micas separates (see Fig. 2 for samples location) at Group 18 Laboratories of the Arizona State University (USA). Finally, one sample from the Daday Unit and one sample from the Saka Unit were selected to constrain the final stage of uplift using apatite fission tracks (AFT) data performed at the CNR-IGG Pisa laboratory (Italy). For further information about the used methodology and for the complete dataset (mineral chemistry, pressure-temperature estimates, ^{40}Ar-^{39}Ar data and AFT results) see online Supplementary Material at http://journals. cambridge. org/geo.

4.b.1. Mineral chemistry

The three samples selected for mineral chemistry analysis are: a fine-grained micaschist (sample TC57), an impure marble (sample TC84) and an actinolite-bearing schist (sample TC83) (see Fig. 2 for samples location and Supplementary Material S2 for GPS coordinates). In metasediments, the metamorphic assemblage associated with the S1 foliation is made up of

quartz + phengite + chlorite ± albite, meanwhile in metabasites the metamorphic assemblage is hornblende + plagioclase + phengite + chlorite ± biotite. The S2-related assemblage is composed of quartz + phengite + chlorite ± albite ± calcite and actinolite + epidote + quartz + phengite + chlorite ± albite ± ilmenite in the metasedimentary (TC57-TC84) and mafic rocks (TC83), respectively.

Chlorite (Chl): chlorite structural formulae were calculated on the basis of 14 oxygens and Fe content is shown as divalent (Fe_{tot}) (Supplementary Table S1 and S4). Chlorites from sample TC84 have high clinochlore- daphnite end-members contain respect to those in sample TC57 (See Supplementary Table S4). In the same sample, they have Si contents between 2.58 and 2.77 apfu and $Mg/(Mg+Fe^{2+}+Mn)$ ratios ranging from 0.49 to 0.55 (Fig. 8a; Supplementary Table S4). Chlorites from sample TC57 has Si contents between 2.59 and 3.06 apfu (atom per formula unit) and $Mg/(Mg+Fe^{2+}+Mn)$ ratios ranging from 0.39 to 0.49 (Supplementary Table S4). Chlorites grew along the S1 foliation have high amesite end-member contain and higher Si content (2.69-2.76 apfu) respect to those grew along the S2 foliation (Table 2; See Supplementary Table S4).

Phengite (Phe): Phengite structural formulae were calculated assuming 11 oxygens and all Fe as Fe^{2+} (Supplementary Table S1 and S4). If a small proportion of the Fe in phengite was Fe^{3+}, there would be a slight decrease in the Si content in the range typically <0.1 atoms per formula unit (apfu) relative to the Fe^{3+}- free case (e.g. Tribuzio & Giacomini, 2002). Phengites in sample TC84 have higher celadonite end-member contents relative to muscovite end-member respect to phengites in sample TC57 (Fig. 8b; Table 2). They show slightly higher Si contents (3.00-3.37 apfu) in sample TC84 whereas Si contents between 3.00 and 3.19 apfu in sample TC57 (Supplementary Table S4). Moreover, in each sample, the phengite is not arranged in clusters with different composition but are distributed on a continuous range. Phengites grew along the S1 foliation have slight higher muscovite end-member contain and slight higher Si content (3.30-3.39 apfu) respect to those grew along the S2

foliation (Fig. 8b; Table 2).

Other minerals: from actinolite-bearing schist (sample TC82) albite, amphibole and epidote were analysed. All analysed albite, which structural formulae were calculated assuming 8 oxygens, has compositions close to the pure end-member. For the analysed amphiboles structural formulae were calculated assuming 23 oxygens (See Supplementary Table S1), and the classification of Leake *et al.* (1997) was adopted. Site assignment and ferric iron contents were calculated using the scheme proposed by Schumacher in Leake *et al.* (1997). The analysed amphiboles on the main foliation are actinolite with $Mg/(Mg+Fe^{2+})$ ratios ranging from 0.51 to 0.74 and are characterized by Si contents ranging from 7.51 to 7.83 apfu. Analysed relicts of brown amphibole show core to rim zonation, with Mg-hornblende / Mg-tschermakite cores and actinolite rims. Mg-hornblende/Mg-tschermakite shows $Mg/(Mg+Fe^{2+})$ ratios ranging from 0.72 to 0.95 and Si contents ratios ranging from 6.33 to 6.57 apfu. Actinolite rims shows $Mg/(Mg+Fe^{2+})$ ratios ranging from 0.63 to 0.65 and Si contents ratios ranging from 7.59 to 7.60 apfu. For the analysed epidotes structural formulae were calculated assuming 12.5 oxygen and all Fe as Fe^{3+}. The pistacite component in the epidote ranges from 0.12 and 0.14.

4.b.2. Metamorphic evolution

Sample TC84 (impure marble) was selected for the chlorite-phengite multi-equilibrium thermodynamic technique (Vidal & Parra, 2000; for analytical description see Supplementary Material S1 whereas for pressure and temperature estimates see Supplementary Material S6 at http://journals. cambridge. org/geo). In this sample several chlorite-phengite pairs, both on the S1 and on the S2 foliation were preliminary selected using classical textural and microstructural criteria (e.g. minerals in contact, no evidence of reaction, grown in the same microstructure). In order to eliminate mineral compositions that do not form a linear

combination of the end-members used in the chlorite - white mica solid-solution models a further selection was made on the basis of the chemical criteria.

Pressure-temperature conditions at the Chl-Phe-Qtz-H_2O equilibrium were estimated using different chlorite-phengite pairs from sample TC84 (Fig. 9 and Supplementary Material S5). If σP > 0.08GPa and/or σT > 25°C the assemblages are considered to be out of equilibrium and the P-T estimates are rejected. The P-T points constrained by the composition of selected chlorite-phengite pairs define a continuous trend in the diagram, characterized by temperatures ranging from ~220 to ~500°C and pressures ranging from ~1.30 to ~0.55 GPa (Fig. 9). The Chl-Phe pairs grew along the S1 foliation constrain a P-T path (Fig. 9) characterized by a very low-temperature metamorphic gradient (~6-12°C/km) whereas the Chl-Phe pairs grew along the S2 foliation define a path characterized by an increase in temperature (up to ~500°C), associated to a decrease of pressure (up to ~0.55GPa). Therefore, the continuous trend shown by the points in the P-T diagram (Fig. 9) probably defines the exhumation path of the rocks belonging to the Daday Unit from the blueschist facies (D1 phase) to medium/high-pressure and medium temperature conditions typical of the greenschist-lower pressure epidote blueschist facies, D2 phase; Fig. 9). In the actinolite-bearing schists, the presence of Mg-hornblende/Mg-tschermakite, crystals partly replaced by actinolite rims, associate to chlorite, epidote, quartz and rare albite is consistent with the metamorphic facies obtained by thermodynamic calculations.

4.b.3. ^{40}Ar-^{39}Ar metamorphic ages and apatite fission tracks

To constrain the age of metamorphism, we performed ^{40}Ar-^{39}Ar step-heating analysis of two metamorphic white micas separates obtained from samples 4-5-12 and 8-7-11 (see Fig. 2 for location and Supplementary Material S1, S2 and S6). In both samples, the main foliation is a S2 continuous foliation marked by fine-grained white micas ± rutile (±chlorite) layers wrapping irregular sub-millimetre-thick layers of quartz, albite and relicts of large (80-

160μm) white mica preserved within D2 microlithons and oriented at high-angle respect to the external S2 foliation (i.e. marking the S1 foliation). Large white micas separates gave Late Jurassic ages ranging from *c.* 151 to *c.* 158 Ma (Fig. 10). ^{40}Ar-^{39}Ar white micas plateau age is constrained at 156.66±0.46 Ma and 157.7±2.0Ma for sample 8-7-11 and 4-5-12, respectively (base of the Kimmeridgian age, Figs. 10a, c). In sample 4-5-12, excluding the first three steps, the remains give a well-defined linear array (MSWD = 0. 81) in the ^{36}Ar-^{40}Ar *vs* ^{40}Ar-^{39}Ar isochron plot, with an intercept age is 157.6±3.4 Ma (Fig. 10b).

To constrain the exhumation of the Daday Unit at shallower structural levels, we performed apatite fission-track on two samples, one from a garnet micaschist (FT4) and one from a metarenite (FT6) (see Fig. 2 for sample location and Supplementary Material S1, S2 and S7). They yielded central ages of 57.7±3.8Ma and 58.0±4.4Ma, respectively (Fig. 11). We manage to measure a consistent number of confined track lengths (>50) in both samples with a mean length of 14.15±0.23μm and 13.53±1.43μm, respectively. Dpar is 1.9±0.42 μm and 2.0±0.33 μm, respectively. There is no noticeable correlation between single grain ages and Dpar.

Thermal history reconstructions were performed using inverse modelling of the fission-track data (Gallagher 1995; Ketcham *et al.* 2000; Ketcham 2005) with HeFTy program (Ketcham *et al.* 2007). The inverse modelling of the data resulted in a history of rapid cooling across the partial annealing zone (PAZ, between 60°C and 120°C) of the apatite fission-track system approximately placed between 65 and 55 Ma.

5. Discussion

5.a. The Daday Unit: a fragment of a suprasubduction oceanic crust of Jurassic age

The collected data indicate that the Daday Unit consists of an assemblage of slices of both metasedimentary and metabasic rocks. The occurrence of boninitic and BABB-type signatures

in the studied samples indicate that the metabasites in the Daday Unit are fragments of an intra-oceanic arc-basin system. However, to fully characterize the ophiolitic metabasic rocks from the Daday Unit, the geochemical data collected in the Daday Massif are jointed with those collected by Sayit *et al.* (2016) in the Daday Unit cropping out in the Tosya area (Fig. 1b). In this area, BABB-type signatures still exist, with Nb anomalies (Nb/Nb* = 0.3-0.6: Sayit *et al.* 2016, Fig. 4) encompassing the range observed in the Araç region. It must be noted, however, that the Tosya region comprises also E-MORB- and OIB-like samples, which are not found in the Araç area. The E-MORB-type samples are characterized by higher Th, Nb and LREE (light rare earth element) concentrations relative to N-MORB (Th_M = 4.2-10.0, Nb_M = 2.2-4.3, La_M = 2.4-3.4) (Fig. 5). The OIB-type, which is represented by a single sample of alkaline composition, displays significant enrichment in incompatible elements and fractionated LREE/HREE patterns ($[Ce/Yb]_N$ = 9.2) (Fig. 5). The E-MORB-like characteristics may have been derived from N-MORB source region with relatively low-degrees of partial melting. Alternatively, an enriched source may have been involved and mixing of melts deriving from such enriched source and those from depleted mantle may have occurred at various proportions to create E-MORB-like melts. The OIB-type signatures, on the other hand, require predominant contribution of melts derived from an enriched mantle source. To summarize, the geochemical characteristics of metabasic rocks from Daday Unit imply the occurrence of remnants of an ancient arc-basin system (Sayit *et al.* 2016). The E-MORB- and OIB-like signatures found outside the Daday Massif may also have been generated in the same arc-basin system (e.g. Leat *et al.* 2000; Hickey-Vargas *et al.* 2006).

The metasedimentary rocks of the Daday Unit derive from a succession consisting of cherts, shales, siltites, quartz-arenites and limestones. Although their pristine relationships cannot be clearly reconstructed, the interfingering relationships between micaschists and paragneisses indicate a primary association. The pristine relationship existing between the different lithotypes was observed outside the mapped area where actinolite-bearing schists

(i.e. meta-basalts) are found associated to meta-cherts and meta-volcaniclastic rocks (Fig. 12). These data indicate that the crustal section from which the metamorphic rocks of the Daday Unit derived was characterized by basic volcanic rocks of oceanic crust origin with cherts (and thin intercalation of volcaniclastic rocks) and topped by limestones (i.e. marble) grading upward to shales and arenites, probably representing turbidite deposits (i.e. micaschists, fine- to coarse-grained paragneisses; Fig. 12)

Since no paleontological ages are available for the metasedimentary succession of the Daday Unit, its deposition age can be ascertained by the geochronological data. The findings in the paragneisses of detrital zircons of Early Jurassic age (Okay *et al.* 2013) and the Late Jurassic age of the D1 phase, constrain the age of the metasedimentary rocks to Middle Jurassic. On the whole, the succession from which the metamorphic rocks of the Daday Unit derived can be described as an oceanic crust and related deep-sea sedimentary cover of Middle Jurassic age.

5.b. Pressure-temperature-time-deformation (P-T-t-D) path of the Daday Unit: tectonic underplating and subsequent exhumation during the Late Jurassic and Early Cretaceous time span.

The rare findings of isoclinal F1 folds as well as the scattered occurrence of the relicts of S1 foliation hamper the full reconstruction of primary features of the D1 phase. Thus, the significance of the D1 phase can be hypothesized only taking into account the P-T conditions estimated using the metamorphic mineral paragenesis that grew along the S1 foliation. Pressure and temperatures estimates indicate that D1 phase were acquired during lower blueschist metamorphic facies conditions (T ≈ 220-420 °C, P ≈ 1.0-1.3 GPa) at depth of ~35-44km. ^{40}Ar-^{39}Ar dating on white mica indicate that this event occurred during the Lower Jurassic (157.6 ± 3.4 Ma) (Fig. 13a). These data suggest that the D1 deformational phase was

acquired at pressure-peak during the accretion of the Daday Unit to an accretionary wedge in a subduction setting.

The D2 phase is characterized by tight to isoclinal F2 folds and by a pervasive S2 foliation that developed both as axial plane surface or as mylonitic foliation along the shear zones located at the boundary of each tectonic slices that show a general top-to-S sense of shear. Thermodynamic calculations conducted on chlorite-phengite pairs that grew in equilibrium along the S2 foliation indicate that the D2 phase was acquired during metamorphic conditions typical of greenschist facies - low-pressure epidote-blueschist facies (Fig. 9; T ≈ 400-480 °C, P ≈ 0.55-1.1 GPa) at depth of ~37-17km (Figs. 9, 13a). The age of the D2 phase can be tentatively determined according to the ^{40}Ar-^{39}Ar ages provided by Okay *et al.* (2013) for the Martin Complex, corresponding in the study area, to the Daday Unit. These authors obtained the age of 107 ± 4 Ma (Albian, Lower Cretaceous) for fine-grained white micas grown along a pervasive foliation that can be tentatively interpreted as related to the D2 phase. The DDU was so exhumed from ~44-35km to ~37-17km of depth in a period of time of *c.* 50Ma implying a roughly mean vertical exhumation rate of ~ 0.25 mm/yr during Upper Jurassic to Lower Cretaceous (i.e. Albian).

Since the boundaries between the different tectonic units as well as the boundaries between different tectonic slices within the Daday Unit are marked by the S2 foliation (the main foliation documented in the field), the stacking of metamorphic and non-metamorphic (Arkot Dağ Mèlange and Ayli Dag ophiolite Unit) units of the IPS zone in the Daday Massif probably started during the late stage of D2 phase. The subsequent D3 phase produced a composite fabric acquired during ductile-brittle to brittle deformation regimes. The main structures are represented by low-angle thrusts with a to top-to-the S sense of shear and by F3 folds. The D3 thrusts promote and emphasize the imbrication of the Daday Massif nappe stack.

The open recumbent F4 folds and the low-angle normal faults produced during the D4 phase were originated from vertical shortening of pre-existing non-horizontal layers during an extensional tectonics due to the gravitational collapse of over-thickened orogenic wedge (Froitzheim 1992, Wheeler & Butler 1994). The brittle low-angle extensional shear zones produced during the D4 phase reworked the top-to the S thrusts produced during the D3 phase. These structures occurred at shallower structural levels (<5-10km of depth) and are sealed by the upper Paleocene-middle Eocene deposits of the inter-mountain Karabük-Kastamonu basin (Tüysüz 1999; Hippolyte *et al.* 2010). In this reconstruction, the apatite fission-track ages of ~58Ma (late Paleocene) may constrain the final stages of the D4 phase and the last episodes of uplift before the deposits of the inter-mountain Karabük-Kastamonu basin and the inception of NAF activity. The analogous age obtained for the samples collected in the Daday Unit and in the Domuz Dağ Unit indicate that the nappe stack made of non-metamorphic and metamorphic units was exhumed at the same time.

To sum up, the pressure-temperature-time-deformation (P-T-t-d) path reconstructed for the Daday unit shows a classical clockwise trajectory with very different maximum pressure and temperature conditions (Fig. 13a). The Daday Unit was buried reaching the blueschist facies metamorphism conditions (D1 phase) and then exhumed during progressive top-to-the-S shearing from deep (D2 phase) to shallow crustal levels (<10-15km of depth; D3 phase). The last step of exhumation occurred at shallower structural levels under extensional tectonics induced by gravitational collapse. As the consequences, the D2, D3 and D4 phases were responsible of the metamorphic gaps existing between the Daday and Saka Units and the Ayli Dağ ophiolite unit and Arkot Dağ Mèlange and the large-scale crustal levels omission documented in the IPS zone nappe stack cropping out in the Daday Massif.

5.c. The post-collision evolution of the IPSZ

The architecture of the Daday Unit acquired during the exhumation path (see section above) was sealed by the upper Paleocene-middle Eocene deposits of the inter-mountain Karabük-Kastamonu basin (Tüysüz 1999; Hippolyte *et al.* 2010) and by middle Eocene volcaniclastics and lavas (Keskin *et al.* 2008). The metamorphic and non-metamorphic units of the IPS zone and the post-collisional deposits were lately deformed by the strike-slip or oblique high-angle fault systems related to the NAF zone. The F5 km-scale folds, well documented in the massif north of Araç, may be interpreted as structures associated to the transpressional tectonic regime of the NAF zone (Fig. 13a) and more in detail, they can be produced during the activity of the main fault system oriented ~WSW-ENE (Ellero *et al.* 2015a). The angle between the three systems of high-angle faults, the N-verging thrust and the F5 fold axes, in fact, is roughly compatible with the features expected from theoretical model in a zone of dextral shear (e.g. Wilcox *et al.* 1973) in which deformation is accommodated by both variably oriented compressional or extensional structures.

5.d. Constraints for the geodynamic evolution of Intra-Pontide Suture Zone

The structural, metamorphic and geochronological data collected in the Daday unit provide useful insights in the geodynamic history of IPS zone in Central Pontides. The structures and the metamorphism data collected from D1 phase relics, coupled with regional data, indicate that starting with the Middle Jurassic (Okay *et al.* 2013; Çimen *et al.* 2016a, b) an active subduction existed in the IPO basin (Fig. 13b). This subduction led to the underthrusting and accretion of the IPO crust covered by deep-sea sedimentary cover of Middle Jurassic age.

According to the reconstructed P-T path, the D2, D3 and D4 phases were achieved during the exhumation path from ~17-37 km of depth to shallow structural levels (<5 km of depth). These three phases may be developed from Albian (age of the D2 phase) to late Paleocene (i.e. immediately before the unconformable sedimentation of the deposits of the

Karabük-Kastamonu basins). The continuous trend of the P-T estimates equilibria points moving from pressure peak (D1 phase) to temperature peak (D2 phase) conditions (Fig. 9), indicate that the exhumation was associated to a continuous and progressive decrease of the pressure from ~1.30 GPa to ~0.55 GPa, and increase of the temperature up to ~480 °C. This exhumation path implies a change in the geothermal gradient from ~6-12 °C/km^{-1} to ~9-24 °C/km^{-1} during the D1 and the D2 phase, respectively. This change is consistent with a continent-arc collisional setting (e.g. Stern 2010). In this setting, the exhumation of rock bodies occurred close to the volcanic arc where an increase of the heat flow occurs (e.g. in the Taiwan convergent margin: Lin 2000; Chi & Reed 2008) (Fig. 13). This reconstruction is strongly supported by the identification of remnants of a continental (Ellero *et al.* 2015b) and intra-oceanic (Aygul *et al.* 2015a) arc-related volcanism of Late Cretaceous age in the IPS zone.

The polarity of the subduction was probably northward, according to the overall top-to-S sense of shear of the D2 and D3 phases and the location of the arc magmatism onto the IZ continental margin during Middle Jurassic (e.g. Gücer *et al.* 2016). In addition, the overall features of the D2, D3 and D4 phases show that the model for the exhumation of the Daday Unit can be acquired by extrusion in a subduction channel (e.g. Godin *et al.* 2006; Guillot *et al.* 2009 and references therein, Xypolias *et al.* 2012). In the subduction channel, the exhumation of rocks volume occurs through the activation of extensional detachments at the top and thrusts at the bottom of the channel during an overall compressional regime (Wheeler *et al.* 2001; Reddy *et al.* 2003; Jolivet *et al.* 2003). In this framework, the Daday Unit is exhumed initially as a weak, ductile body (D2 phase) and then as rigid but still deformable volume (D3 phase) in a time span running from Albian to late Paleocene (Fig. 13). Also the D4 phase can be interpreted in the same framework, when the over-thickening of the orogenic wedge during the increasing collision produced an extensional tectonics driven by low-angle normal faults and folds with sub-horizontal axial plane as detected in several orogenic belts

(e.g. Froitzheim 1992, Wheeler & Butler 1994; Marroni *et al.* 2004). The result of this process is the coupling of the Daday Unit with the non-metamorphosed Ayli Dağ ophiolite Unit and Arkot Dağ Mèlange at very shallow structural levels.

The pre-late Paleocene tectonic setting of the IPS zone has been strongly modified during Miocene time by the tectonics related to the NAF zone. Along the core zone of the NAF zone the units from the IPS zone are enclosed in lozenge-shape domains bounded by strike-slip faults (Ellero *et al.* 2015a), whereas far from the core zone, as in the Daday Massif, the pre-late Paleocene tectonic setting, even if strongly deformed by faults, thrusts and folds, can be still reconstructed.

6. Conclusions

The collected data indicate that the Daday Unit consists of a block-in-matrix assemblage derived from a supra-subduction-type oceanic crust and related deep-sea sedimentary cover of Middle Jurassic age. This setting has been acquired during the Late Jurassic by tectonic underplating at 35-42 km of depth leading to the development of blueschist facies metamorphism (D1 phase). The following D2, D3 and D4 phases developed during the exhumation the Daday Unit that occurred in a time span running from Albian to late Paleocene. The D2 phase developed under greenschist – lower pressure epidote blueschist facies, whereas the D3 and D4 phases are characterized by lower P-T conditions. The high geothermal gradient detected during the development of the D2 phase seems to be consistent with the inception of the exhumation during a continent-arc collision. On the whole, the transition from D2 to D3 and D4 phases indicate an exhumation of the Daday Unit from 37-17 km to uppermost structural levels (<5-10 km of depth). During the D2 and D3 phases, deformations with a dominant top-to-S sense of shear developed, whereas the D4 phase is characterized by structures indicating extensional tectonics.

This picture suggests that the IPO basin was characterized by a subduction zone where the Daday Unit experienced underthrusting and accretion since Late Jurassic and then exhumation, from the Early Cretaceous up to the Paleocene. The exhumation probably occurred in a subduction channel active during an arc-continent collision. The result of this process is the exhumation of the Daday Unit joined to its tectonic coupling with the pair Ayli Dağ ophiolite unit and Arkot Dağ Mèlange, i.e. the remnants of the shallower structural levels of the subduction system.

Acknowledgements

We thank Osman Parlak and an anonymous reviewer for the constructive criticisms that helped to improve the manuscript and Giovanni Capponi for the editorial work. The research has been funded by Darius Project (Resp. M. Marroni). This research benefits also by grants from PRIN 2008 and PRIN 2010–2011 Project (Resp. M. Marroni) and from IGG-CNR.

Supplementary material

To view supplementary material for this article, please visit http://journals. cambridge. org/geo

References

AKBAYRAM, K., OKAY, A. I. & SATIR, M. 2013. Early Cretaceous closure of the Intra-Pontide Ocean in western Pontides (northwestern Turkey). *Journal of Geodynamics* **65**, 38-55.

AYDIN, M., SAHINTÜRK, O., SERDAR, H. S., ÖZÇELIK, Y., AKARSU, I., ÜNGÖR, A., ÇOKUĞRAŞ, R. KASAR, S. 1986. The geology of the area between Ballidağ and Çangaldağ (Kastamonu) (in Turkish). *Bulletin of the Geological Society of Turkey* **29**, 1-16.

AYGÜL, M., OKAY, A. I., OBERHANSLI, R. & ZIEMANN, M. A. 2015a. Thermal structure of low-grade accreted Lower Cretaceous distal turbidites, the Central Pontides, Turkey: insights for tectonic thickening of an accretionary wedge. *Turkish J. Earth Sciences*, **24**, 461-474.

AYGÜL, M., OKAY, A. I., OBERHANSLI, R. SCHMIDT, A. & SUDO, M. 2015b. Late Cretaceous infant intra-oceanic arc volcanism, the Central Pontides, Turkey: Petrogenetic and tectonic implications. *Journal of Asian Earth Sciences*, **111**, 312-327.

BEDARD, J. H. 1999. Petrogenesis of Boninites from the Betts Cove Ophiolite, Newfoundland, Canada: Identification of Subducted Source Components. *Journal of Petrology* **40**, 1853–1889.

BERBER, F., GÖNCÜOĞLU, M. C. & SAYIT, K. 2014. Geochemistry and tectonic significance of the Kösedag metavolcanic rocks from the Sakarya Zone, Northern Turkey. *Bull. Shk. Gjeol.* Spec. Issue **2,** 161-163.

BERMAN, R. G. 1991. Thermobarometry using multiequilibrium calculations: a new technique with petrologic applications. *Canadian Mineralogist* **29**, 833–855.

CAMERON, W. E., CULLOCH, M. T. & WALKER, D. A. 1983. Boninite Petrogenesis: chemical and Nd-Sr isotopic constraints. *Earth and Planetary Science Letters* **65**, 75–89.

CATANZARITI, R., ELLERO, A., GÖNCÜOĞLU, M. C., MARRONI, M., OTTRIA, G. & PANDOLFI, L. 2013. The Taraklı Flysch in the Boyalı area (Sakarya Terrane, Northern Turkey): Implications for the tectonic history of the Intrapontide Suture Zone. C.R. Geosciences **345**, 454–461.

CHI, W. C. & REED, D. L. 2008. Evolution of shallow, crustal thermal structure from subduction to collision: An example from Taiwan. Geological Society of America Bulletin **120**, 679 – 690.

ÇIMEN, O., GÖNCÜOĞLU, M. C., SAYIT, K. & SIMONETTI, A. 2016a. Whole rock geochemistry, U-Pb geochronology and Lu-Hf isotope systematics of the Çangaldağ Pluton (Central Pontides, Turkey). 69th Geological Congress of Turkey. Abstracts and Programme, 148–149.

ÇIMEN, O., GÖNCÜOĞLU, M. C. & SAYIT, K. 2016b. Geochemistry of the meta-volcanic rocks from the Çangaldağ Complex in Central Pontides: Implications for the Middle Jurassic arc - back - arc system in the Neotethyan Intra - Pontide Ocean. *Turkish Journal of Earth Sciences* **25**, 491-512.

CRAWFORD, A. J., BECCALUVA, L. & SERRI, G. 1981. Tectono-magmatic evolution of the west Philipine-Mariana region and the origin of boninites. *Earth and Planetary Science Letters* **54**, 346–356.

COHEN, K. M., FINNEY, S. C., GIBBARD, P. L. & FAN, J.-X. (2013; updated 2016) The ICS International Chronostratigraphic Chart. *Episodes* **36**, 199-204.

DIZER, A. & MERIÇ, E. 1983. Late Cretaceous-Paleocene stratigraphy in northwest Anatolia. *Maden Tetkik ve Arama Enstitutusu Dergisi* **95/96**, 149–163.

ELLERO, A., OTTRIA, G., MARRONI, M., PANDOLFI, L. & GÖNCÜOGLU, M. C. 2015a. Analysis of the North Anatolian Shear Zone in Central Pontides (northern Turkey): Insight for geometries and kinematics of deformation structures in a transpressional zone. *Journal of Structural Geology* **72**, 124–141.

ELLERO, A., OTTRIA, G., SAYIT, K., CATANZARITI, C., FRASSI, C., GÖNCÜOGLU, M. C., MARRONI, M. & PANDOLFI, L. 2015b. Geological and geochemical evidence for a Late Cretaceous continental arc in the Central Pontides, northern Turkey. *Ofioliti* **40**, 73–90.

ELMAS, A. & YIĞITBAŞ, E. 2001. Ophiolite emplacement by strike-slip tectonics between the Pontide Zone and the Sakarya Zone in northwestern Anatolia, Turkey. *International Journal of Earth Sciences* **90**, 257–269.

FRASSI C., GÖNCÜOGLU M. C., MARRONI M., PANDOLFI L., RUFFINI L. ELLERO A., OTTRIA G. & SAYIT K. 2016. The Intra-Pontide Suture Zone in the Tosya-Kastamonu area, Northern Turkey (with geological map at 1:50. 000 scale). In press, Journal of Maps. DOI: 10.1080/17445647.2016.1192330.

FROITZHEIM, N. 1992. Formation of recumbent folds during synorogenic crustal extension (Austroalpine nappes, Switzerland). *Geology* **20**, 923–926.

FROST B. R. & FROST C. D. 2013. Essentials of Igneous and Metamorphic Petrology, Cambridge University Press, pp. 314.

GALLAGHER, K. 1995. Evolving temperature histories from apatite fission track data. *Earth and Planetary Science Letters* **136**, 421–435.

GODIN, L., GRUJIC, D., LAW, R. D. & SEARLE, M. P. 2006. Channel flow, ductile extrusion and exhumation in continental collision zones: An introduction. In *Channel Flow, Ductile Extrusion and Exhumation in Continental Collision Zones* (eds R. D. Law, M. P. Searle & L. Godin), pp. 1–23. Geological Society of London, Special Publications, no. 268.

GÖNCÜOĞLU M. C., ERENDIL M., TEKELI O., AKSAY A., KUS I. & ÜRGÜN B. M. 1987. Geology of the Armutlu Peninsula. In: Excursion Guidebook for the IGCP Project No. 5, 53 pp.

GÖNCÜOĞLU, M. C. & ERENDIL, M. 1990. Pre-Late Cretaceous tectonic units of the Armutlu Peninsula. *Proceeding of 8th Turkish Petroleum Congress* **8**, 161–168.

GÖNCÜOĞLU, M. C., DIRIK K. & KOZLU, H. 1997. Pre-Alpine and Alpine Terranes in Turkey: explanatory notes to the terrane map of Turkey. *Ann. Geol. Pays. Hellen.* **37**, 515-536.

GÖNCÜOĞLU, M. C., GÜRSU, S., TEKIN, U. K. & KOKSAL, S. 2008. New data on the evolution of the Neotethyan oceanic branches in Turkey: Late Jurassic ridge spreading in the Intra-Pontide branch. *Ofioliti* **33**, 153–164.

GÖNCÜOGLU, M. C., MARRONI, M., PANDOLFI, L., ELLERO, A., OTTRIA, G., CATANZARITI, R., TEKIN, U. K. & SAYIT, K. 2014. The Arkot Dağ Mélange in Araç area, central Turkey: Evidence of its

origin within the geodynamic evolution of the Intra-Pontide suture zone. *Journal of Asian Earth Sciences* **85**, 117–139.

GÖNCÜOGLU, M. C., MARRONI, M., SAYIT, K., TEKIN, U. K., OTTRIA, G., PANDOLFI, L. & ELLERO, A. 2012. The Aylı Dağ ophiolite sequence (central-northern Turkey): A fragment of Middle Jurassic oceanic lithosphere within the Intra-Pontide suture zone. *Ofioliti* **37**, 77–91.

GÖNCÜOĞLU, M. C., TURHAN, N., SENTURK, K., OZCAN, A. & UYSAL, S. 2000. A geotraverse across NW Turkey: tectonic units of the Central Sakarya region and their tectonic evolution. In *Tectonics and magmatism in Turkey and the surrounding area* (eds E. Bozkurt, J. Winchester & J. A. Piper), pp. 139-161. Geological Society of London Special Publication no. 173.

GÖRÜR, N., MONOD, O., OKAY, A. I., ŞENGÖR, A. M. C, TÜYSÜZ, O., YIĞITBAŞ, E., SAKINC, M. & AKKÖK, R. 1997. Palaeogeographic and tectonic position of the Carboniferous rocks of the western Pontides (Turkey) in the frame of the Variscan belt. *Bulletin de la Société Géologique de France* **168**, 197–205.

GÜCER, M. A., ARSLAN, M., SHERLOCK S. & HEAMAN, L. M. 2016. Permo-Carboniferous granitoids with Jurassic high temperature metamorphism in Central Pontides, Northern Turkey. *Mineralogy and Petrology*, on-line early view.

GUILLOT, S., HATTORI, K., AGARD, P., SCHWARTZ, S. & VIDAL O. 2009. Exhumation Processes in Oceanic and Continental Subduction Contexts: A Review. In *Subduction Zone Geodynamics* (eds S. Lallemand & F. Funiciello), pp. 175-205. Frontiers in Earth Sciences, Springer Berlin Heidelberg.

HICKEY-VARGAS, R., SAVOV, I., BIZIMIS, M., ISHII, T. & FUJIOKA, K. 2006. Origin of diverse geochemical signatures in igneous rocks from the West Philippine Basin: Implications for tectonic models, In Back-Arc Spreading Systems: Geological, Biological, Chemical and Physical Interactions (ed D. Christie), pp. 287–303. AGU Geophysical Monograph Series no. 166.

HIPPOLYTE, J.-C., MÜLLER, C., KAYMAKCI N. & E. SANGU 2010. Nannoplankton dating in the Black Sea inverted margin of central Pontides (Turkey) reveals two episodes of rifting. In *Sedimentary Basin Tectonics From the Black Sea and Caucasus to the Arabian Platform* (eds M. Sosson et al.), pp. 113–136. Geological Society of London, Special Volume, no. 340.

JOLIVET, L., FACCENNA, C., GOFFÉ, B., BUROV, E. & AGARD P. 2003. Subduction tectonics and exhumation of high-pressure metamorphic rocks in the Mediterranean orogens. *American Journal of Science* **303**, 353–409

KESKIN, M., GENÇ, Ş. C. & TÜYSÜZ O. 2008, Petrology and geochemistry of post-collisional Middle Eocene volcanic units in north-central Turkey: Evidence for magma generation by slab breakoff following the closure of the northern Neotethys Ocean, *Lithos* **104**, 267–305,

KETCHAM, R. A. 2005. Forward and inverse modeling of low-temperature thermochronometry data. *Rev. Mineral. Geochem*. **58**, 275–314.

KETCHAM, R. A., CARTER, A., DONELICK, R. A., BARBARAND, J. & HURFORD, A. J. 2007b. Improved modeling of fission-track annealing in apatite. Am. Mineral. **92**, 799–810.

KETCHAM, R. A., DONELICK, R. A. & DONELICK, M. B. 2000. AFTSolve: a program for multi-kinetic modeling of apatite fission-track data. *Geol. Mater. Res.* **2**, 1–32.

LEAKE, B. E., WOOLEY, A. R., ARPS, Z. E. S., ET AL. 1997. Nomenclature of amphiboles: Report of subcommittee on amphiboles of the International Mineralogical Association, commission on new minerals and mineral names. *Canadian Mineralogist* **35**, 219–246.

LEAT, P. T., LIVERMORE, R. A., MILLAR, I. L. & PEARCE, J. A. 2000. Magma supply in back-arc spreading centre segment E2, East Scotia Ridge. *Journal of Petrology* **41**: 845–866.

LIN, C. -H. 2000. Thermal modelling of continental subduction and exhumation constrained by heat flow and seismicity in Taiwan. *Tectonophysics* **324**, 189–201.

MARRONI, M., FRASSI, C., GÖNCÜOGLU, M. C., DI VINCENZO, G., PANDOLFI, L., REBAY, G., ELLERO, A. & OTTRIA, G. 2013. The Intra-Pontide Suture zone in Turkey: the eastern extension of the Dinaric-Hellenic belt? *Rendiconti on line SGI*, **29**, 93-96.

MARRONI, M., FRASSI, C., GÖNCÜOGLU, M. C., DI VINCENZO, G., PANDOLFI, L., REBAY, G., ELLERO, A. & OTTRIA, G. 2014. Late Jurassic amphibolite-facies metamorphism in the Intra-Pontide Suture Zone (Turkey): an eastward extension of the Vardar Ocean from the Balkans into Anatolia? *Journal of Geological Society* **171**, 605–609.

MARRONI, M., PANDOLFI, L. & MENEGHINI, F. 2004. From accretion to exhumation in a fossil accretionary wedge: a case history from Gottero Unit (Northern Apennines, Italy). *Geodinamica Acta* **17**, 41–53.

OKAY, A. I. & MONIÉ, P. 1997. Early Mesozoic subduction in the Eastern Mediterranean: Evidence from Triassic eclogite in northwest Turkey. *Geology* **25**, 595–598.

OKAY, A. I. & TÜYSÜZ, O. 1999. Tethyan sutures of northern Turkey. In *The Mediterranean basins, extension within the Alpine Orogen* (eds B. Durand, J. L. Olivet, E. Horvath & M. Serrane), pp. 475-515. *Turkish Journal of Earth Sciences* no. 156.

OKAY, A. I. & WHITNEY, D. L. 2010. Blueschists, eclogites, ophiolites and suture zones in northwest Turkey: A review and a field excursion guide. *Ofioliti* **35**, 131-172.

OKAY, A. I. 2000. Was the Late Triassic orogeny in Turkey caused by the collision of an oceanic plateau? In *Tectonic and magmatism in Turkey and surrounding area* (eds E. Bozkurt, J. A. Winchester & J. D. A. Piper), pp. 25–41. Geological Society Special Publications no. 173.

OKAY, A. I., MONOD, O. & MONIÉ, P. 2002. Triassic blueschists and eclogites from northwest Turkey: vestiges of the Paleo-Tethyan subduction. *Lithos* **64**, 155–178.

OKAY, A. I., SATIR, M. & SIEBEL, W. 2006. Pre-Alpide Palaeozoic and Mesozoic orogenic events in the Eastern Mediterranean region. In *European Lithosphere Dynamics* (eds D. G. Gee & R. A. Stepherson), pp. 389–406. Geological Society Special Publications no. 32.

OKAY, A. I., SATIR, M., MALUSKI, H., SIYAKO, M., MONIÉ, P. METZGER, R. & AKYÜZ, S. 1996. Palaeo- and Neo-Tethyan events in northwest Turkey. In *Tectonics of Asia (E.* Yin & M. Harrison M.), pp. 420–441. Cambridge University Press, Cambridge.

OKAY, A. I., SUNAL, G., SHERLOCK, S., ALTINER, D., TÜYSÜZ, O., KYLANDER-CLARK, A. R. C. & AYGÜL, M. 2013. Early Cretaceous sedimentation and orogeny on the active margin of Eurasia: Southern Central Pontides, Turkey. *Tectonics* **32**, 1247–1271.

ÖZCAN, E., LESS, G. & KERTESZ, B. 2007. Late Ypresian to middle Lutetian Orthophragminid record from central and northern Turkey: Taxonomy and remarks on zonal scheme. *Turkish Journal of Earth Sciences* **16**, 281–318.

PEARCE, J. A., STERN, R. J., BLOOMER S. H. & FRYER, P. 2005. Geochemical mapping of the Mariana arc-basin system: Implications for the nature and distribution of subduction components. *Geochemistry Geophysics Geosystems* **6**, Q07006, doi:10.1029/2004GC000895.

RAMSAY, J. G. 1967. Folding and Fracturing of Rocks. McGraw-Hill: New York; 568.

REDDY, S. M., WHEELER, J., BUTLER, R. W. H., CLIFF, R. A., FREEMAN, S., INGER, S. PICKLES, C. & KELLEY, S. P. 2003. Kinematic reworking and exhumation within the convergent Alpine Orogen. *Tectonophysics* **365**, 77-102.

ROBERTSON, A. H. F. & USTAÖMER, T. 2004. Tectonic evolution of the Intra-Pontide suture zone in the Armutlu Peninsula, NW Turkey. *Tectonophysics* **381**, 175–209.

ROBERTSON, A. H. F. & USTAÖMER, T. 2011. Role of tectonic-sedimentary mélange and Permian–Triassic cover units, central southern Turkey in Tethyan continental margin evolution. *Journal of Asian Earth Sciences* **40**, 98–120.

ROBERTSON, A. H. F., CLIFT, P. D., DEGNAN, P. J. & JONES, G. 1991. Palaeogeographical and palaeotectonic evolution of the eastern Mediterranean Neotethys. *Palaeogeogr. Palaeoclim. Palaeoecol.*, **87**, 289–343.

SAYIT, K., MARRONI, M., GÖNCÜOGLU, M. C., PANDOLFI, L., ELLERO, A., OTTRIA, G. & FRASSI, C. 2016. Geological setting and geochemical signatures of the mafic rocks from the Intra-Pontide suture zone: implications for the geodynamic reconstruction of the Mesozoic Neotethys. *International Journal of Earth Sciences* **105**, 39–64.

ŞENGÖR, A. M. C. & YILMAZ, Y. 1981. Tethyan evolution of Turkey: a plate tectonic approach. *Tectonophysics* **75**, 181–241.

STERN, R. J. 2010. The anatomy and ontogeny of modern intra-oceanic arc systems. In *The evolving continents: understanding processes of continental growth* (eds T. M. Kusky, M. G. Zhai & W. Xiao), pp. 7–34. Geological Society of London Special Publication no. 338.

STIPP, M., STÜNITZ, H., HEILBRONNER, R., SCHMID, S. M., 2002. The eastern Tonale fault zone: a 'natural laboratory' for crystal plastic deformation of quartz over a temperature range from 250 to 700 °C. *Journal of Structural Geology* **24**, 1861–1884.

SUN, S.-S. & MCDONOUGH, W. F. 1989. Chemical and isotopic systematics of oceanic basalts: implications for mantle composition and processes. In *Magmatism in the Ocean Basins* (eds A. D. Saunders & M. J. Norry), pp. 313–345. Geological Society of London, Special Publication no. 42.

TEKIN, U. K., GÖNCÜOGLU, M. C., PANDOLFI, L. & MARRONI, M. 2012. Middle-Late Trias radiolarian cherts from the Arkotdağ mélange in northern Turkey: implications for the life span of the northern Neotethyan branch. *Geodinamica Acta* **25**, 305–319.

TOKAY, M. 1973. Geological observations on them North Anatolian Fault Zone between Gerede and Ilgaz. Proceed. North Anatolian Fault and Earthquakes Symposium, Ankara. *The Mineral Research and Exploration Publication*, 12–29.

TRIBUZIO, R. & GIACOMINI, F. 2002. Blueschist facies metamorphism of peralkaline rhyolites from the Tenda crystalline massif (northern Corsica): evidence for involvement in the Alpine subduction event? *Journal of Metamorphic Geology* **20**, 513–526.

TÜYSÜZ, O. 1990. Tectonic evolution of a part of the Tethyside Orogenic Collage: the Kargı Massif, Northern Turkey. *Tectonics* **9**, 141–160.

USTAÖMER, P. A. & ROGERS G. 1999. The Bolu Massif: remnant of a pre-Early Ordovician active margin in the west Pontides, northern Turkey. *Geological Magazine* **136**, 579–592.

VIDAL, O. & PARRA, T. 2000. Exhumation paths of high-pressure metapelites obtained from local equilibria for chlorite-phengite assemblages. *Geological Journal* **35**, 139–161.

WHEELER J. & BUTLER R. W. H. 1994. Criteria for identifying structures related to true extension in orogens. *Journal of Structural Geology* **16**, 1023–1027.

WHEELER, J., REDDY, S. M. & CLIFF R. A. 2001. Kinematic linkage between internal zone extension and shortening in the more external units in the NW Alps. *Journal of the Geological Society of London* **158**, 439–443

WILCOX, R. E., HARDING, T. P. & SEELY D. R. 1973. Basic wrench tectonics. *AAPG Bulletin* **57**, 74–96.

XYPOLIAS, P., ILIOPOULOS, I., CHATZARAS, V. & KOKKALAS, S. 2012. Subduction - and exhumation - related structures in the Cycladic Blueschists: Insights from south Evia Island (Aegean region, Greece). *Tectonics* **31**, DOI: 10. 1029/2011TC002946.

YILMAZ, Y. 1990. Allochthonous terranes in the Tethyan Middle East, Anatolia and surrounding regions. *Philosophical Transaction Royal Society of London* A **331**, 611–624.

YILMAZ, Y., GENC, S. C., YIĞITBAŞ, E., BOZCU, M. & YILMAZ, K. 1995. Geological evolution of the late Mesozoic Continental margin of Nortwestern Anatolia. *Tectonophysics*, **243**, 155-171.

YILMAZ, Y., TÜYSÜZ, O., YIĞITBAŞ, E., GENÇ, S. C. & ŞENGÖR, A. M. C. 1997. Geology and tectonic evolution of the Pontides. In: Robinson, A. G. (Ed.), Regional and Petroleum geology of the Black Sea and surrounding region. *Bulletin American Association of Petroleum Geologists* **68**,183– 226.

Figure

Figure 1. (a) Tectonic map of the Anatolia peninsula. IZ: Istanbul-Zonguldak Terrane. SK: Sakarya Terrane. AT: Anatolide-Tauride Terrane. NAF: North Anatolian Fault. EAF: East Anatolian Fault. IPS: IntraPontide suture. Black line: ophiolite suture zones. (b) Schematic geological map of the Central Pontides.

Figure 2. Geological sketch map of the Intra-Pontide suture zone in the Daday massif (see Fig. 1b for map location). Stereographic projections of the main structural elements (S2: S2 foliation; A2: axes of F2 folds; S3: S3 foliation; A3: axes of F3 folds; S4: S4 foliation; A4: axes of F4 folds) are also showed (equal area, lower hemisphere). CPSC: Central Pontide Structural Complex (Tekin et al, 2012).

Figure 3. Geological cross-section of the Intra-Pontide suture zone along the Araç - Daday transect (see Fig. 2 for location).

Figure 4. Metamorphic rocks of the Daday Unit cropping out in the Araç area. (a) Micaschists. (b) Marble. (c) Quartzites. (d) Actinolite-bearing schist. S0: bedding; S2: S2 foliation.

Figure 5. Chemical classification of the metamorphic mafic rocks from the DDU exposed in the study area and the Tosya region (after Winchester & Floyd, 1977, modified by Pearce, 1996) (Alk-Bas: alkali basalt; And: andesite; Bas-And: basaltic andesite; TrachyAnd: trachy andesite). Note that two samples from the study area do not appear in the plot either due to very low Nb content or that Nb remained below the detection limit.

Figure 6. Trace element (left column) and REE (right column) patterns of the metabasic rocks form the DDU exposed in the study area and in the Tosya region. Normalization values from Sun & McDonough (1989).

Figure 7. Meso- and microstructures documented in the Daday Unit. (a) Thin section photomicrograph of micaschist (XPL). Phengite crystals (Phg) grew along the S1 foliation (S1). S2: S2 foliation. (b) Backscattering SEM image showing chlorite (Chl) and phengite (Phg) crystals grew along the S1 foliation (S1). S2: S2 foliation. (c) S1 foliation (S1) deformed by isoclinal F2 fold. S2: S2 foliation. (d) Thin section photomicrograph of actinolite (Act)-bearing schist (XPL). Chl: chlorite; Ep: epidote; Px: pyroxene; S2: S2 foliation. (e) Backscattering SEM image of actinolite (Act)-bearing schist. Chl: chlorite; Ep: epidote; Ab: albite; S2: S2 foliation. (f) Micaschists deformed by F3 folds. S2: S2 foliation; AP3: F3 axial plane. (g) Thin section photomicrograph of fine-grained micaschists (PPL). S2: S2 foliation; S3: S3 foliation; S4: S4 foliation. (h) Relationship between the four deformation phases documented in the field. S1: S1 foliation; S2: S2 foliation; AP3: F3 axial plane; AP4: F4 axial plane.

Figure 8. Compositional variability of chlorite (a) and phengite (b) used for thermodynamic calculations. (a) Si (apfu) *vs* $Mg/(Mg+Fe^{2+})$ diagram. (b) Al (apfu) versus Si (apfu) diagram.

Figure 9. Estimated metamorphic P–T conditions in the Daday Unit metasedimentary rocks. Calculated Chl-Phe-Qtz-H2O equilibrium P–T conditions using different Phe-Chl pairs (local equilibria method of Vidal & Parra 2000) from sample TC84. The average P–T estimates and the scatter of intersection (σT and σP) were calculated using INTERSX software (Berman 1991). Stability field of the metamorphic facies are from Frost & Frost

(2013). Abbreviations: Am: amphibolite facies; EAm: epidote-amphibolite facies; Ecl: eclogite facies; EBs: epidote blueschist facies; LBs: lawsonite blueschist facies; PGs: pumpellyite greenschist facies; Gs: greenschist facies; LAC: lawsonite-albite-chlorite; PP: prehnite-pumpellyite facies and Z: zeolite facies.

Figure 10. Results of ^{40}Ar–^{39}Ar laser step-heating experiments on white micas separates from sample 4-5-12 (a, b) and sample 8-7-11 (c). In (a) and (c) plateau steps are red, rejected steps are blue.

Figure 11. Profiles of apatite fission track (AFT) time-temperature (T-t) models of samples FT4 (collected in the SKU) and FT6 (collected in the DDU) performed with HeFTy program (Ketcham *et al.* 2007b). Brown envelopes stand for statistically good fit (statistical parameters >0.50), whereas green envelopes stand for acceptable fit (statistical parameters >0.05). The best fit thermal path for AFT is shown in black. On the right, mean track length distributions (light blu) and the best-fit curves (black) are shown.

Figure 12. Reconstruction of the hypothetical crustal section from which the metamorphic rocks of the Daday Unit derived and field pictures showing the pristine relationship between quarzites (i.e. meta-cherts), meta-volcaniclastics levels and actinolite-bearing schists (i.e. metabasalts) in the Tosya area.

Figure 13. (a) Retrograde pressure–temperature–time–deformation (P–T–t–D) path proposed for the metasedimentary rocks of the Daday Unit in the Araç area. (b)-(c) Geodynamic reconstruction of the Intra-Pontide Oceanic domain during the Late Jurassic (b) and Early Cretaceous (c). See text for further explanations.

Table 1. Correlation table showing the relationships between the Daday Unit and the different tectono-metamorphic units within the IPSZ. The correlation is based on both metamorphic/lithological features and location in the geological maps.

GEOLOGICAL MAP-BASED CORRELATION

IPSZ tectonic unit	Ustaömer & Robertson 1999	Okay *et al.* 2006	Okay *et al.* 2013
Daday Unit*	Domuzdağ-Saraycikdağ Complex *p.p.*	Late Cretaceous accretionary complex *p.p.*	Martin, Saka, Esenler and Domuzdağ Complexes *p.p.*
Saka Unit	-	Late Cretaceous accretionary complex *p.p.*	Saka Complex *p.p.*
Domuzdag Unit	Domuzdağ-Saraycikdağ Complex *p.p.*	Domuzdağ Complex *p.p.*	Domuzdağ Complex *p.p.*
Emirkoy Unit	-	Late Cretaceous accretionary complex *p.p.*	Martin and Esenler Complexes *p.p.*

LITHOLOGY-METAMORPHISM-BASED CORRELATION

IPSZ tectonic unit	Ustaömer & Robertson 1999	Okay *et al.* 2006	Okay *et al.* 2013
Daday Unit*	Domuzdağ-Saraycikdağ Complex *p.p.*	Domuzdağ Complex *p.p.*	Martin, Esenler and Domuzdağ Complexes *p.p.*
Saka Unit	-	-	Saka Complex
Domuzdag Unit	Domuzdağ-Saraycikdağ Complex *p.p.*	Domuzdağ Complex *p.p.*	Domuzdağ Complex
Emirkoy Unit	Domuzdağ-Saraycikdağ Complex *p.p.*	-	-

*Present study

Table 2. Electron microprobe analyses of representative phengite (Phe) and chlorite (Chl) used for thermodynamic calculations in sample TC84 (impure marble).

site	Syn-S1			syn-S2			Syn-S1			syn-S2		
mineral	Phe23	Phe38	Phe43	Phe2	Phe7	Phe51	Chl24	Chl28	Chl39	Chl6	Chl52	Chl61
Wt%												
SiO_2	50.62	49.17	49.44	50.60	50.13	48.57	26.26	26.02	25.75	26.20	24.73	24.93
TiO_2	0.17	0.34	0.22	0.23	0.19	0.28	0.10	0.10	0.01	0.06	0.04	0.10
Al_2O_3	28.65	30.27	28.07	29.07	28.91	29.78	21.91	22.48	22.21	21.52	22.97	23.27
FeO	2.87	2.99	3.30	2.65	3.06	3.16	25.47	23.57	23.64	24.01	23.47	23.57
MnO	0.00	0.03	0.05	0.03	0.03	0.01	0.16	0.21	0.16	0.18	0.14	0.17
MgO	2.63	2.30	2.68	2.79	2.60	2.57	13.63	15.58	14.89	16.14	15.58	15.57
CaO	0.01	0.01	0.00	0.02	0.03	0.00	0.09	0.02	0.03	0.02	0.02	0.04
Na_2O	0.22	0.31	0.31	0.30	0.28	0.38	0.04	0.00	0.04	0.01	0.00	0.04
K_2O	9.85	9.78	9.83	9.65	9.67	9.75	0.03	0.08	0.05	0.02	0.02	0.05
F	0.00	0.00	0.00	0.00	0.00	0.00	0.00	0.00	0.00	0.00	0.00	0.00
Cl	0.00	0.00	0.00	0.00	0.00	0.00	0.00	0.00	0.00	0.00	0.00	0.00
Sum	95.02	95.19	93.91	95.34	94.90	94.50	87.69	88.06	86.78	88.16	86.98	87.73
Cations												
Si	3.38	3.28	3.35	3.36	3.35	3.27	2.76	2.70	2.71	2.72	2.60	2.60
Al vi	0.62	0.72	0.65	0.64	0.65	0.73	1.24	1.30	1.29	1.28	1.40	1.40
Al iv	1.63	1.66	1.60	1.63	1.63	1.64	1.47	1.44	1.47	1.35	1.45	1.46
Ti	0.01	0.02	0.01	0.01	0.01	0.01	0.01	0.01	0.00	0.00	0.00	0.01
Fe	0.16	0.17	0.19	0.15	0.17	0.18	2.24	2.04	2.08	2.08	2.06	2.05
Mn	0.00	0.00	0.00	0.00	0.00	0.00	0.01	0.02	0.01	0.02	0.01	0.01
Mg	0.26	0.23	0.27	0.28	0.26	0.26	2.13	2.41	2.34	2.50	2.44	2.42
Ca	0.00	0.00	0.00	0.00	0.00	0.00	0.01	0.00	0.00	0.00	0.00	0.00
Na	0.03	0.04	0.04	0.04	0.04	0.05	0.01	0.00	0.01	0.00	0.00	0.01
K	0.84	0.83	0.85	0.82	0.82	0.84	0.00	0.01	0.01	0.00	0.00	0.01
Sum	6.92	6.95	6.96	6.92	6.93	6.97	9.88	9.93	9.92	9.96	9.97	9.97

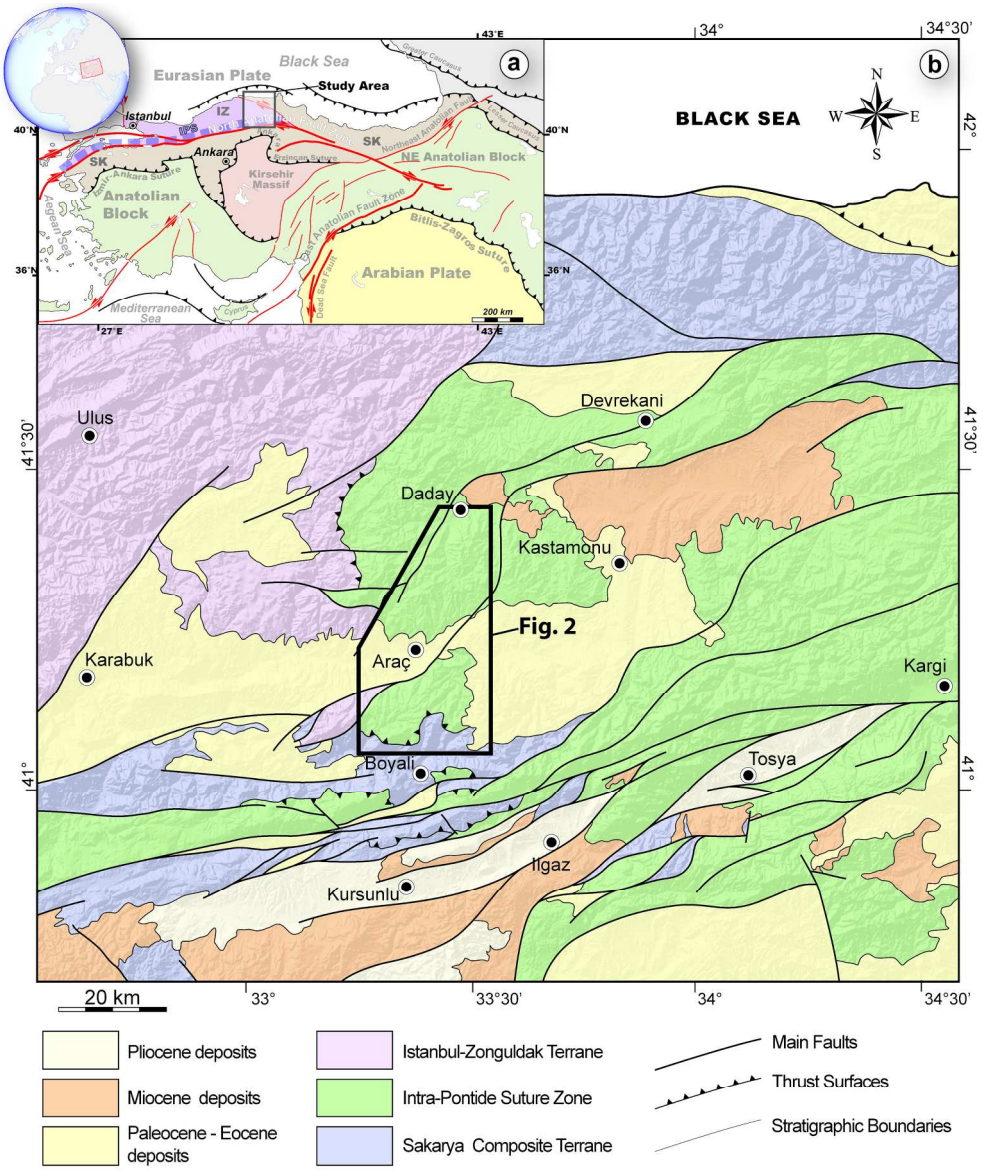

(a) Tectonic map of the Anatolia peninsula. IZ: Istanbul-Zonguldak Terrane. SK: Sakarya Terrane. AT: Anatolide-Tauride Terrane. NAF: North Anatolian Fault. EAF: East Anatolian Fault. IPS: Intra-Pontide suture. Black line: ophiolite suture zones. (b) Schematic geological map of the Central Pontides.
Fig. 1
203x240mm (300 x 300 DPI)

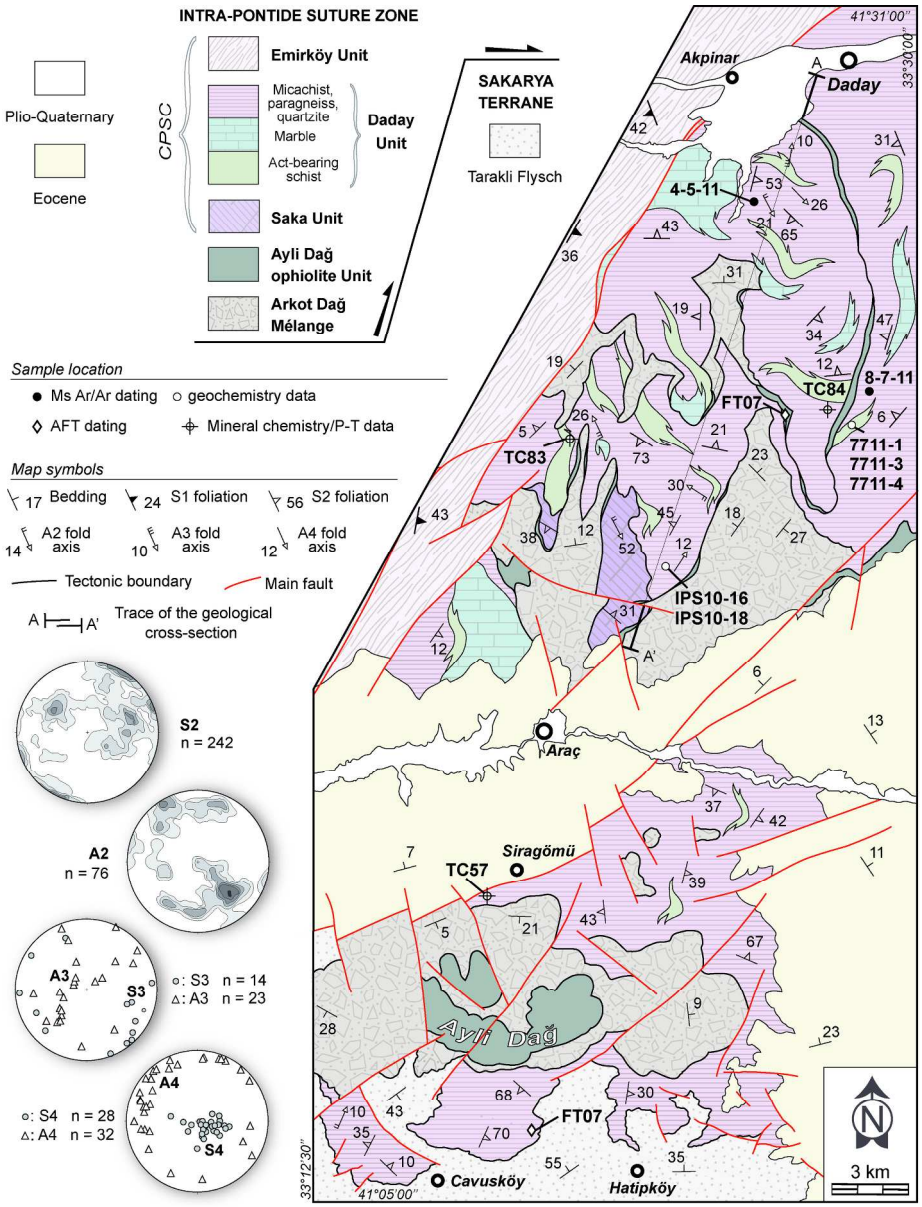

Geological sketch map of the Intra-Pontide suture zone in the Daday massif (see Fig. 1b for map location). CPSC: Central Pontide Structural Complex (Tekin et al, 2012).

Fig. 2

215x282mm (300 x 300 DPI)

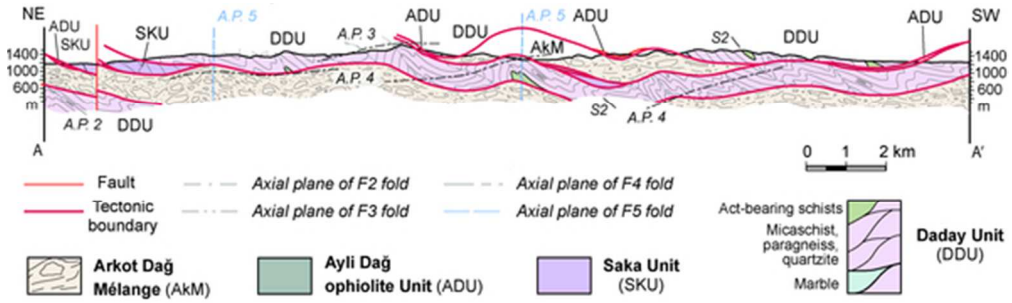

Geological cross-section of the Intra-Pontide suture zone along the Araç -Daday transect (see Fig. 2 for location).
Fig. 3
50x15mm (300 x 300 DPI)

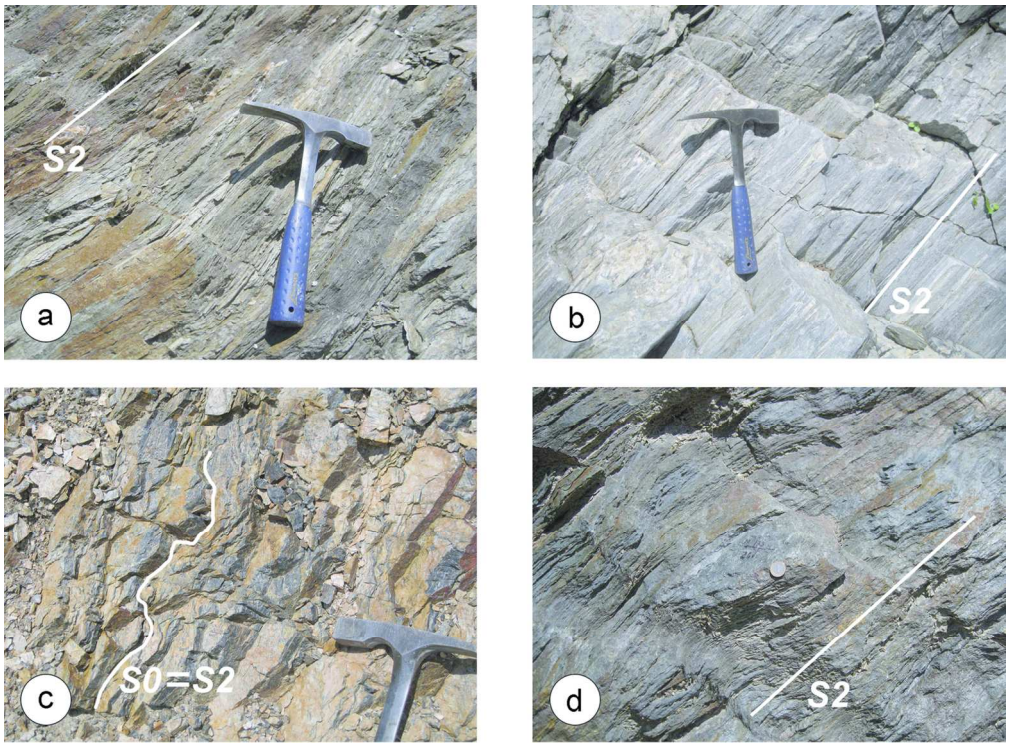

Metamorphic rocks of the Daday Unit cropping out in the Araç area. (a) Micaschists. (b) Marble. (c) Quartzites. (d) Actinolite-bearing schist. S0: bedding; S2: S2 foliation.
Fig. 4
132x97mm (300 x 300 DPI)

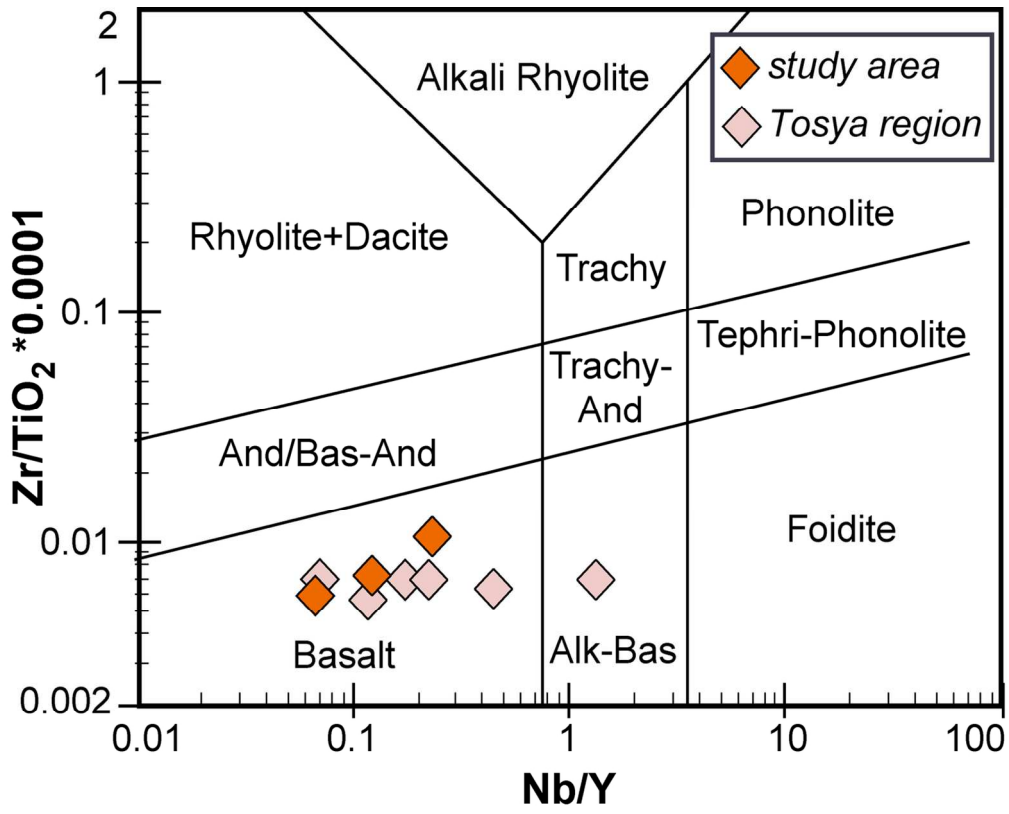

Chemical classification of the metamorphic mafic rocks belonging to the DDU (after Winchester & Floyd, 1977, modified by Pearce, 1996) (Alk-Bas: alkali basalt; And: andesite; Bas-And: basaltic andesite; TrachyAnd: trachy andesite).
Fig. 5
64x51mm (600 x 600 DPI)

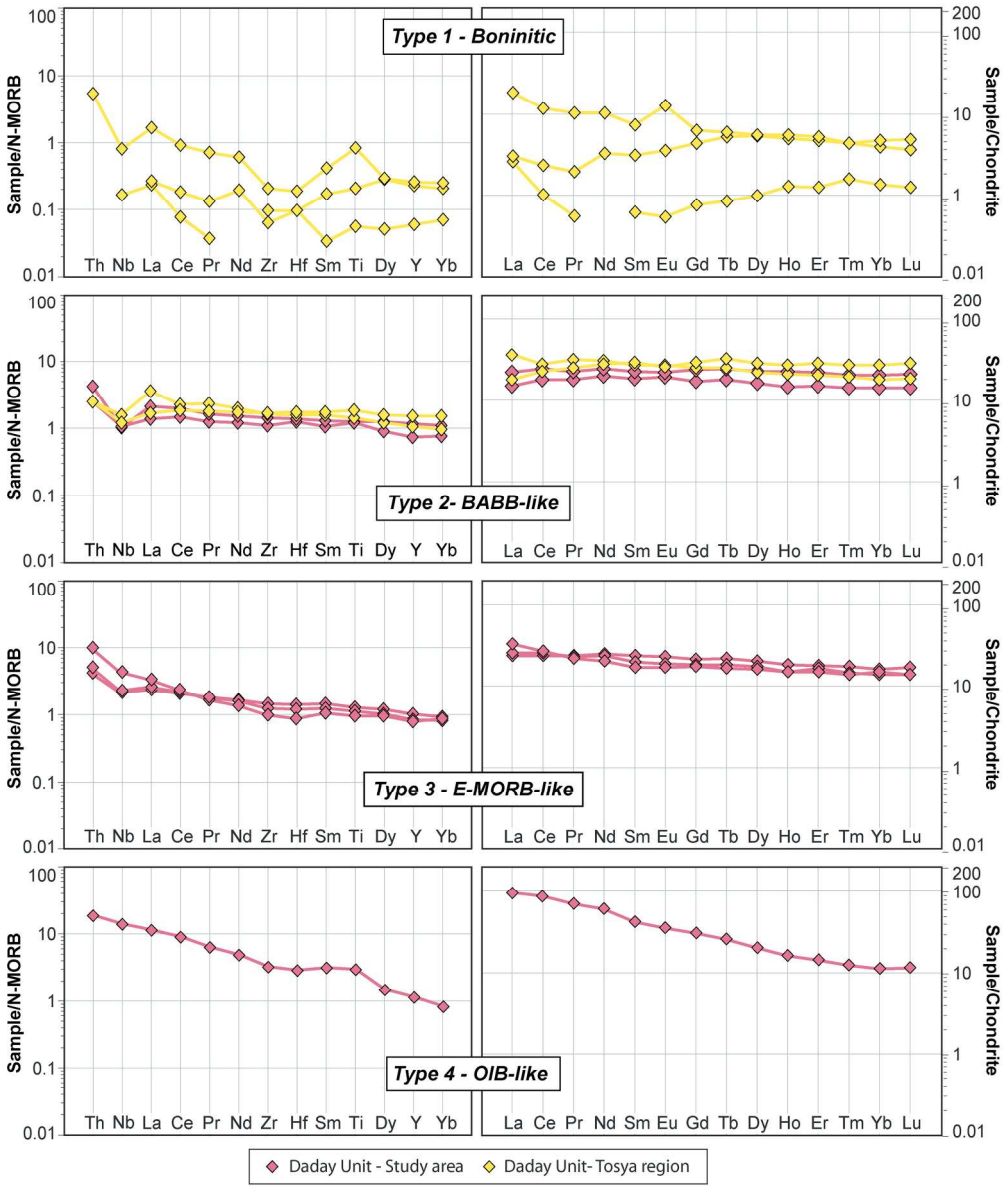

Trace element (left column) and REE (right column) patterns of the metabasic rocks form the DDU exposed in the study area and in the Tosya region. Normalization values from Sun & McDonough (1989).

FIg. 6

188x223mm (300 x 300 DPI)

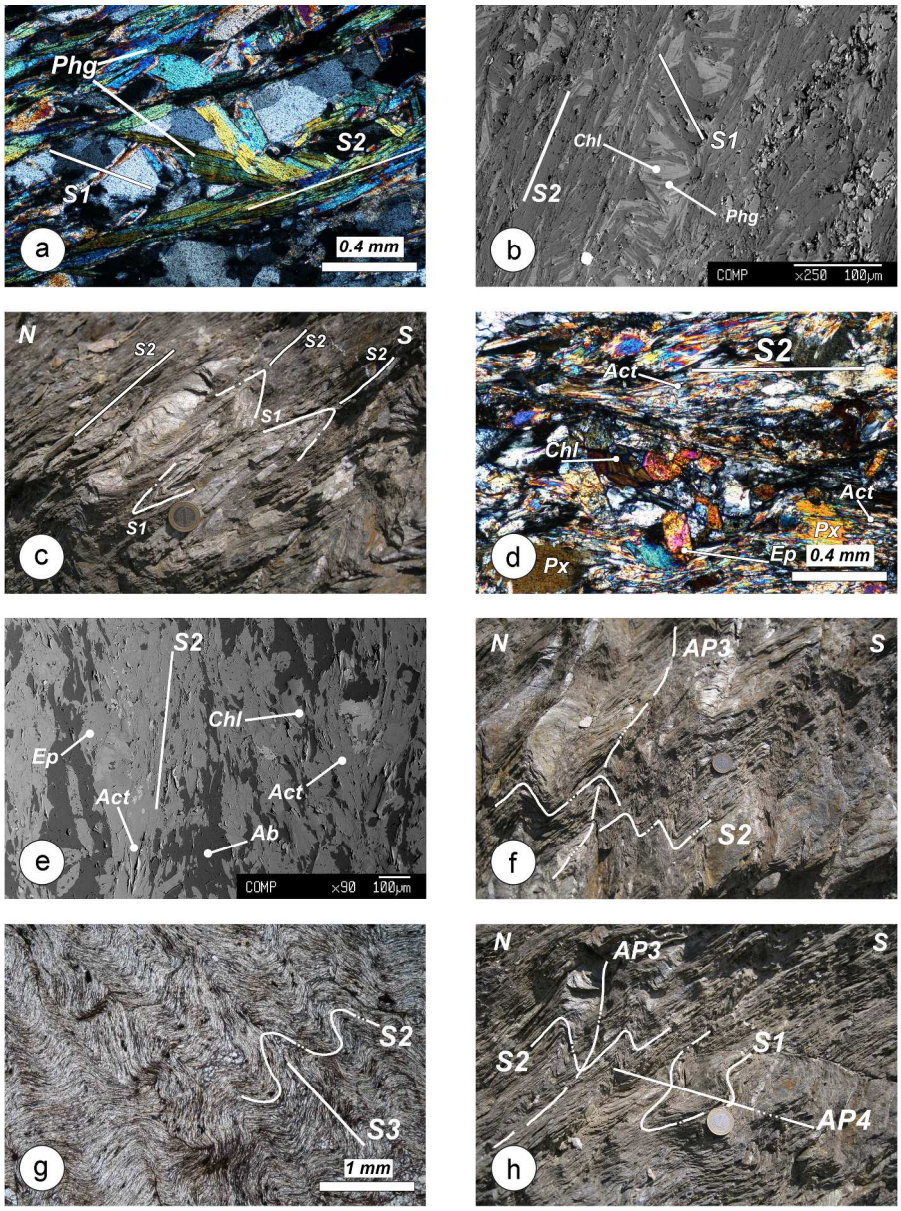

Meso- and microstructures documented in the Daday Unit. (a) Thin section photomicrograph of micaschist (XPL). Phengite crystals (Phg) grew along the S1 foliation (S1). S2: S2 foliation. (b) Backscattering SEM image showing chlorite (Chl) and phengite (Phg) crystals grew along the S1 foliation (S1). S2: S2 foliation. (c) S1 foliation (S1) deformed by isoclinal F2 fold. S2: S2 foliation. (d) Thin section photomicrograph of actinolite (Act)-bearing schist (XPL). Chl: chlorite; Ep: epidote; Px: pyroxene; S2: S2 foliation. (e) Backscattering SEM image of actinolite (Act)-bearing schist. Chl: chlorite; Ep: epidote; Ab: albite; S2: S2 foliation. (f) Micaschists deformed by F3 folds. S2: S2 foliation; AP3: F3 axial plane. (g) Thin section photomicrograph of fine-grained micaschists (PPL). S2: S2 foliation; S3: S3 foliation; S4: S4 foliation. (h) Relationship between the four deformation phases documented in the field. S1: S1 foliation; S2: S2 foliation; AP3: F3 axial plane; AP4: F4 axial plane.

Fig. 7

241x324mm (300 x 300 DPI)

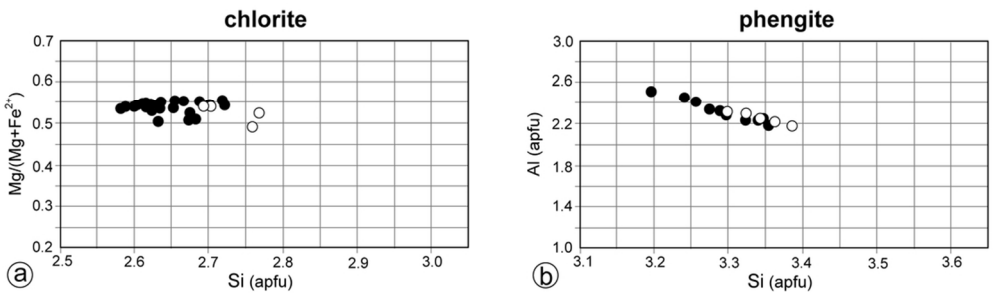

Compositional variability of chlorite (a) and phengite (b) used for thermodynamic calculations. (a) Si (apfu) vs Mg/(Mg+Fe2+) diagram. (b) Al (apfu) versus Si (apfu) diagram.
FIg. 8
48x14mm (600 x 600 DPI)

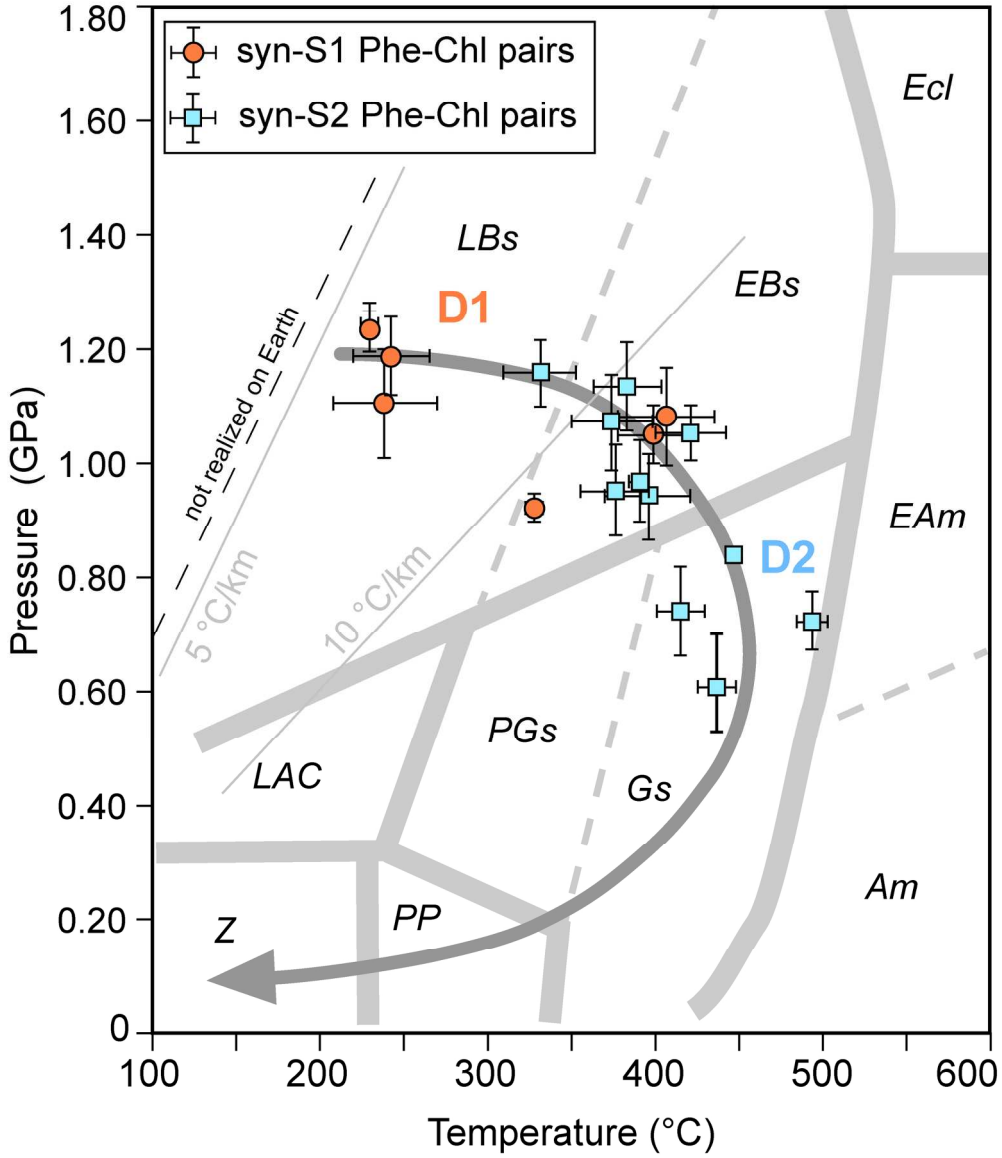

Estimated metamorphic P–T conditions in the Daday Unit metasedimentary rocks. Calculated Chl-Phe-Qtz-H2O equilibrium P–T conditions using different Phe-Chl pairs (local equilibria method of Vidal & Parra 2000) from sample TC84. The average P–T estimates and the scatter of intersection (σT and σP) were calculated using INTERSX software (Berman 1991). Stability field of the metamorphic facies are from Frost & Frost (2013). Abbreviations: Am: amphibolite facies; EAm: epidote-amphibolite facies; Ecl: eclogite facies; EBs: epidote blueschist facies; LBs: lawsonite blueschist facies; PGs: pumpellyite greenschist facies; Gs: greenschist facies; LAC: lawsonite-albite-chlorite; PP: prehnite-pumpellyite facies and Z: zeolite facies.
Fig. 9
91x106mm (600 x 600 DPI)

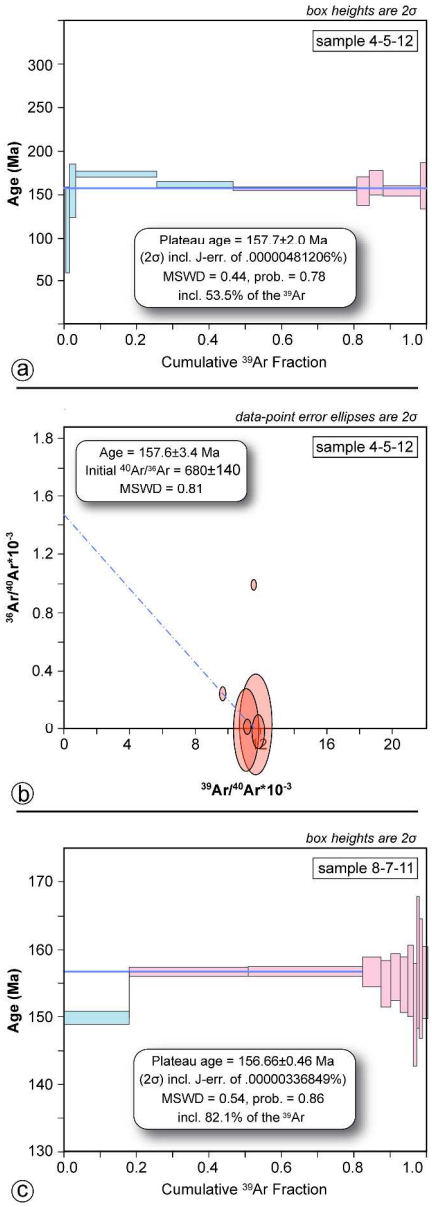

Results of 40Ar–39Ar laser step-heating experiments on white micas separates from sample 4-5-12 (a, b) and sample 8-7-11 (c). In (a) and (c) plateau steps are red, rejected steps are blue.

FIg. 10

224x631mm (600 x 600 DPI)

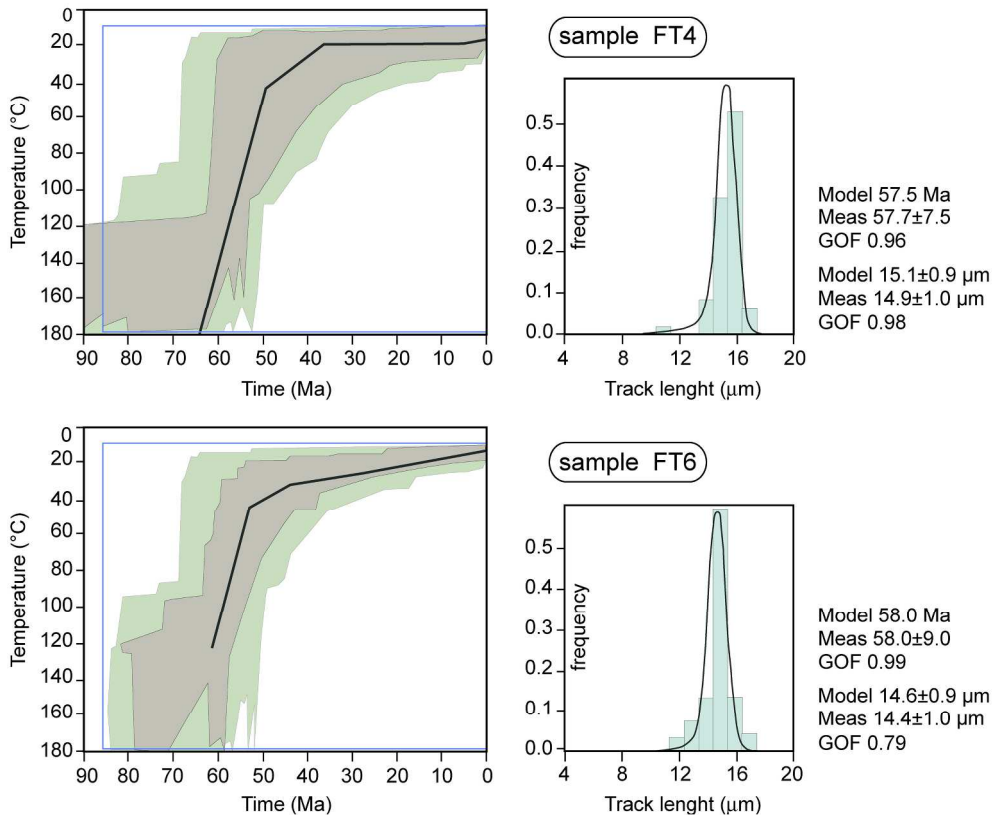

Profiles of apatite fission track (AFT) time-temperature (T-t) models of samples FT4 (collected in the SKU) and FT6 (collected in the DDU) performed with HeFTy program (Ketcham et al. 2007b). Brown envelopes stand for statistically good fit (statistical parameters >0.50), whereas green envelopes stand for acceptable fit (statistical parameters >0.05). The best fit thermal path for AFT is shown in black. On the right, mean track length distributions (light blu) and the best-fit curves (black) are shown.

Fig. 11

114x92mm (600 x 600 DPI)

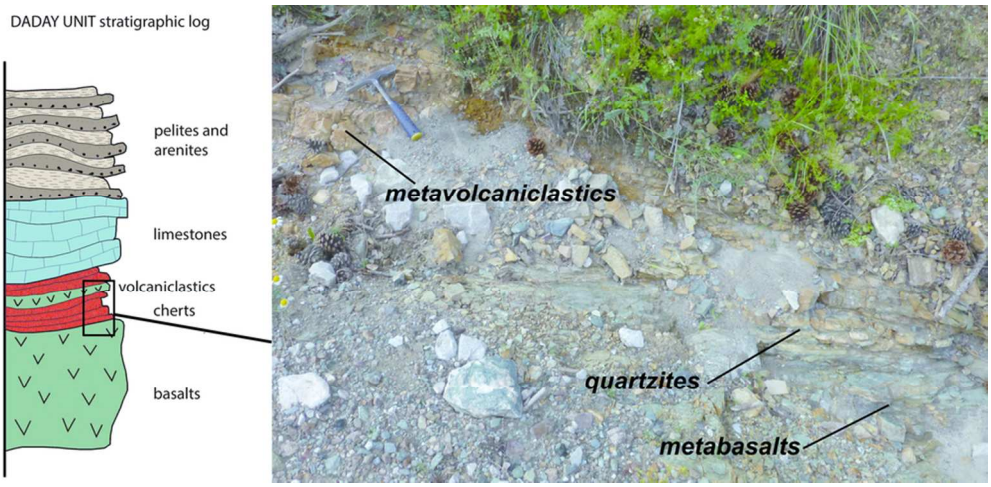

Reconstruction of the hypothetical crustal section from which the metamorphic rocks of the Daday Unit derived and field pictures showing the pristine relationship between quarzites (i.e. meta-cherts), meta-volcaniclastics levels and actinolite-bearing schists (i.e. metabasalts) in the Tosya area.
Fig. 12
85x40mm (300 x 300 DPI)

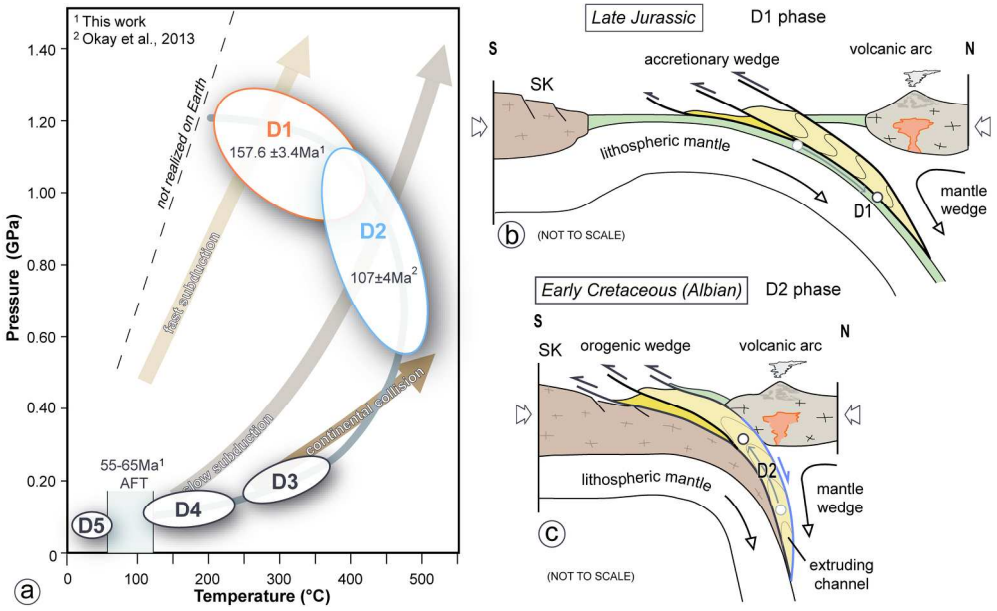

(a) Retrograde pressure–temperature–time–deformation (P–T–t–D) path proposed for the metasedimentary rocks of the Daday Unit in the Araç area. (b)-(c) Geodynamic reconstruction of the Intra-Pontide Oceanic domain during the Late Jurassic (b) and Early Cretaceous (c). See text for further explanations.
FIg. 13
100x60mm (600 x 600 DPI)

Geological Magazine

Supplementary Material

Burial and exhumation history of the Daday Unit (Central Pontides, Turkey): implications for the closure of the Intra-Pontide oceanic basin.

Frassi C., Marroni M., Pandolfi L., Göncüoğlu M. C., Ellero A., Ottria G., Sayit K., McDonald C. S., Balestrieri M. L., Malasoma A.

1. Mineral chemistry and thermobaric estimations

Running conditions during microprobe chemical analyses were 15 kV accelerating voltage and 5 nA beam current on a Faraday cage. Counting time for the determined elements ranged from 10 to 60 s at both peak and background. Nominal beam spot size ranges from 1 to 3 μm for the analyses of all minerals. Natural and synthetic silicates and oxides were used for instrumental calibration.

The thermodynamic calculations are performed with TWEEQ software (Berman 1991). The thermodynamic data and the solid-solution models are from Berman (1988; 1990) for all phases except K-white mica and chlorite. The former were studied with the Parra *et al.* (2000, 2002a) models, while the latter with Parra *et al.* (2000) and Vidal *et al.* (2001, 2005). The end-members to use for the thermodynamic calculations, should describe the white mica and chlorite chemical composition. For the white mica, the following end-members were used: Mg-Al-celadonite (Mg-ACel)$_{Phe}$, pyrophyllite (Prl)$_{Phe}$ and muscovite (Ms)$_{Phe}$, whereas for the analyzed chlorites, characterized by high Si contents, we used 4 end-members: Mg-sudoite (Sud)$_{Chl}$, clinochlore (Clin)$_{Chl}$, Fe-amesite (Fe-Ames) $_{Chl}$ and daphnite (Daph)$_{Chl}$. The presence of Fe^{3+} will affect the activity of chlorite end-members, although it is generally neglected because no difference can be made between Fe^{2+} and Fe^{3+} with the microprobe. An estimation of Fe^{3+} in chlorite can be done using the criterion proposed by Vidal *et al.* (2006).

The number of reactions that can be computed for a given paragenesis involving chlorite and phengite, depends on the number of end-members used to express the compositional variability of these minerals. The K_2O-Al_2O_3–FeO–MgO-SiO_2-H_2O system, the P-T conditions for the chlorite-phengite-quartz-H_2O assemblage are given by the

intersection of 13 equilibria, among which 3 are independent. Some scatter of the intersection points in the diagrams was observed. According to Vidal & Parra (2000), this scatter results from cumulated errors in each reaction, which stem from the uncertainties in the thermodynamic standard-state properties of the end-members and the solution models, departure of the analysed compositions from equilibrium compositions and analytical uncertainties. The first source of error, resulting from the uncertainties associated with the thermodynamic data, is difficult to estimate because the thermodynamic standard-state properties were calibrated using experimental and natural data of various levels of confidence. However, it is likely that the uncertainties in the thermodynamic data have a systematic effect on the calculated locations of the intersection points, but not on their relative positions. Finally, even if the thermodynamic data were "perfect", imprecision on the analysed compositions places limits on the precision with which P-T can be estimated (De Andrade *et al.* 2006).

The average P-T estimates and their associated deviations (σP and σT) were calculated for each mineral pair by the INTERSX software included in the TWEEQ package (Berman 1991). According to Berman (1991), Vidal & Parra (2000), Trotet *et al.* (2001) and Parra *et al.* (2002b), the magnitude of the pressure (σP) and temperature (σT) scatter for the calculated equilibria lead to reject the chlorite–phengite pairs, which are considered to be out of equilibrium. Assuming that the thermodynamic data are "perfect" and equilibrium is achieved, the scatter resulting from analytical uncertainties is given by the precision of the microprobe analysis. It can be calculated with a Monte Carlo technique (Lieberman & Petrakakis 1991; Vidal & Parra 2000), which lead to the estimation of the maximum permissible scatter (σP_{max} and σT_{max}) of any P-T estimate. The estimated σP_{max} and σT_{max} values for assemblages including chlorite and phengite are 0.08 GPa and 25 °C, respectively (Vidal & Parra 2000; Trotet *et al.* 2001; Parra *et al.* 2002b; Augier *et al.* 2005; Rimmelé *et al.* 2005*).*

References

AUGIER, R., AGARD, P., MONIE, P., JOLIVET, L., ROBIN, C. & BOOTH-REA, G. 2005. Exhumation, doming and slab retreat in the Betic Cordillera (SE Spain): in situ 40Ar/39Ar ages and P–T-d-t paths for the Nevado-Filabride complex. *Journal of Metamorphic Geology* **23**, 357–381.

BERMAN, R. G. 1988. Internally-consistent thermodynamic data for stoichiometric minerals in the system Na2O-K2O-CaO-MgO-FeO-Fe2O3-Al2O3-SiO2-TiO2-H2O-CO2. *Journal of Petrology* **29**, 445–522.

BERMAN, R. G. 1990. Mixing properties of Ca-Mg-Fe-Mn garnets. *American Mineralogist* **75**, 328–344.

BERMAN, R. G. 1991. Thermobarometry using multiequilibrium calculations: a new technique with petrologic applications. *Canadian Mineralogist* **29**, 833–855.

DE ANDRADE, V., VIDAL, O., LEWIN, E., O'BRIEN, P. & AGARD P. 2006. Quantification of electron microprobe compositional maps of rock thin sections: an optimized method and examples. *Journal of Metamorphic Geology* **24**, 655–668.

LIEBERMAN, J. & PETRAKAKIS, K. 1991. TWEEQU thermobarometry: analysis of uncertainties and application to granulites from the western Alaska and Austria. *Canadian Mineralogist* **29**: 857–887.

Parra *et al.* (2000)

PARRA, T., VIDAL, O. & AGARD, P. 2002a. A thermodynamic model for Fe-Mg dioctahedral K white micas using data from phase-equilibrium experiments and natural pelitic assemblages. *Contribution to Mineralogy and Petrology* **143**, 706–732.

PARRA, T., VIDAL, O. & JOLIVET, L. 2002b. Relation between the intensity of deformation and retrogression in blueschist metapelites of Tinos Island (Greece) evidenced by chlorite-mica local equilibria. *Lithos* **63**, 41–66.

RIMMELE´, G., PARRA, T., GOFFE´, B., OBERHANSLI, R., JOLIVET, L. & CANDAN, O. 2005. Exhumation paths of high pressure-low temperature rocks from the Lycian Nappes and the Menderes Massif (SW Turkey): a multi-equilibrium approach. *Journal of Petrology* **46**, 641–669.

TROTET, F., VIDAL, O. & JOLIVET, L. 2001a. Exhumation of Syros and Sifnos metamorphic rocks (Cyclades, Greece). New constraints on the P–T paths. *European Journal of Mineralogy* **13**, 901–920.

VIDAL, O. & PARRA, T. 2000. Exhumation paths of high-pressure metapelites obtained from local equilibria for chlorite-phengite assemblages. *Geological Journal* **35**, 139–161.

VIDAL, O., DE ANDRADE, V., LEWIN, E., MUNOZ, M., PARRA, T. & PASCARELLI, S. 2006. P–T-deformation-Fe3þ/Fe2þ mapping at the thin section scale and comparison with XANES mapping: application to a garnet-bearing metapelite from the Sanbagawa metamorphic belt (Japan). *Journal of Metamorphic Geology* **24**, 669–683.

VIDAL, O., PARRA, T. & TROTET, F. 2001. A thermodynamic model for Fe-Mg aluminous chlorite using data from phase equilibrium experiments and natural pelitic assemblages in the 100–6008C, 1–25 kbar P–T range. *American Journal of Science* **301**, 557–592.

VIDAL, O., PARRA, T. & VIEILLARD, P. 2005. Experimental data on the Tschermak solid solution in Fe-chlorites: application to natural examples and possible role of oxidation. *American Mineralogist* **90**, 359–370.

2. $^{39}Ar/^{40}Ar$ geochronology

Muscovite separates used for $^{40}Ar/^{39}Ar$ analysis were prepared by crushing rocks, sieving to the grain size of 60-180 μm and separated using heavy liquids separation and dry shaking at the Middle East Technical University in Ankara (Turkey). The 40Ar/39Ar analyses have been conducted at Group 18 Laboratories in the Arizona State University.

Multiple crystals of muscovite were packed in Al foil, loaded into Al discs, and stacked in a flame-sealed glass vial for irradiation. Standards of HD-B1 with an age of 24.18 ± 0.009 Ma (Schwarz & Trieloff 2007) were placed within wells adjacent to the samples and throughout the entire stack to permit detailed characterization of the irradiation flux both horizontally and vertically. Samples were irradiated in the Cd-lined (CLICIT) facility of the Oregon State University (USA) TRIGA reactor for 4 hours.

Samples were fused with a Photon Machines 55W CO_2 laser. Isotope data were collected using a Nu Insturments Nobelesse multi-collector mass spectrometer, run in single collector mode. Samples were heated for 10 seconds prior to 120 seconds clean-up. Extracted gases were cleaned using 2 GP50 SAES getters (one operated at 450°C and one at room temperature). The extraction, clean up and data collection processes were entirely automated. Average backgrounds ± standard deviations from all five blank runs were used to correct isotope abundances. Air calibrations were collected after every 10 analyses to monitor mass discrimination. A $^{40}Ar/^{36}Ar$ value of 295.5 was used to correct the data for mass discrimination. A power law function was used for the mass discrimination correction (Renne *et al.* 2009).

Berkeley Geochronology Centre software 'mass spec' was used to regress and reduce age data using the decay constant of 5.543×10^{-10} a^{-1} from Steiger & Jager (1977). The isotope data were corrected for blank, radioactive decay, mass discrimination and interfering reactions. Age uncertainties are reported to 2σ; uncertainties on the isotopic measurements are reported to 1σ.

References

RENNE, P. R., CASSATA, W. S. & MORGAN, L. E. 2009. The isotopic composition of atmospheric argon and $^{40}Ar/^{39}Ar$ geochronology: Time for a change? *Quaternary Geochronology*, **4**, 288–298.

SCHWARZ, W. H. & TRIELOFF, M. 2007. Intercalibration of $^{40}Ar/^{39}Ar$ age standards NL-25, HB3gr hornblende, GA1550, SB-3, HD-B1 biotite and BMus/2 muscovite. *Chemical Geology*, **242**, 218-232.

STEIGER, R. H. & JAGER, E. 1977. Subcommission on geochronology: Convention on the use of decay constants in geo- and cosmochemistry. *Earth and Planetary Science Letters*, **36**, 359-362.

3. Fission track

Apatite grains were separated from about 5 kg bulk samples using standard heavy liquids and magnetic separation techniques. Mounts were ground, polished and etched with 5 N HNO3 at 20 ± 1 °C for 20.0±1s to reveal the spontaneous tracks. Samples were then irradiated with thermal neutrons in the Lazy Susan facility of the Triga Mark II reactor at the University of Pavia (Italy). To measure the neutron fluency, standard glass CN5 was used as dosimeters. After irradiation, the low-U muscovite detectors were etched in 40% HF at 20 °C for 45min to reveal the induced fission-tracks. Apatite fission-track ages were measured and calculated using the external-detector and the zeta-calibration methods (Hurford & Green 1983) with a zeta value (referred to Fish Canyon Tuff and Durango apatite standards, Hurford 1990) of ζ=360±11. The annealing behaviour of fission tracks in apatite is sensitive to chemical composition. Chlorine rich apatites are more resistant to track annealing than fluorine-rich apatites (O'Sullivan & Parrish 1995). In order to quantify chlorine and fluorine content of apatite crystals Dpar values (diameter of etched spontaneous fission tracks measured parallel to the crystallographic c-axis) were measured in all the samples (e.g. Barbarand *et al.* 2003; O'Sullivan & Parrish, 1995). We routinely measured 4 etch pits in each grain. A small Dpar value (smaller than 2 μm) is typical for fluorine-rich apatites and a larger value (2–5 μm) is characteristic for chlorine rich apatites. Only TINTs (tracks reached by the etching because they intercept a surface track, Bhandari *et al.* 1971) made part of the measured length distributions as recommended by Ketcham *et al.* (2005). We performed a thermal modelling using the HeFTy software (Ketcham 2005). In HeFty, fission-track lengths normalized

for track angle using c-axis projection (Ketcham *et al.* 2007a, 2009) and the annealing model of Ketcham *et al.* (2007b) was used.

References

BARBARAND, J., CARTER, A., WOOD, I. & HURFORD, T. 2003. Compositional and structural control of fission-track annealing in apatite. *Chemical Geology* **198**, 107–137.

BHANDARI, N., BHAT, S. G., LAL, D., RAJAGOPALAN, G., TAMHANE, A. S. & VENKATAVARADAN, V. S. 1971. Fission fragment tracks in apatite: recordable track lengths. *Earth Planetary Sciences Letters* **13**, 191–199.

DUNKL, I. 2002. Trackkey: a Windows program for calculation and graphical presentation of fission track data. *Comput. Geosci.* **28**, 3–12.

GALBRAITH, R.F. 1981. On statistical models of fission track counts. *J. Int. Assoc. Math. Geol.* **13**, 471–478.

GALLAGHER, K. 1995. Evolving temperature histories from apatite fission-track data. *Earth Planetary Sciences Letters* **136**, 421–435.

GREEN, P. F. & DUDDY, I. R. 1989. Some comments on paleotemperature estimation from apatite fission track analysis. *J. Pet. Geol.* **12**, 111–114.

GREEN, P. F., DUDDY, I. R. & HEGARTY, K. A. 2002. Quantifying exhumation from apatite fission track analysis and vitrinite reflectance data: precision, accuracy and latest results from the Atlantic margin of NW Europe. Exhumation of the North Atlantic Margin: Timing, Mechanisms and Implications for Petroleum Exploration. In: Doré, A.G., Green, P.F., Moore, M.E., O'Brien, C., Crowhurst, P.V., 2003. Thermal History Reconstruction In The Ataa-1, Gane-1, Gant-1, Gro-3 And Umiivik-1 Boreholes, Onshore West Greenland, Based On Afta®, Vitrinite Reflectance And Apatite (U–Th)/He Dating. Geotrack Report 883.

HURFORD, A. J. 1990. Standardization of fission track dating calibration: recommendation by the Fission TrackWorking Group of the I.U.G.S. Subcommission on Geochronology. *Chemical Geology* **80**, 171–178.

HURFORD, A. J. & GREEN, P. F. 1983. The zeta age calibration of fission-track dating. *Chemical Geology* **41**, 285–317.

KETCHAM, R. A. 2005. Forward and inverse modeling of low-temperature thermochronometry data. *Rev. Mineral. Geochem.* **58**, 275–314.

KETCHAM, R. A., DONELICK, R. A. & DONELICK, M. B. 2000. AFTSolve: a program for multi-kinetic modeling of apatite fission-track data. *Geol.Mater. Res.* **2**, 1–32.

KETCHAM, R. A., CARTER, A., DONELICK, R. A., BARBARAND, J. & HURFORD, A. J. 2007a. Improved measurement of fission-track annealing in apatite using c-axis projection. *American Mineralogist* **92**, 789–798.

KETCHAM, R. A., CARTER, A., DONELICK, R. A., BARBARAND, J. & HURFORD, A.J. 2007b. Improved modeling of fission-track annealing in apatite. *American Mineralogist* **92**, 799–810.

KETCHAM, R. A., DONELICK, R. A., BALESTRIERI, M. L. & ZATTIN, M. 2009. Reproducibility of apatite fission-track length data and thermal history reconstruction. *Earth Planetary Sciences Letters* **284**, 504–515.

Geological Magazine

Supplementary Material

Burial and exhumation history of the Daday Unit (Central Pontides, Turkey): implications for the closure of the Intra-Pontide oceanic basin.

Frassi C., Marroni M., Pandolfi L., Göncüoğlu M. C., Ellero A., Ottria G., Sayit K., McDonald C. S., Balestrieri M. L., Malasoma A.

Supplementary Material S2: GPS coordinates for samples used in the mineral chemistry, thermobaric estimation, geochemistry analyses and isotopic ages.

Sample	Unit	Coordinates	Analyses
TC57	Daday U.	41º 11' 34"N, 33º 18' 25"E	Mineral chemistry
TC84	Daday U.	41°21'42.11"N, 33°27'59.57"E	Mineral chemistry/P-T path
TC83	Daday U.	41°21'44.58"N, 33°27'59.90"E	Mineral chemistry
FT4	Daday U.	41º21'12"N, 33º26'17"E	Apatite fission track analyses
FT6	Saka U.	41º 05' 04"N, 33º 18' 25"E	Apatite fission track analyses
8-7-11	Daday U.	41°25'10.35"N, 33°25'31.82"E	Ar-Ar muscovite dating
4-5-12	Daday U.	41°20'59.63"N, 33°28'36.49"E	Ar-Ar muscovite dating
IPS-10-16	Daday U.	41°18'04.61"N, 33°23'45.78"E	Geochemistry
IPS-10-18	Daday U.	41°18'04.61"N, 33°23'45.78"E	Geochemistry
7-7-11-1	Daday U.	41°20'56.02"N, 33°28'20.11"E	Geochemistry
7-7-11-3	Daday U.	41°20'59.97"N, 33°28'31.10"E	Geochemistry
7-7-11-4	Daday U.	41°20'59.97"N, 33°28'31.10"E	Geochemistry

Geological Magazine

Supplementary Material

Burial and exhumation history of the Daday Unit (Central Pontides, Turkey): implications for the closure of the Intra-Pontide oceanic basin.

Frassi C., Marroni M., Pandolfi L., Göncüoğlu M. C., Ellero A., Ottria G., Sayit K., McDonald C. S., Balestrieri M. L., Malasoma A.

Supplementary Material S4: Geochemical data of the studied mafic rocks.

Sample	*IPS-10-16*	*IPS-10-18*	*7-7-11-4*	*7-7-11-1*	*7-7-11-3*
SiO2	43.07	44.34	44.71	49.38	51.05
Al2O3	20.64	11.49	18.94	4.89	4.52
Fe2O3	12.03	12.73	9.11	7.74	7.43
MgO	3.49	5.94	7.01	21.37	17.04
CaO	9.65	11.47	10.89	11.59	16.83
Na2O	2.96	1.21	2.48	0.31	0.46
K2O	1.46	0.11	0.37	0.04	0.05
TiO2	1.72	2.13	1.05	0.07	0.27
P2O5	0.15	0.19	0.04	<0.01	<0.01
MnO	0.14	0.23	0.15	0.15	0.16
Cr2O3	0.076	0.026	0.013	0.104	0.440
LOI	4.4	9.9	5.0	3.9	1.3
Sum	99.79	99.78	99.80	99.60	99.59
Ni	149.9	40.8	7.7	99.2	63.6
Sc	45	40	43	53	82
V	230	381	279	229	274
Co	54.6	37.6	30.6	47.6	44.7
Ba	123	6	80	2	4
Rb	34.5	4.8	6.8	b.d.	0.3
Sr	564.2	276.2	266.0	7.0	10.8
U	0.6	0.2	0.2	b.d.	b.d.
Pb	1.8	2	1.0	0.2	0.2
Th	0.3	0.3	0.7	b.d.	b.d.
Hf	3.3	3.6	0.4	0.2	0.2
Nb	3.7	2.9	2.0	0.4	b.d.
Ta	0.2	0.2	0.1	b.d.	b.d.
Zr	123.3	124.2	16.0	7.4	4.9
Y	29.9	42.8	7.5	1.7	6.5
La	9	4.2	4.4	0.6	0.7
Ce	17.2	13.9	7.2	0.6	1.4
Pr	3.09	2.39	0.98	0.05	0.18
Nd	14.7	13	4.8	<0.3	1.5
Sm	4.21	4.58	1.12	0.09	0.46
Eu	1.59	1.52	0.74	0.03	0.20
Gd	5.16	6.16	1.27	0.15	0.88

Tb	0.94	1.21	0.22	0.03	0.19
Dy	5.57	7.32	1.40	0.24	1.35
Ho	1.21	1.58	0.31	0.07	0.28
Er	3.36	4.84	0.85	0.20	0.78
Tm	0.5	0.72	0.11	0.04	0.11
Yb	3.03	4.67	0.78	0.22	0.65
Lu	0.46	0.73	0.12	0.03	0.09

phengite

Geological Magazine

Supplementary Material

Burial and exhumation history of the Daday Unit (Central Pontides, Turkey): implications

Frassi C., Marroni M., Pandolfi L., Göncüoğlu M. C., Ellero A., Ottria G., Sayit K., McDonald

Supplementary Material S4. Mineral chemistry.

Sample	TC84	TC84	TC84	TC84	TC84	TC84	TC84	TC84	TC84	TC84	TC84
site	Syn-S2	Syn-S2	Syn-S2	Syn-S2	Syn-S2	Syn-S2	Syn-S2	Syn-S1	Syn-S1	Syn-S2	Syn-S1
Phengite	24	29	30	35	34	39	42	44	45	47	51
Wt%											
SiO2	50.60	50.13	48.40	50.43	47.37	47.72	46.80	46.87	50.62	51.04	48.19
TiO2	0.23	0.19	0.25	0.20	0.31	0.38	0.35	0.34	0.17	0.21	0.47
Al2O3	29.07	28.91	31.65	28.74	30.09	32.85	34.74	35.53	28.65	27.80	31.96
FeO	2.65	3.06	2.59	2.58	2.46	2.33	1.62	1.69	2.87	3.38	2.43
MnO	0.03	0.03	0.00	0.02	0.00	0.04	0.02	0.02	0.00	0.00	0.00
MgO	2.79	2.60	1.89	3.00	2.03	1.72	1.13	1.24	2.63	2.70	1.93
CaO	0.02	0.03	0.01	0.02	0.13	0.02	0.00	0.01	0.01	0.00	0.00
Na2O	0.30	0.28	0.48	0.30	0.38	0.60	0.63	0.45	0.22	0.14	0.36
K2O	9.65	9.67	9.54	9.70	9.47	9.59	9.71	9.86	9.85	9.97	9.83
Sum	95.34	94.90	94.80	94.99	92.24	95.25	95.00	95.99	95.02	95.24	95.17
Cations											
Si	3.36	3.35	3.23	3.36	3.26	3.17	3.11	3.09	3.38	3.41	3.21
Al vi	0.64	0.65	0.77	0.64	0.74	0.83	0.89	0.91	0.62	0.59	0.79
Sum Z	4.00	4.00	4.00	4.00	4.00	4.00	4.00	4.00	4.00	4.00	4.00
Al iv	1.63	1.63	1.73	1.62	1.69	1.75	1.84	1.84	1.63	1.59	1.72
Ti	0.01	0.01	0.01	0.01	0.02	0.02	0.02	0.02	0.01	0.01	0.02
Fe3+	0.00	0.00	0.00	0.00	0.00	0.00	0.00	0.00	0.00	0.00	0.00
Fe2+	0.15	0.17	0.14	0.14	0.14	0.13	0.09	0.09	0.16	0.19	0.14
Mn	0.00	0.00	0.00	0.00	0.00	0.00	0.00	0.00	0.00	0.00	0.00
Mg	0.28	0.26	0.19	0.30	0.21	0.17	0.11	0.12	0.26	0.27	0.19
Sum Y	2.07	2.07	2.07	2.07	2.06	2.07	2.06	2.08	2.06	2.06	2.07
Ca	0.00	0.00	0.00	0.00	0.01	0.00	0.00	0.00	0.00	0.00	0.00
Na	0.04	0.04	0.06	0.04	0.05	0.08	0.08	0.06	0.03	0.02	0.05
K	0.82	0.82	0.81	0.82	0.83	0.81	0.82	0.83	0.84	0.85	0.84
Sum X	0.86	0.86	0.87	0.86	0.89	0.89	0.90	0.89	0.87	0.87	0.88
OH-	0.00	0.00	0.00	0.00	0.00	0.00	0.00	0.00	0.00	0.00	0.00
F	0.00	0.00	0.00	0.00	0.00	0.00	0.00	0.00	0.00	0.00	0.00
Cl	0.00	0.00	0.00	0.00	0.00	0.00	0.00	0.00	0.00	0.00	0.00
Sum	6.92	6.93	6.95	6.93	6.95	6.96	6.96	6.96	6.92	6.92	6.95

Sample	TC57	TC57	TC57	TC57	TC57	TC57	TC57	TC57	TC57	TC57	TC57
site	syn-S2	syn-S2	syn-S2	syn-S2	syn-S2	syn-S1	syn-S2	syn-S2	syn-S1	syn-S1	syn-S1
Phengite	165	167	169	171	174	176	177	179	180	182	184
Wt%											

phengite

SiO2	47.59	47.16	47.17	46.22	47.05	46.17	47.17	46.62	48.41	47.67	46.46
TiO2	0.16	0.13	0.25	0.35	0.16	0.19	0.10	0.09	0.30	0.20	0.17
Al2O3	36.75	36.01	33.92	35.11	35.99	35.20	36.71	35.96	33.10	34.81	34.00
FeO	1.30	1.77	2.52	1.59	1.76	1.62	1.22	1.26	2.21	1.85	3.42
MnO	0.00	0.00	0.00	0.03	0.01	0.00	0.04	0.02	0.00	0.00	0.03
MgO	0.89	0.80	1.27	0.84	0.97	0.98	0.78	0.78	1.38	1.16	1.49
CaO	0.07	0.05	0.04	0.02	0.01	0.03	0.03	0.03	0.00	0.01	0.04
Na2O	0.86	1.03	0.99	0.85	1.00	0.88	0.80	0.75	0.86	1.00	0.84
K2O	9.61	9.21	9.58	9.86	9.59	9.65	9.84	9.87	9.69	9.72	9.35
Sum	97.22	96.16	95.73	94.86	96.54	94.72	96.69	95.37	95.95	96.42	95.80
Cations											
Si	3.08	3.09	3.13	3.09	3.08	3.08	3.08	3.09	3.19	3.13	3.09
Al vi	0.92	0.91	0.87	0.91	0.92	0.92	0.92	0.91	0.81	0.87	0.91
Sum Z	4.00	4.00	4.00	4.00	4.00	4.00	4.00	4.00	4.00	4.00	4.00
Al iv	1.89	1.87	1.78	1.85	1.86	1.85	1.90	1.89	1.77	1.82	1.76
Ti	0.01	0.01	0.01	0.02	0.01	0.01	0.00	0.00	0.01	0.01	0.01
Fe3+	0.00	0.00	0.00	0.00	0.00	0.00	0.00	0.00	0.00	0.00	0.00
Fe2+	0.07	0.10	0.14	0.09	0.10	0.09	0.07	0.07	0.12	0.10	0.19
Mn	0.00	0.00	0.00	0.00	0.00	0.00	0.00	0.00	0.00	0.00	0.00
Mg	0.09	0.08	0.13	0.08	0.10	0.10	0.08	0.08	0.14	0.11	0.15
Sum Y	2.05	2.06	2.06	2.04	2.06	2.05	2.05	2.04	2.04	2.04	2.11
Ca	0.00	0.00	0.00	0.00	0.00	0.00	0.00	0.00	0.00	0.00	0.00
Na	0.11	0.13	0.13	0.11	0.13	0.11	0.10	0.10	0.11	0.13	0.11
K	0.79	0.77	0.81	0.84	0.80	0.82	0.82	0.83	0.82	0.81	0.79
Sum X	0.91	0.90	0.94	0.95	0.93	0.94	0.92	0.93	0.93	0.94	0.90
OH-	0.00	0.00	0.00	0.00	0.00	0.00	0.00	0.00	0.00	0.00	0.00
F	0.00	0.00	0.00	0.00	0.00	0.00	0.00	0.00	0.00	0.00	0.00
Cl	0.00	0.00	0.00	0.00	0.00	0.00	0.00	0.00	0.00	0.00	0.00
Sum	6.96	6.96	7.00	6.99	6.99	6.99	6.97	6.97	6.97	6.99	7.02

phengite

s for the closure of the Intra-Pontide oceanic ba

C. S., Balestrieri M. L., Malasoma A.

TC84 Syn-S2 52	TC84 Syn-S2 56	TC84 Syn-S1 58	TC84 Syn-S2 60	TC84 Syn-S2 64	TC84 Syn-S1 65	TC84 Syn-S1 67	TC84 Syn-S2 68	TC84 Syn-S1 71	TC84 Syn-S2 73	TC84 Syn-S1 81	TC84 Syn-S2 84
49.81	49.07	46.48	49.17	46.31	49.44	44.97	48.74	47.17	48.57	48.89	48.67
0.25	0.32	0.24	0.34	0.37	0.22	0.41	0.29	0.44	0.28	0.12	0.17
29.73	30.01	36.23	30.27	35.39	28.07	36.75	31.01	31.96	29.78	27.19	29.05
2.67	2.94	1.42	2.99	1.71	3.30	1.63	2.59	2.36	3.16	4.59	3.28
0.02	0.00	0.03	0.03	0.02	0.05	0.06	0.00	0.02	0.01	0.03	0.00
2.50	2.49	0.96	2.30	1.21	2.68	0.95	2.29	1.86	2.57	3.26	2.76
0.01	0.01	0.00	0.01	0.00	0.00	0.00	0.04	0.00	0.00	0.03	0.02
0.35	0.35	0.80	0.31	0.84	0.31	0.54	0.26	0.56	0.38	0.14	0.31
9.69	9.87	9.73	9.78	9.38	9.83	10.14	9.86	9.56	9.75	9.24	9.70
95.02	95.05	95.90	95.19	95.23	93.91	95.45	95.08	93.93	94.50	93.48	93.97
3.32	3.28	3.06	3.28	3.07	3.35	2.99	3.25	3.19	3.27	3.34	3.30
0.68	0.72	0.94	0.72	0.93	0.65	1.01	0.75	0.81	0.73	0.66	0.70
4.00	4.00	4.00	4.00	4.00	4.00	4.00	4.00	4.00	4.00	4.00	4.00
1.65	1.65	1.87	1.66	1.84	1.60	1.87	1.69	1.73	1.64	1.54	1.62
0.01	0.02	0.01	0.02	0.02	0.01	0.02	0.01	0.02	0.01	0.01	0.01
0.00	0.00	0.00	0.00	0.00	0.00	0.00	0.00	0.00	0.00	0.00	0.00
0.15	0.16	0.08	0.17	0.09	0.19	0.09	0.14	0.13	0.18	0.26	0.19
0.00	0.00	0.00	0.00	0.00	0.00	0.00	0.00	0.00	0.00	0.00	0.00
0.25	0.25	0.09	0.23	0.12	0.27	0.09	0.23	0.19	0.26	0.33	0.28
2.07	2.08	2.06	2.08	2.07	2.07	2.08	2.08	2.07	2.09	2.14	2.09
0.00	0.00	0.00	0.00	0.00	0.00	0.00	0.00	0.00	0.00	0.00	0.00
0.05	0.04	0.10	0.04	0.11	0.04	0.07	0.03	0.07	0.05	0.02	0.04
0.82	0.84	0.82	0.83	0.79	0.85	0.86	0.84	0.82	0.84	0.81	0.84
0.87	0.89	0.92	0.87	0.90	0.89	0.93	0.88	0.90	0.89	0.83	0.88
0.00	0.00	0.00	0.00	0.00	0.00	0.00	0.00	0.00	0.00	0.00	0.00
0.00	0.00	0.00	0.00	0.00	0.00	0.00	0.00	0.00	0.00	0.00	0.00
0.00	0.00	0.00	0.00	0.00	0.00	0.00	0.00	0.00	0.00	0.00	0.00
6.93	6.96	6.98	6.95	6.98	6.96	7.01	6.95	6.97	6.97	6.97	6.97

TC57 syn-S2 185	TC57 syn-S1 187	TC57 syn-S1 189	TC57 syn-S1 193	TC57 syn-S1 195	TC57 syn-S1 187

phengite

47.44	41.10	41.64	39.74	38.90	41.10
0.20	0.17	0.08	0.06	0.11	0.17
35.21	31.67	31.77	31.23	30.77	31.67
1.84	1.06	1.22	2.46	3.46	1.06
0.00	0.01	0.00	0.08	0.06	0.01
0.96	0.73	0.69	2.63	1.55	0.73
0.03	0.06	0.02	0.04	0.03	0.06
0.89	0.84	0.80	0.46	0.64	0.84
9.67	7.82	7.88	5.89	6.83	7.82
96.24	83.45	84.11	82.59	82.35	83.45
3.12	3.09	3.11	3.01	3.00	3.09
0.88	0.91	0.89	0.99	1.00	0.91
4.00	4.00	4.00	4.00	4.00	4.00
1.84	1.90	1.90	1.80	1.80	1.90
0.01	0.01	0.00	0.00	0.01	0.01
0.00	0.00	0.00	0.00	0.00	0.00
0.10	0.07	0.08	0.16	0.22	0.07
0.00	0.00	0.00	0.00	0.00	0.00
0.09	0.08	0.08	0.30	0.18	0.08
2.05	2.06	2.06	2.27	2.21	2.06
0.00	0.00	0.00	0.00	0.00	0.00
0.11	0.12	0.12	0.07	0.10	0.12
0.81	0.75	0.75	0.57	0.67	0.75
0.92	0.88	0.87	0.64	0.77	0.88
0.00	0.00	0.00	0.00	0.00	0.00
0.00	0.00	0.00	0.00	0.00	0.00
0.00	0.00	0.00	0.00	0.00	0.00
6.97	6.93	6.92	6.91	6.98	6.93

phengite

TC84 Syn-S2 86	TC84 Syn-S2 87	TC84 Syn-S2 89	TC84 Syn-S1 92	TC84 Syn-S2 95	TC84 Syn-S1 98	TC84 Syn-S2 100
46.07	49.68	46.90	49.69	47.90	49.23	50.11
0.43	0.14	0.42	0.26	0.32	0.22	0.21
35.20	28.72	34.04	29.69	32.66	30.74	28.30
1.60	3.65	2.00	3.31	2.50	2.56	3.25
0.00	0.03	0.03	0.00	0.34	0.00	0.00
1.19	2.78	1.41	2.82	1.84	2.25	2.73
0.00	0.02	0.01	0.00	0.05	0.01	0.00
0.86	0.24	0.63	0.36	0.43	0.30	0.19
9.43	9.81	9.75	9.46	9.66	9.90	9.84
94.79	95.07	95.20	95.60	95.71	95.21	94.63
3.07	3.33	3.12	3.30	3.18	3.28	3.37
0.93	0.67	0.88	0.70	0.82	0.72	0.63
4.00	4.00	4.00	4.00	4.00	4.00	4.00
1.84	1.60	1.79	1.62	1.73	1.69	1.60
0.02	0.01	0.02	0.01	0.02	0.01	0.01
0.00	0.00	0.00	0.00	0.00	0.00	0.00
0.09	0.20	0.11	0.18	0.14	0.14	0.18
0.00	0.00	0.00	0.00	0.02	0.00	0.00
0.12	0.28	0.14	0.28	0.18	0.22	0.27
2.07	2.09	2.07	2.10	2.09	2.07	2.07
0.00	0.00	0.00	0.00	0.00	0.00	0.00
0.11	0.03	0.08	0.05	0.06	0.04	0.02
0.80	0.84	0.83	0.80	0.82	0.84	0.84
0.91	0.87	0.91	0.85	0.88	0.88	0.87
0.00	0.00	0.00	0.00	0.00	0.00	0.00
0.00	0.00	0.00	0.00	0.00	0.00	0.00
0.00	0.00	0.00	0.00	0.00	0.00	0.00
6.98	6.96	6.98	6.95	6.96	6.95	6.94

chlorite

Geological Magazine

Supplementary Material

Burial and exhumation history of the Daday Unit (Central Pontides, Turkey): implicat

Frassi C., Marroni M., Pandolfi L., Göncüoğlu M. C., Ellero A., Ottria G., Sayit K., McDon

Supplementary Material S4. Mineral chemistry.

Sample	TC84	TC84	TC84	TC84	TC84	TC84	TC84	TC84	TC84	TC84
site	syn-S2	syn-S2	syn-S2	syn-S2	syn-S2	syn-S2	syn-S2	syn-S1	syn-S2	syn-S1
Chlorite	25	28	31	32	33	38	41	46	48	50
Wt%										
SIO2	25.78	26.20	26.35	25.27	25.63	24.52	25.22	26.26	25.75	26.02
TIO2	0.11	0.06	0.09	0.02	0.08	0.06	0.06	0.10	0.09	0.10
Al2O3	23.11	21.52	21.88	23.43	23.26	23.57	23.47	21.91	23.20	22.48
FeO	24.61	24.01	23.33	24.90	24.06	23.41	23.41	25.47	23.70	23.57
MnO	0.19	0.18	0.28	0.21	0.23	0.15	0.18	0.16	0.26	0.21
MgO	14.41	16.14	16.38	14.38	15.86	15.12	15.57	13.63	15.64	15.58
CaO	0.06	0.02	0.10	0.06	0.08	0.02	0.04	0.09	0.01	0.02
Na2O	0.04	0.01	0.01	0.00	0.01	0.01	0.01	0.04	0.00	0.00
K2O	0.15	0.02	0.01	0.01	0.02	0.01	0.05	0.03	0.01	0.08
F	0.00	0.00	0.00	0.00	0.00	0.00	0.00	0.00	0.00	0.00
Cl	0.00	0.00	0.00	0.00	0.00	0.00	0.00	0.00	0.00	0.00
Sum	88.46	88.16	88.43	88.27	89.23	86.87	88.01	87.69	88.66	88.06
Cations										
Si	2.67	2.72	2.72	2.63	2.63	2.58	2.62	2.76	2.65	2.70
Al vi	1.33	1.28	1.28	1.37	1.37	1.42	1.38	1.24	1.35	1.30
Sum Z	4.00	4.00	4.00	4.00	4.00	4.00	4.00	4.00	4.00	4.00
Al iv	1.50	1.35	1.38	1.51	1.44	1.50	1.48	1.47	1.47	1.44
Ti	0.01	0.00	0.01	0.00	0.01	0.00	0.00	0.01	0.01	0.01
Fe3+	0.00	0.00	0.00	0.00	0.00	0.00	0.00	0.00	0.00	0.00
Fe2+	2.13	2.08	2.01	2.17	2.06	2.06	2.03	2.24	2.04	2.04
Mn	0.02	0.02	0.02	0.02	0.02	0.01	0.02	0.01	0.02	0.02
Mg	2.23	2.50	2.52	2.23	2.42	2.37	2.41	2.13	2.40	2.41
Sum Y	5.88	5.95	5.93	5.92	5.95	5.95	5.94	5.86	5.93	5.92
Ca	0.01	0.00	0.01	0.01	0.01	0.00	0.00	0.01	0.00	0.00
Na	0.01	0.00	0.00	0.00	0.00	0.00	0.00	0.01	0.00	0.00
K	0.02	0.00	0.00	0.00	0.00	0.00	0.01	0.00	0.00	0.01
Sum X	0.03	0.01	0.01	0.01	0.01	0.01	0.01	0.02	0.00	0.01
OH-	0.00	0.00	0.00	0.00	0.00	0.00	0.00	0.00	0.00	0.00
F	0.00	0.00	0.00	0.00	0.00	0.00	0.00	0.00	0.00	0.00
Cl	0.00	0.00	0.00	0.00	0.00	0.00	0.00	0.00	0.00	0.00
Sum	9.92	9.96	9.95	9.93	9.96	9.96	9.95	9.88	9.94	9.93

chlorite

Sample site	TC57 syn-S2	TC57 syn-S2	TC57 syn-S2	TC57 syn-S2	TC57 syn-S2	TC57 syn-S1	TC57 syn-S2	TC57 syn-S1	TC57 syn-S1	TC57 syn-S2
Chlorite	166	168	170	172	173	175	178	181	183	186
Wt%										
SIO2	25.36	25.04	25.51	27.64	24.54	25.60	25.00	24.83	24.43	24.84
TIO2	0.03	0.05	0.13	0.05	0.08	0.10	0.00	0.07	0.08	0.05
Al2O3	23.43	23.02	23.20	22.94	23.67	22.21	23.27	23.28	23.46	23.14
FeO	28.99	29.26	28.68	27.08	28.90	29.56	28.54	28.92	29.38	29.51
MnO	0.42	0.39	0.47	0.39	0.33	0.35	0.45	0.43	0.38	0.41
MgO	10.94	11.19	10.77	9.90	10.97	10.82	11.84	11.13	11.21	11.13
CaO	0.07	0.08	0.12	0.11	0.06	0.10	0.05	0.02	0.02	0.04
Na2O	0.04	0.00	0.05	0.07	0.00	0.03	0.01	0.01	0.03	0.02
K2O	0.24	0.03	0.14	1.13	0.07	0.25	0.07	0.09	0.05	0.13
F	0.00	0.00	0.00	0.00	0.00	0.00	0.00	0.00	0.00	0.00
Cl	0.00	0.00	0.00	0.00	0.00	0.00	0.00	0.00	0.00	0.00
Sum	89.52	89.07	89.06	89.30	88.63	89.02	89.23	88.78	89.04	89.26
Cations										
Si	2.66	2.65	2.69	2.88	2.60	2.71	2.63	2.63	2.59	2.63
Al vi	1.34	1.35	1.31	1.12	1.40	1.29	1.37	1.37	1.41	1.37
Sum Z	4.00	4.00	4.00	4.00	4.00	4.00	4.00	4.00	4.00	4.00
Al iv	1.56	1.52	1.57	1.69	1.56	1.49	1.51	1.54	1.52	1.51
Ti	0.00	0.00	0.01	0.00	0.01	0.01	0.00	0.01	0.01	0.00
Fe3+	0.00	0.00	0.00	0.00	0.00	0.00	0.00	0.00	0.00	0.00
Fe2+	2.54	2.59	2.53	2.36	2.56	2.62	2.51	2.56	2.60	2.61
Mn	0.04	0.04	0.04	0.03	0.03	0.03	0.04	0.04	0.03	0.04
Mg	1.71	1.76	1.69	1.53	1.73	1.71	1.85	1.76	1.77	1.75
Sum Y	5.86	5.90	5.83	5.62	5.90	5.86	5.92	5.90	5.93	5.91
Ca	0.01	0.01	0.01	0.01	0.01	0.01	0.01	0.00	0.00	0.00
Na	0.01	0.00	0.01	0.01	0.00	0.01	0.00	0.00	0.01	0.00
K	0.03	0.00	0.02	0.15	0.01	0.03	0.01	0.01	0.01	0.02
Sum X	0.05	0.01	0.04	0.17	0.02	0.05	0.02	0.02	0.02	0.03
OH-	0.00	0.00	0.00	0.00	0.00	0.00	0.00	0.00	0.00	0.00
F	0.00	0.00	0.00	0.00	0.00	0.00	0.00	0.00	0.00	0.00
Cl	0.00	0.00	0.00	0.00	0.00	0.00	0.00	0.00	0.00	0.00
Sum	9.91	9.92	9.88	9.79	9.91	9.91	9.93	9.92	9.95	9.94

chlorite

tions for the closure of the Intra-Pontide oceanic ba

ıald C. S., Balestrieri M. L., Malasoma A.

TC84 syn-S2 53	TC84 syn-S2 55	TC84 syn-S2 57	TC84 syn-S1 59	TC84 syn-S2 61	TC84 syn-S2 63	TC84 syn-S1 66	TC84 syn-S2 69	TC84 syn-S1 72	TC84 syn-S2 74	TC84 syn-S1 75	TC84 syn-S1 77
26.01	26.02	25.51	25.32	25.75	25.18	26.38	25.54	25.01	24.73	24.68	25.01
0.04	0.06	0.07	0.09	0.01	0.05	0.08	0.10	0.12	0.04	0.07	0.08
22.37	22.08	23.15	24.21	22.21	23.00	21.24	22.54	23.12	22.97	23.18	22.71
23.36	23.54	23.24	22.83	23.64	23.61	24.51	23.17	23.00	23.47	23.46	23.05
0.20	0.23	0.23	0.22	0.16	0.15	0.12	0.16	0.17	0.14	0.24	0.24
16.21	15.99	16.00	15.39	14.89	15.82	14.96	16.17	15.97	15.58	15.12	15.76
0.01	0.01	0.01	0.06	0.03	0.02	0.05	0.05	0.02	0.02	0.02	0.03
0.00	0.06	0.00	0.00	0.04	0.00	0.02	0.00	0.01	0.00	0.01	0.00
0.01	0.03	0.01	0.02	0.05	0.01	0.04	0.06	0.01	0.02	0.08	0.13
0.00	0.00	0.00	0.00	0.00	0.00	0.00	0.00	0.00	0.00	0.00	0.00
0.00	0.00	0.00	0.00	0.00	0.00	0.00	0.00	0.00	0.00	0.00	0.00
88.21	88.02	88.22	88.14	86.78	87.84	87.41	87.79	87.42	86.98	86.85	87.00
2.69	2.70	2.64	2.61	2.71	2.62	2.77	2.65	2.61	2.60	2.60	2.63
1.31	1.30	1.36	1.39	1.29	1.38	1.23	1.35	1.39	1.40	1.40	1.37
4.00	4.00	4.00	4.00	4.00	4.00	4.00	4.00	4.00	4.00	4.00	4.00
1.41	1.40	1.45	1.55	1.47	1.44	1.40	1.41	1.45	1.45	1.48	1.44
0.00	0.00	0.01	0.01	0.00	0.00	0.01	0.01	0.01	0.00	0.01	0.01
0.00	0.00	0.00	0.00	0.00	0.00	0.00	0.00	0.00	0.00	0.00	0.00
2.02	2.04	2.01	1.97	2.08	2.05	2.15	2.01	2.00	2.06	2.07	2.02
0.02	0.02	0.02	0.02	0.01	0.01	0.01	0.01	0.01	0.01	0.02	0.02
2.50	2.47	2.46	2.36	2.34	2.45	2.34	2.50	2.48	2.44	2.37	2.46
5.95	5.94	5.95	5.91	5.90	5.96	5.90	5.95	5.96	5.97	5.95	5.95
0.00	0.00	0.00	0.01	0.00	0.00	0.01	0.01	0.00	0.00	0.00	0.00
0.00	0.01	0.00	0.00	0.01	0.00	0.00	0.00	0.00	0.00	0.00	0.00
0.00	0.00	0.00	0.00	0.01	0.00	0.01	0.01	0.00	0.00	0.01	0.02
0.00	0.02	0.00	0.01	0.02	0.00	0.02	0.01	0.00	0.01	0.01	0.02
0.00	0.00	0.00	0.00	0.00	0.00	0.00	0.00	0.00	0.00	0.00	0.00
0.00	0.00	0.00	0.00	0.00	0.00	0.00	0.00	0.00	0.00	0.00	0.00
0.00	0.00	0.00	0.00	0.00	0.00	0.00	0.00	0.00	0.00	0.00	0.00
9.95	9.95	9.95	9.91	9.92	9.97	9.92	9.96	9.96	9.97	9.96	9.97

chlorite

TC57 syn-S1 188	TC57 syn-S1 190	TC57 syn-S1 192	TC57 syn-S1 194	TC57 syn-S2 196	TC57 syn-S1 199	TC57 syn-S1 201	TC57 syn-S1 203	TC57 syn-S2 205	TC57 syn-S1 208	TC57 syn-S1 210
22.43	21.27	23.12	22.75	25.15	24.88	25.36	25.33	25.19	24.95	24.64
0.00	0.01	0.08	0.03	0.04	0.07	0.06	0.05	0.06	0.06	0.08
20.88	19.96	22.18	20.59	18.96	23.01	23.31	22.64	23.15	23.31	23.33
19.85	16.30	18.52	19.63	18.69	29.42	28.75	28.80	29.56	28.93	29.64
0.31	0.24	0.20	0.26	0.28	0.36	0.36	0.45	0.36	0.41	0.26
10.23	9.04	8.76	10.09	9.87	11.26	10.68	11.50	10.97	11.54	11.06
0.04	0.12	0.06	0.02	0.07	0.00	0.06	0.04	0.06	0.00	0.01
0.01	0.00	0.08	0.00	0.17	0.02	0.00	0.00	0.00	0.06	0.01
0.14	0.12	0.72	0.10	0.73	0.08	0.22	0.09	0.13	0.04	0.04
0.00	0.00	0.00	0.00	0.00	0.00	0.00	0.00	0.00	0.00	0.00
0.00	0.00	0.00	0.00	0.00	0.00	0.00	0.00	0.00	0.00	0.00
73.90	67.06	73.72	73.46	73.96	89.10	88.79	88.90	89.47	89.30	89.07
2.75	2.83	2.82	2.80	3.06	2.63	2.68	2.68	2.65	2.63	2.61
1.25	1.17	1.18	1.20	0.94	1.37	1.32	1.32	1.35	1.37	1.39
4.00	4.00	4.00	4.00	4.00	4.00	4.00	4.00	4.00	4.00	4.00
1.78	1.95	2.00	1.79	1.77	1.50	1.58	1.50	1.53	1.52	1.52
0.00	0.00	0.01	0.00	0.00	0.01	0.00	0.00	0.00	0.01	0.01
0.00	0.00	0.00	0.00	0.00	0.00	0.00	0.00	0.00	0.00	0.00
2.04	1.81	1.89	2.02	1.90	2.60	2.54	2.54	2.60	2.55	2.62
0.03	0.03	0.02	0.03	0.03	0.03	0.03	0.04	0.03	0.04	0.02
1.87	1.79	1.59	1.85	1.79	1.78	1.68	1.81	1.72	1.81	1.75
5.72	5.58	5.51	5.69	5.49	5.92	5.84	5.90	5.89	5.91	5.92
0.00	0.02	0.01	0.00	0.01	0.00	0.01	0.00	0.01	0.00	0.00
0.00	0.00	0.02	0.00	0.04	0.00	0.00	0.00	0.00	0.01	0.00
0.02	0.02	0.11	0.01	0.11	0.01	0.03	0.01	0.02	0.01	0.01
0.03	0.04	0.14	0.02	0.16	0.01	0.04	0.02	0.02	0.02	0.01
0.00	0.00	0.00	0.00	0.00	0.00	0.00	0.00	0.00	0.00	0.00
0.00	0.00	0.00	0.00	0.00	0.00	0.00	0.00	0.00	0.00	0.00
0.00	0.00	0.00	0.00	0.00	0.00	0.00	0.00	0.00	0.00	0.00
9.75	9.62	9.65	9.71	9.66	9.93	9.88	9.91	9.91	9.93	9.93

chlorite

TC84 syn-S1 82	TC84 syn-S2 83	TC84 syn-S2 85	TC84 syn-S2 88	TC84 syn-S2 90	TC84 syn-S1 91	TC84 syn-S2 96	TC84 syn-S1 97	TC84 syn-S2 99
25.87	24.93	25.25	25.27	25.62	25.11	25.79	25.97	25.58
0.02	0.10	0.11	0.14	0.10	0.08	0.07	0.04	0.05
22.20	23.27	23.20	23.69	23.43	23.94	22.57	21.94	21.90
24.00	23.57	23.61	23.03	23.93	23.59	24.54	24.46	25.43
0.12	0.17	0.22	0.23	0.13	0.18	0.20	0.14	0.20
14.62	15.57	16.03	15.69	15.59	15.66	15.23	15.83	14.88
0.08	0.04	0.03	0.01	0.02	0.01	0.02	0.04	0.01
0.01	0.04	0.02	0.00	0.04	0.01	0.03	0.03	0.00
0.02	0.05	0.00	0.02	0.03	0.02	0.03	0.03	0.01
0.00	0.00	0.00	0.00	0.00	0.00	0.00	0.00	0.00
0.00	0.00	0.00	0.00	0.00	0.00	0.00	0.00	0.00
86.93	87.73	88.46	88.07	88.89	88.61	88.47	88.48	88.05
2.72	2.60	2.61	2.61	2.63	2.59	2.67	2.69	2.68
1.28	1.40	1.39	1.39	1.37	1.41	1.33	1.31	1.32
4.00	4.00	4.00	4.00	4.00	4.00	4.00	4.00	4.00
1.47	1.46	1.43	1.50	1.47	1.49	1.43	1.37	1.39
0.00	0.01	0.01	0.01	0.01	0.01	0.01	0.00	0.00
0.00	0.00	0.00	0.00	0.00	0.00	0.00	0.00	0.00
2.11	2.05	2.04	1.99	2.06	2.03	2.13	2.12	2.23
0.01	0.01	0.02	0.02	0.01	0.02	0.02	0.01	0.02
2.29	2.42	2.47	2.42	2.39	2.40	2.35	2.44	2.32
5.89	5.95	5.97	5.93	5.93	5.95	5.93	5.95	5.96
0.01	0.00	0.00	0.00	0.00	0.00	0.00	0.00	0.00
0.00	0.01	0.00	0.00	0.01	0.00	0.01	0.01	0.00
0.00	0.01	0.00	0.00	0.00	0.00	0.00	0.00	0.00
0.01	0.02	0.01	0.00	0.01	0.01	0.01	0.01	0.00
0.00	0.00	0.00	0.00	0.00	0.00	0.00	0.00	0.00
0.00	0.00	0.00	0.00	0.00	0.00	0.00	0.00	0.00
0.00	0.00	0.00	0.00	0.00	0.00	0.00	0.00	0.00
9.90	9.97	9.97	9.94	9.95	9.96	9.95	9.97	9.96

amphibole

Geological Magazine

Supplementary Material

Burial and exhumation history of the Daday Unit (Central Pontides, Turkey): implications

Frassi C., Marroni M., Pandolfi L., Göncüoğlu M. C., Ellero A., Ottria G., Sayit K., McDonald C

Supplementary Material S4. Mineral chemistry.

Sample	TC82	TC82	TC82	TC82	TC82	TC82	TC82	TC82	TC82	TC82	TC82
Amphibole	4	5	6	7	10	11	13	14	17	18	19
Wt%											
SiO2	53.20	51.65	54.13	52.37	55.09	53.03	53.53	53.46	47.57	53.60	43.97
TiO2	0.32	0.06	0.00	0.10	0.11	0.06	0.08	0.07	1.15	0.07	2.74
Al2O3	2.94	4.36	4.35	4.59	1.33	4.05	3.00	2.95	10.88	3.15	10.68
FeO	15.87	18.60	12.61	15.27	14.75	15.16	14.53	14.91	9.12	15.98	15.68
MnO	0.42	0.67	0.50	0.36	0.25	0.31	0.38	0.39	0.14	0.38	0.22
MgO	13.64	10.54	14.70	13.23	14.89	13.46	14.10	13.79	16.79	13.28	12.30
CaO	12.20	12.45	10.90	11.31	12.24	12.03	12.32	11.95	11.49	11.99	10.40
Na2O	0.41	0.39	1.08	1.12	0.14	0.65	0.41	0.39	2.00	0.41	2.37
K2O	0.12	0.15	0.10	0.13	0.03	0.15	0.09	0.07	0.13	0.08	0.18
Cr2O3	0.02	0.00	0.00	0.00	0.02	0.02	0.07	0.03	0.12	0.07	0.01
Sum	99.15	98.86	98.37	98.48	98.84	98.93	98.51	98.01	99.38	99.02	98.55
Cations											
Si	7.61	7.57	7.64	7.51	7.83	7.59	7.67	7.63	6.57	7.61	6.33
Al (iv)	0.39	0.43	0.36	0.49	0.17	0.41	0.33	0.37	1.43	0.39	1.67
Sum T	8.00	8.00	8.00	8.00	8.00	8.00	8.00	8.00	8.00	8.00	8.00
Al (vi)	0.11	0.33	0.36	0.29	0.05	0.27	0.18	0.13	0.34	0.13	0.15
Ti	0.03	0.01	0.00	0.01	0.01	0.01	0.01	0.11	0.12	0.11	0.30
Cr	0.00	0.00	0.00	0.00	0.00	0.00	0.01	0.00	0.01	0.01	0.00
Fe(iii)	0.34	0.04	0.39	0.37	0.33	0.23	0.20	0.25	0.88	0.27	1.02
Fe(ii)	1.56	2.24	1.09	1.46	1.42	1.58	1.54	1.53	0.17	1.63	0.86
Mn	0.05	0.08	0.06	0.04	0.03	0.04	0.05	0.05	0.02	0.05	0.03
Mg	2.91	2.30	3.09	2.83	3.15	2.87	3.01	2.93	3.46	2.81	2.64
Sum C	5.00	5.00	5.00	5.00	5.00	5.00	5.00	5.00	5.00	5.00	5.00
Ca	1.87	1.96	1.65	1.74	1.86	1.84	1.89	1.83	1.70	1.82	1.60
Na	0.11	0.04	0.30	0.26	0.04	0.16	0.11	0.11	0.30	0.11	0.40
Sum B	1.98	2.00	1.94	2.00	1.90	2.00	2.00	1.94	2.00	1.94	2.00
Na	0.00	0.07	0.00	0.05	0.00	0.03	0.01	0.00	0.24	0.00	0.27
K	0.02	0.03	0.02	0.02	0.00	0.03	0.02	0.01	0.02	0.01	0.03
Sum A	0.02	0.09	0.02	0.07	0.00	0.05	0.02	0.01	0.26	0.01	0.30
Mg/(Mg+Fe)	0.65	0.51	0.74	0.66	0.69	0.64	0.66	0.66	0.95	0.63	0.75

amphibole

for the closure of the Intra-Pontide oceanic ba

. S., Balestrieri M. L., Malasoma A.

TC82 20	TC82 21	TC82 22
52.80	44.08	51.23
0.07	2.88	0.14
4.22	11.22	5.54
15.48	14.97	15.68
0.41	0.29	0.34
12.99	11.96	12.49
11.18	10.54	11.07
0.95	2.37	0.99
0.09	0.18	0.17
0.00	0.05	0.03
98.19	98.54	97.67
7.59	6.36	7.41
0.41	1.64	0.59
8.00	8.00	8.00
0.30	0.27	0.35
0.01	0.31	0.01
0.00	0.01	0.00
0.37	0.79	0.47
1.49	1.02	1.43
0.05	0.04	0.04
2.78	2.57	2.69
5.00	5.00	5.00
1.72	1.63	1.71
0.26	0.37	0.28
1.99	2.00	1.99
0.00	0.29	0.00
0.02	0.03	0.03
0.02	0.33	0.03
0.65	0.72	0.65

epidote

Geological Magazine

Supplementary Material

Burial and exhumation history of the Daday Unit (Central Pontides, Turkey): implicatio

Frassi C., Marroni M., Pandolfi L., Göncüoğlu M. C., Ellero A., Ottria G., Sayit K., McDonal

Supplementary Material S4. Mineral chemistry.

Sample	TC82	TC82	TC82	TC82
Epidote	8	9	15	16
Wt%				
Na2O	0.02	0.00	0.00	0.01
MgO	0.05	0.03	0.03	0.00
TiO2	0.10	0.10	0.10	0.17
MnO	0.19	0.12	0.29	0.30
K2O	0.00	0.00	0.00	0.00
Al2O3	29.17	28.39	28.84	29.62
SiO2	39.29	39.13	39.35	39.44
Cr2O3	0.00	0.02	0.03	0.00
FeO	6.50	7.56	7.19	6.31
CaO	23.94	23.73	23.49	23.84
Sum	99.27	99.08	99.33	99.69
Cations				
SiO2	1.31	1.30	1.31	1.31
TiO2	0.00	0.00	0.00	0.00
Al2O3	0.86	0.84	0.85	0.87
Cr2O3	0.00	0.00	0.00	0.00
Fe2O3	0.12	0.14	0.14	0.12
FeO	0.00	0.00	0.00	0.00
MnO	0.00	0.00	0.00	0.00
MgO	0.00	0.00	0.00	0.00
CaO	0.43	0.42	0.42	0.43
Na2O	0.00	0.00	0.00	0.00
K2O	0.00	0.00	0.00	0.00
Sum	2.72	2.71	2.72	2.74
TOT	4.59	4.61	4.59	4.57
Cations				
Si	3.00	3.01	3.01	3.00
Ti	0.01	0.01	0.01	0.01
Al iv	2.63	2.58	2.61	2.65
Cr	0.00	0.00	0.00	0.00
Fe3+	0.37	0.44	0.41	0.36
Fe2+	0.00	0.00	0.00	0.00
Mn	0.01	0.01	0.02	0.02
Mg	0.01	0.00	0.00	0.00
Ca	1.96	1.95	1.92	1.94

epidote

Na	0.00	0.00	0.00	0.00
K	0.00	0.00	0.00	0.00
Sum Z	3.00	3.00	3.00	3.00
Sum Y	3.03	3.03	3.05	3.04
Sum X	1.96	1.95	1.92	1.94
TOT	7.99	7.98	7.98	7.98
Pistacite	0.12	0.14	0.14	0.12

epidote

ns for the closure of the Intra-Pontide oceanic ba

d C. S., Balestrieri M. L., Malasoma A.

epidote

epidote

Suppl. Mat. S5

Geological Magazine

Supplementary Material

Burial and exhumation history of the Daday Unit (Central Pontides, Turkey): implications

Frassi C., Marroni M., Pandolfi L., Göncüoğlu M. C., Ellero A., Ottria G., Sayit K., McDonald

Supplementary Material S5. Thermo-baric estimations.

Sample TC84			**S1 foliation**			
σ(P)<0.08GPa σ(T)<25°C						
CHLORITE	**TC84-24**	**TC84-28**	**TC84-39**	**TC84-44**	**TC84-69**	**TC84-75**
PHENGITE	**TC84-23**	**TC84-27**	**TC84-38**	**TC84-43**	**TC84-70**	**TC84-76**
Pavg (GPa)	11853	10468	9195	11021	10786	12377
dev	680	508	247	956	862	426
Tavg (°C)	243	398	328	239	405	228
dev	22	21	5	31	28	3

Sample TC84			**S2 foliation**					
<0.08GPa σ(T)<25°C								
CHLORITE	TC84-3	TC84-6	**TC84-52**	TC84-53	TC84-55	TC84-61	TC84-66	TC84-77
PHENGITE	TC84-2	TC84-7	TC84-51	TC84-54	TC84-54	TC84-62	TC84-65	TC84-78
Pavg (GPa)	11553.11	10516.3	8377	9389.91	9494.17	9661.34	10690.99	11315.15
dev	582.89	491.18	3	753.3	799.1	725.84	840.53	775.23
Tavg (°C)	330.49	419.45	445	394.27	375.11	389.04	373.12	382.37
dev	21.53	20.9	0.05	24.92	20.19	5.77	23.83	19.84

Suppl. Mat. S5

s for the closure of the Intra-Pontide oceanic ba

C. S., Balestrieri M. L., Malasoma A.

TC84-47	TC84-20	TC84-33
TC84-46	**TC84-21**	**TC84-32**
7220	7419	6152
523	773	850
491	411	433
9.39	16	20

Sample: 4.5.12			Lab #: 836-01				
Material: White Mica							
Irradiation coordinates: 14F6							
N	Power (W)	^{40}Ar (moles)	^{40}Ar (ISO) (cps)	±σ (cps)	^{40}Ar (PLT) (cps)	±σ (cps)	^{39}Ar (cps)
A	0.5	-2.96E-18	-7.14E+01	4.64E+01	-3.56E+01	6.83E+02	2.17E+01
B	0.6	8.28E-17	2.65E+03	5.42E+01	2.80E+03	6.83E+02	5.36E+01
C	0.7	1.42E-15	4.56E+04	7.23E+01	4.15E+04	7.07E+02	4.69E+02
D	0.8	1.22E-15	3.93E+04	5.73E+01	4.00E+04	6.62E+02	4.67E+02
E	0.9	1.36E-15	4.35E+04	6.38E+01	4.33E+04	6.63E+02	5.22E+02
F	1.0	1.78E-16	5.74E+03	5.85E+01	5.48E+03	6.67E+02	6.78E+01
G	1.1	8.99E-17	2.88E+03	5.71E+01	2.33E+03	6.67E+02	4.13E+01
H	1.2	1.08E-16	3.49E+03	5.33E+01	2.43E+03	6.86E+02	5.01E+01
I	1.3	9.15E-17	2.93E+03	5.71E+01	2.99E+03	6.87E+02	3.76E+01
J	1.4	6.56E-17	2.08E+03	5.39E+01	2.98E+03	6.86E+02	2.90E+01
K	1.5	8.40E-17	2.67E+03	4.71E+01	1.62E+03	6.40E+02	3.29E+01
L	1.6	2.38E-17	7.69E+02	6.47E+01	1.99E+02	1.03E+03	4.35E+01
M	1.8	4.64E-17	1.50E+03	4.90E+01	1.03E+03	6.61E+02	3.32E+01
N	2.0	2.62E-17	8.31E+02	4.77E+01	1.20E+03	6.40E+02	1.39E+01
O	5.0	8.39E-16	2.69E+04	6.39E+01	2.62E+04	6.63E+02	2.76E+02
Plateau Age (Steps B-I)							

Sample: 4.5.12			Lab #: 836-02				
Material: White Mica							
Irradiation coordinates: 14F6							
N	Power (W)	^{40}Ar (moles)	^{40}Ar (ISO) (cps)	±σ (cps)	^{40}Ar (PLT) (cps)	±σ (cps)	^{39}Ar (cps)
A	0.6	1.07E-15	3.43E+04	5.38E+01	3.17E+04	6.94E+02	3.31E+02
B	0.7	4.95E-16	1.58E+04	5.38E+01	1.48E+04	6.73E+02	1.80E+02
C	0.8	1.56E-15	4.99E+04	5.72E+01	4.84E+04	7.38E+02	5.85E+02
D	0.9	1.84E-16	5.88E+03	4.79E+01	5.20E+03	6.73E+02	7.64E+01
E	1.0	6.69E-17	2.12E+03	4.77E+01	1.61E+03	6.41E+02	3.64E+01
F	1.5	5.42E-16	1.73E+04	5.88E+01	1.58E+04	6.00E+02	1.63E+02
G	2.0	4.19E-16	1.34E+04	5.12E+01	1.35E+04	6.20E+02	1.38E+02
H	5.0	2.29E-16	7.30E+03	5.65E+01	6.55E+03	6.21E+02	8.91E+01
Plateau Age (Steps B-D)							

Sample: 4.5.12			Lab #: 836-03				
Material: White Mica							
Irradiation coordinates: 14F6							
N	Power (W)	^{40}Ar (moles)	^{40}Ar (ISO)[3] (cps)	±σ (cps)	^{40}Ar (PLT)[4] (cps)	±σ (cps)	^{39}Ar (cps)
A	0.6	-8.39E-18	-2.43E+02	5.62E+01	-3.47E+02	1.01E+03	3.06E+01
B	0.7	1.22E-16	3.95E+03	4.92E+01	3.23E+03	6.73E+02	5.45E+01
C	0.8	2.49E-16	7.98E+03	5.00E+01	7.77E+03	6.53E+02	9.17E+01
D	0.9	3.90E-15	1.25E+05	9.98E+01	1.16E+05	7.21E+02	1.21E+03
E	1.1	3.19E-15	1.02E+05	9.61E+01	1.02E+05	6.99E+02	1.14E+03
F	1.3	5.00E-15	1.60E+05	1.15E+02	1.59E+05	7.12E+02	1.85E+03
G	1.5	4.92E-16	1.58E+04	5.25E+01	1.56E+04	6.61E+02	1.84E+02
H	2.0	5.78E-16	1.85E+04	5.81E+01	1.85E+04	6.41E+02	2.06E+02
I	5.0	1.46E-15	4.69E+04	6.23E+01	4.70E+04	6.84E+02	5.54E+02
J	8.0	2.99E-16	9.57E+03	5.25E+01	1.00E+04	6.61E+02	1.14E+02
Plateau Age (Steps F-J)							

Standards: HD-B1			Lab #: 831				
Irradiation coordinates: 14F1							
N	Power (W)	^{40}Ar (moles)	^{40}Ar (ISO)[3] (cps)	±σ (cps)	^{40}Ar (PLT)[4] (cps)	±σ (cps)	^{38}Ar (cps)
1	5.0	3.30E-16	1.05E+04	6.44E+01	5.15E+02	6.32E+00	5.58E+00
2	5.0	4.06E-16	1.29E+04	6.63E+01	8.06E+02	7.26E+00	1.07E+01
3	5.0	1.85E-15	5.88E+04	8.66E+01	4.07E+03	1.34E+01	5.56E+01
4	5.0	3.34E-15	1.06E+05	9.84E+01	7.19E+03	1.63E+01	1.01E+02
5	5.0	1.97E-15	6.26E+04	8.92E+01	4.62E+03	1.34E+01	6.30E+01

Weighted mean *J* : 0.00104950 ± 0.0000049113

Standards: HD-B1			Lab #: 833				
Irradiation coordinates: 14F3							
N	Power (W)	^{40}Ar (moles)	^{40}Ar (ISO)[3] (cps)	±σ (cps)	^{40}Ar (PLT)[4] (cps)	±σ (cps)	^{38}Ar (cps)
1	5.0	1.97E-14	6.27E+05	2.92E+02	4.72E+04	4.12E+01	6.09E+02
2	5.0	1.13E-14	3.60E+05	2.02E+02	2.68E+04	3.02E+01	3.47E+02
3	5.0	7.55E-15	2.40E+05	1.52E+02	1.86E+04	2.62E+01	2.39E+02
4	5.0	5.69E-15	1.81E+05	1.27E+02	1.36E+04	2.23E+01	1.77E+02
5	5.0	4.47E-15	1.42E+05	1.38E+02	1.06E+04	1.93E+01	1.39E+02

Weighted mean *J* : 0.00104470 ± 0.0000099887

Standards: HD-B1			Lab #: 835				
Irradiation coordinates: 14F5							
N	Power (W)	^{40}Ar (moles)	^{40}Ar (cps)	±σ (cps)	^{39}Ar (cps)	±σ (cps)	^{38}Ar (cps)
1	5.0	4.95E-15	1.57E+05	1.42E+02	1.16E+04	2.75E+01	1.49E+02
2	5.0	2.07E-14	6.57E+05	4.30E+02	4.93E+04	6.13E+01	6.36E+02
3	5.0	3.85E-15	1.22E+05	1.02E+02	9.27E+03	1.96E+01	1.20E+02
4	5.0	2.07E-15	6.56E+04	7.47E+01	4.63E+03	1.34E+01	6.98E+01
5	5.0	7.03E-15	2.23E+05	1.72E+02	1.63E+04	2.53E+01	2.19E+02

Weighted mean *J* : 0.00106520 ± 0.0000013385

Explanations

D[1]: Mass discrimination per AMU based on power law

Blank Type[2]: Ave = average; LR = linear regression versus time

^{40}Ar (ISO)[3] - non air corrected 40Ar for isochron calculations

^{40}Ar (PLT)[4] - Air corrected 40Ar for plateau calculations

N.D. : values are indistinguishable from the background measurements

Constants Used

Atmospheric argon ratios

$(^{40}Ar/^{36}Ar)_A$	295.5 ± 0.50	Nier (1950)
$(^{40}Ar/^{38}Ar)_A$	0.1880 ± 0.0001	Nier (1950)

Interfering isotope production ratios

$(^{40}Ar/^{39}Ar)_K$	(7.30 ± 0.90)E-04
$(^{38}Ar/^{39}Ar)_K$	(1.22 ± 0.00)E-02
$(^{37}Ar/^{39}Ar)_K$	(2.24 ± 0.16)E-04
$(^{39}Ar/^{37}Ar)_{Ca}$	(6.95 ± 0.09)E-04

$(^{38}Ar/^{37}Ar)_{Ca}$	(1.96 ± 0.08)E-05	
$(^{36}Ar/^{37}Ar)_{Ca}$	(2.65 ± 0.02)E-04	
$(^{36}Cl/^{38}Cl)_{Cl}$	263 ± 2	
Decay Constants		
$^{40}K\ \lambda_{\varepsilon}$	(5.81 ± 0.17)E-11	Steiger & Jäger, 1977
$^{40}K\ \lambda_{\beta}$	(4.96 ± 0.08)E-10	Steiger & Jäger, 1977
^{39}K	(2.58)E-3 a^{-1}	Stoenner et al. (1965)
^{37}K	7.232 a^{-1}	Stoenner et al. (1965)
$^{36}Cl\ \lambda_{\beta}$	(2.305)E-6 a^{-1}	Endt (1998)

J : 0.00106155 ± 0.00000481206 D^{I} : 0.997658 ± 0.000469

±σ (cps)	^{38}Ar (cps)	±σ (cps)	^{37}Ar (cps)	±σ (cps)	^{36}Ar (cps)	±σ (cps)	%^{40}Ar*	^{40}Ar*/^{39}Ar$_K$
6.25E+00	2.83E+00	1.78E+00	N.D.	6.18E+02	-1.21E-01	2.30E+00	101.5	-1.63918
5.52E+00	9.02E-01	1.70E+00	N.D.	5.72E+02	-5.06E-01	2.30E+00	103.5	52.33137
7.46E+00	3.91E+00	1.93E+00	N.D.	6.13E+02	1.39E+01	2.38E+00	90.9	88.54622
8.12E+00	N.D.	1.64E+00	N.D.	6.18E+02	-2.34E+00	2.23E+00	101.7	85.49876
6.91E+00	1.41E+00	1.86E+00	N.D.	5.88E+02	7.87E-01	2.23E+00	99.3	82.86220
4.99E+00	7.32E-01	1.59E+00	N.D.	6.58E+02	8.69E-01	2.25E+00	93.6	80.84072
5.15E+00	N.D.	1.51E+00	N.D.	5.90E+02	1.86E+00	2.25E+00	75.3	56.38645
4.68E+00	N.D.	1.67E+00	8.85E+02	6.28E+02	3.61E+00	2.32E+00	70.3	48.43975
4.53E+00	N.D.	1.42E+00	N.D.	6.48E+02	-1.84E-01	2.32E+00	96.3	79.39564
4.91E+00	6.66E-01	1.59E+00	N.D.	6.59E+02	-3.06E+00	2.32E+00	140.4	102.60098
4.79E+00	2.35E+00	1.82E+00	1.76E+02	6.75E+02	3.53E+00	2.16E+00	55.1	49.28402
1.05E+01	2.30E+00	2.40E+00	N.D.	1.03E+03	1.93E+00	3.47E+00	-10.0	4.56799
5.40E+00	N.D.	1.60E+00	N.D.	6.36E+02	1.59E+00	2.23E+00	51.8	30.88329
5.85E+00	N.D.	1.60E+00	N.D.	5.82E+02	-1.25E+00	2.16E+00	126.6	86.39381
6.01E+00	N.D.	1.60E+00	8.35E-01	5.78E+02	2.30E+00	2.23E+00	97.0	94.76847

J : 0.00106155 ± 0.00000481206 D^{I} : 0.997658 ± 0.000469

±σ (cps)	^{38}Ar (cps)	±σ (cps)	^{37}Ar (cps)	±σ (cps)	^{36}Ar (cps)	±σ (cps)	%^{40}Ar*	^{40}Ar*/^{39}Ar$_K$
7.43E+00	3.72E-02	1.54E+00	1.26E+03	5.96E+02	8.98E+00	2.34E+00	92.0	95.86564
6.75E+00	N.D.	1.67E+00	6.94E+02	5.96E+02	3.50E+00	2.27E+00	91.9	82.22916
6.92E+00	N.D.	1.75E+00	5.04E+02	6.53E+02	5.20E+00	2.49E+00	96.8	82.71980
5.56E+00	7.35E-01	1.67E+00	9.24E+02	5.69E+02	2.29E+00	2.27E+00	86.2	68.08237
4.87E+00	N.D.	1.67E+00	N.D.	6.80E+02	1.70E+00	2.16E+00	77.0	44.34675
6.37E+00	N.D.	1.67E+00	1.22E+02	6.41E+02	5.27E+00	2.02E+00	91.2	96.45595
6.13E+00	N.D.	1.81E+00	N.D.	7.49E+02	-2.88E-01	2.09E+00	100.7	97.90341
5.07E+00	N.D.	1.88E+00	N.D.	7.12E+02	2.55E+00	2.09E+00	89.6	73.48631

J : 0.00106155 ± 0.00000481206 D^{I} : 0.997658 ± 0.000469

±σ (cps)	^{38}Ar (cps)	±σ (cps)	^{37}Ar (cps)	±σ (cps)	^{36}Ar (cps)	±σ (cps)	%^{40}Ar*	^{40}Ar*/^{39}Ar$_K$
9.16E+00	N.D.	2.75E+00	N.D.	7.78E+02	3.51E-01	3.41E+00	222.3	-11.34233
5.71E+00	2.49E-01	1.59E+00	N.D.	6.53E+02	2.44E+00	2.27E+00	77.6	59.26239
5.39E+00	N.D.	1.59E+00	6.36E+02	6.80E+02	7.14E-01	2.20E+00	96.6	84.74010
9.72E+00	4.83E+00	2.00E+00	N.D.	6.22E+02	3.20E+01	2.42E+00	92.3	95.57903
9.44E+00	2.98E-01	2.08E+00	2.41E+01	6.75E+02	2.73E+00	2.34E+00	99.1	88.89517
1.03E+01	5.04E-01	2.11E+00	6.86E+02	5.99E+02	3.00E+00	2.38E+00	99.4	86.11975
6.31E+00	2.36E+00	1.73E+00	N.D.	6.39E+02	6.74E-01	2.23E+00	97.9	84.60673
5.77E+00	9.05E-01	1.66E+00	N.D.	6.71E+02	8.93E-02	2.16E+00	98.9	90.04528
7.21E+00	1.46E+00	1.67E+00	7.48E+02	6.55E+02	-3.21E-01	2.30E+00	99.8	84.76291
6.15E+00	N.D.	1.59E+00	4.47E+02	6.35E+02	-1.47E+00	2.23E+00	101.9	88.01867

Age: 24.18 Ma D^{1}: 0.9977846

±σ (cps)	^{37}Ar (cps)	±σ (cps)	^{36}Ar (cps)	±σ (cps)	%^{40}Ar*	^{40}Ar*/^{39}Ar$_K$	±σ	*J*
1.36E+00	1.40E+02	6.39E+02	1.19E+01	1.74E+00	66.4	13.49864	1.02768	9.9960E-04
1.36E+00	7.92E+02	7.79E+02	8.41E+00	1.70E+00	81.2	12.97701	0.64692	1.0398E-03
2.21E+00	N.D.	6.90E+02	1.82E+01	1.74E+00	90.8	13.08874	0.13613	1.0309E-03
2.29E+00	N.D.	7.27E+02	4.69E+01	1.86E+00	86.9	12.81535	0.08346	1.0529E-03
1.38E+00	1.15E+03	6.47E+02	1.24E+01	1.67E+00	94.3	12.74341	0.11505	1.0588E-03

Age: 24.18 Ma D^{1}: 0.9980028

±σ (cps)	^{37}Ar (cps)	±σ (cps)	^{36}Ar (cps)	±σ (cps)	%^{40}Ar*	^{40}Ar*/^{39}Ar$_K$	±σ	*J*
4.85E+00	N.D.	7.43E+02	2.58E+01	1.80E+00	98.8	13.08368	0.01735	1.0313E-03
3.27E+00	1.02E+03	6.97E+02	5.36E+01	1.90E+00	95.6	12.81752	0.02669	1.0527E-03
3.00E+00	N.D.	5.86E+02	1.98E+01	1.58E+00	97.5	12.52863	0.03179	1.0770E-03
2.89E+00	N.D.	6.08E+02	2.58E+01	1.72E+00	95.7	12.73508	0.04411	1.0595E-03
2.38E+00	6.91E+02	6.43E+02	1.67E+01	1.69E+00	96.6	12.89272	0.05438	1.0466E-03

Age: 24.18 Ma D^{1}: 0.9966905 ± 0.0003579

±σ (cps)	^{37}Ar (cps)	±σ (cps)	^{36}Ar (cps)	±σ (cps)	%^{40}Ar*	^{40}Ar*/^{39}Ar$_K$	±σ	*J*
1.53E+00	N.D.	1.06E+02	3.38E+01	1.18E+00	93.6	12.62367	0.04422	1.0689E-03
3.11E+00	N.D.	9.96E+01	1.14E+02	1.64E+00	94.9	12.63119	0.02119	1.0682E-03
1.42E+00	N.D.	1.02E+02	1.25E+01	1.03E+00	97.0	12.77003	0.04408	1.0566E-03
2.04E+00	1.20E+01	6.40E+02	1.89E+01	1.85E+00	91.5	12.94470	0.12556	1.0424E-03
2.97E+00	5.12E+02	7.40E+02	5.19E+01	1.81E+00	93.1	12.70961	0.03981	1.0617E-03

Heating: 10 s

						Blank Corrections		
±σ	Age (Ma)	±σ (Ma)	±2σ (Ma)	±σ (-J) (Ma)	Ca/K	Blank Type[2]	^{40}Ar (cps)	±σ (cps)
-31.45103	-3.14	60.34	120.68	60.34	-24.76	LR	7.29E+03	3.54E+01
13.84416	97.54	25.12	50.24	25.12	-18.27	LR	7.22E+03	3.54E+01
2.06305	162.07	3.68	7.36	3.61	-1.21	LR	7.16E+03	3.54E+01
2.05292	156.73	3.67	7.34	3.60	-0.30	LR	7.03E+03	3.54E+01
1.67648	152.10	3.02	6.04	2.95	-1.42	LR	6.97E+03	3.54E+01
11.48727	148.53	20.27	40.54	20.26	-12.17	LR	7.51E+03	4.26E+01
17.60775	104.88	31.82	63.64	31.82	-41.88	LR	7.46E+03	4.26E+01
14.42031	90.46	26.27	52.54	26.27	29.79	LR	7.35E+03	4.26E+01
20.61363	145.98	36.41	72.82	36.41	-68.00	LR	7.30E+03	4.26E+01
29.31951	186.51	50.64	101.28	50.64	-1.59	LR	7.24E+03	4.26E+01
20.72354	92.00	37.72	75.44	37.71	12.47	LR	7.36E+03	3.71E+01
23.64659	8.73	45.07	90.14	45.07	-52.42	LR	7.27E+03	3.71E+01
20.52988	58.20	38.07	76.14	38.07	-62.11	LR	7.22E+03	3.71E+01
58.65389	158.30	102.89	205.78	102.89	-10.53	LR	7.17E+03	3.71E+01
3.16094	172.93	5.55	11.10	5.50	0.28	LR	7.12E+03	3.71E+01
	153.0	**4.5**	**9.00**					

Heating: 10 s

						Blank Corrections		
±σ	Age (Ma)	±σ (Ma)	±2σ (Ma)	±σ (-J) (Ma)	Ca/K	Blank Type[2]	^{40}Ar (cps)	±σ (cps)
3.00790	174.84	5.28	10.56	5.23	6.61	LR	7.20E+03	2.78E+01
4.84334	150.98	8.56	17.12	8.53	6.04	LR	7.16E+03	2.78E+01
1.59660	151.84	2.89	5.78	2.81	1.47	LR	7.08E+03	2.78E+01
10.10024	125.89	18.05	36.10	18.04	20.00	LR	7.03E+03	2.78E+01
18.61014	82.99	34.04	68.08	34.04	-42.99	LR	7.20E+03	3.54E+01
5.25919	175.87	9.17	18.34	9.14	2.14	LR	7.14E+03	3.54E+01
6.26031	178.38	10.89	21.78	10.86	-7.64	LR	7.02E+03	3.54E+01
8.12864	135.52	14.45	28.90	14.44	-2.01	LR	6.97E+03	3.54E+01
	151.2	**5.3**	**10.60**					

Heating: 10 s

						Blank Corrections		
±σ	Age (Ma)	±σ (Ma)	±2σ (Ma)	±σ (-J) (Ma)	Ca/K	Blank Type[2]	^{40}Ar (cps)	±σ (cps)
-33.15883	-21.85	64.28	128.56	64.28	-80.48	LR	7.16E+03	3.36E+01
13.82199	110.07	24.91	49.82	24.90	-18.51	LR	7.10E+03	3.36E+01
8.68808	155.40	15.28	30.56	15.27	12.27	LR	7.05E+03	3.36E+01
0.97119	174.34	1.85	3.70	1.69	-0.19	LR	6.95E+03	3.36E+01
0.95558	162.68	1.81	3.62	1.67	-0.01	LR	6.89E+03	3.36E+01
0.61312	157.82	1.28	2.56	1.08	0.69	LR	7.07E+03	3.27E+01
4.62064	155.16	8.15	16.30	8.12	0.13	LR	7.04E+03	3.27E+01
4.01274	164.70	7.05	14.10	7.01	-1.29	LR	6.97E+03	3.27E+01
1.65476	155.44	2.98	5.96	2.91	2.58	LR	6.94E+03	3.27E+01
7.51985	161.15	13.19	26.38	13.17	7.60	LR	6.90E+03	3.27E+01
	157.7	**2.0**	**4.00**					

Heating: 10 s

±σ	Ca/K	Blank Type[2]	^{40}Ar (cps)	±σ (cps)	^{39}Ar (cps)	±σ (cps)	^{38}Ar (cps)
#########	0.48	LR	8.63E+03	5.99E+01	2.54E+02	2.98E+00	1.47E+01
#########	1.76	LR	8.48E+03	5.79E+01	2.55E+02	3.10E+00	1.37E+01
#########	-0.02	LR	8.39E+03	5.79E+01	2.52E+02	3.10E+00	1.38E+01
#########	-0.08	LR	8.20E+03	3.59E+01	2.51E+02	3.45E+00	1.46E+01
#########	0.44	LR	8.20E+03	3.59E+01	2.54E+02	3.45E+00	1.51E+01

Heating: 10 s

±σ	Ca/K	Blank Type[2]	^{40}Ar (cps)	±σ (cps)	^{39}Ar (cps)	±σ (cps)	^{38}Ar (cps)
#########	0.00	LR	9.00E+03	3.73E+01	2.56E+02	3.36E+00	1.34E+01
#########	0.07	LR	8.84E+03	3.73E+01	2.57E+02	3.36E+00	1.34E+01
#########	-0.01	LR	8.50E+03	3.73E+01	2.58E+02	3.36E+00	1.35E+01
#########	-0.14	LR	8.47E+03	7.51E+01	2.59E+02	3.52E+00	1.31E+01
#########	0.11	LR	8.61E+03	7.51E+01	2.59E+02	3.52E+00	1.26E+01

Heating: 10 s

±σ	Ca/K	Blank Type[2]	^{40}Ar (cps)	±σ (cps)	^{39}Ar (cps)	±σ (cps)	^{38}Ar (cps)
#########	-0.01	LR	3.94E+03	2.10E+01	8.45E+02	5.13E+00	2.31E+00
#########	-0.01	LR	6.09E+03	3.29E+01	9.62E+02	6.71E+00	4.11E+00
#########	-0.03	LR	1.07E+04	3.29E+01	1.20E+03	6.71E+00	8.12E+00
#########	0.00	LR	9.27E+03	4.06E+01	2.60E+02	3.43E+00	1.34E+01
#########	0.05	LR	9.11E+03	4.06E+01	2.60E+02	3.43E+00	1.32E+01

Ratios for Is

^{39}Ar (cps)	±σ (cps)	^{38}Ar (cps)	±σ (cps)	^{37}Ar (cps)	±σ (cps)	^{36}Ar (cps)	±σ (cps)	^{39}Ar/^{40}Ar
2.31E+02	4.42E+00	1.02E+01	1.21E+00	3.41E+02	5.89E+00	4.73E+01	1.56E+00	-3.04E-01
2.31E+02	4.42E+00	1.02E+01	1.21E+00	3.40E+02	5.89E+00	4.74E+01	1.56E+00	2.02E-02
2.31E+02	4.42E+00	1.03E+01	1.21E+00	3.40E+02	5.89E+00	4.75E+01	1.56E+00	1.03E-02
2.30E+02	4.42E+00	1.05E+01	1.21E+00	3.40E+02	5.89E+00	4.76E+01	1.56E+00	1.19E-02
2.30E+02	4.42E+00	1.05E+01	1.21E+00	3.39E+02	5.89E+00	4.77E+01	1.56E+00	1.20E-02
2.34E+02	3.10E+00	1.09E+01	1.04E+00	3.45E+02	6.34E+00	4.79E+01	1.67E+00	1.18E-02
2.34E+02	3.10E+00	1.10E+01	1.04E+00	3.43E+02	6.34E+00	4.77E+01	1.67E+00	1.43E-02
2.34E+02	3.10E+00	1.11E+01	1.04E+00	3.40E+02	6.34E+00	4.72E+01	1.67E+00	1.43E-02
2.35E+02	3.10E+00	1.11E+01	1.04E+00	3.39E+02	6.34E+00	4.70E+01	1.67E+00	1.28E-02
2.35E+02	3.10E+00	1.12E+01	1.04E+00	3.37E+02	6.34E+00	4.68E+01	1.67E+00	1.40E-02
2.38E+02	3.73E+00	1.24E+01	1.16E+00	3.37E+02	5.63E+00	4.75E+01	1.56E+00	1.23E-02
2.36E+02	3.73E+00	1.22E+01	1.16E+00	3.37E+02	5.63E+00	4.75E+01	1.56E+00	5.66E-02
2.35E+02	3.73E+00	1.21E+01	1.16E+00	3.37E+02	5.63E+00	4.76E+01	1.56E+00	2.22E-02
2.34E+02	3.73E+00	1.20E+01	1.16E+00	3.36E+02	5.63E+00	4.76E+01	1.56E+00	1.67E-02
2.32E+02	3.73E+00	1.19E+01	1.16E+00	3.36E+02	5.63E+00	4.76E+01	1.56E+00	1.03E-02

Ratios for Is

^{39}Ar (cps)	±σ (cps)	^{38}Ar (cps)	±σ (cps)	^{37}Ar (cps)	±σ (cps)	^{36}Ar (cps)	±σ (cps)	^{39}Ar/^{40}Ar
2.38E+02	3.75E+00	1.43E+01	1.16E+00	3.18E+02	5.34E+00	4.74E+01	1.61E+00	9.63E-03
2.38E+02	3.75E+00	1.37E+01	1.16E+00	3.19E+02	5.34E+00	4.64E+01	1.61E+00	1.14E-02
2.38E+02	3.75E+00	1.25E+01	1.16E+00	3.22E+02	5.34E+00	4.43E+01	1.61E+00	1.17E-02
2.38E+02	3.75E+00	1.18E+01	1.16E+00	3.24E+02	5.34E+00	4.32E+01	1.61E+00	1.30E-02
2.36E+02	3.66E+00	1.47E+01	1.25E+00	3.37E+02	6.67E+00	4.80E+01	1.46E+00	1.72E-02
2.37E+02	3.66E+00	1.47E+01	1.25E+00	3.36E+02	6.67E+00	4.76E+01	1.46E+00	9.43E-03
2.37E+02	3.66E+00	1.46E+01	1.25E+00	3.33E+02	6.67E+00	4.69E+01	1.46E+00	1.03E-02
2.38E+02	3.66E+00	1.46E+01	1.25E+00	3.31E+02	6.67E+00	4.66E+01	1.46E+00	1.22E-02

Ratios for Is

^{39}Ar (cps)	±σ (cps)	^{38}Ar (cps)	±σ (cps)	^{37}Ar (cps)	±σ (cps)	^{36}Ar (cps)	±σ (cps)	^{39}Ar/^{40}Ar
2.35E+02	3.37E+00	1.16E+01	1.14E+00	3.38E+02	6.11E+00	4.60E+01	1.61E+00	-1.26E-01
2.36E+02	3.37E+00	1.18E+01	1.14E+00	3.36E+02	6.11E+00	4.60E+01	1.61E+00	1.38E-02
2.37E+02	3.37E+00	1.20E+01	1.14E+00	3.35E+02	6.11E+00	4.60E+01	1.61E+00	1.15E-02
2.39E+02	3.37E+00	1.23E+01	1.14E+00	3.31E+02	6.11E+00	4.60E+01	1.61E+00	9.67E-03
2.40E+02	3.37E+00	1.25E+01	1.14E+00	3.30E+02	6.11E+00	4.61E+01	1.61E+00	1.12E-02
2.36E+02	3.83E+00	1.21E+01	1.14E+00	3.27E+02	6.23E+00	4.76E+01	1.56E+00	1.15E-02
2.37E+02	3.83E+00	1.22E+01	1.14E+00	3.28E+02	6.23E+00	4.76E+01	1.56E+00	1.17E-02
2.38E+02	3.83E+00	1.25E+01	1.14E+00	3.29E+02	6.23E+00	4.74E+01	1.56E+00	1.11E-02
2.38E+02	3.83E+00	1.26E+01	1.14E+00	3.29E+02	6.23E+00	4.73E+01	1.56E+00	1.18E-02
2.39E+02	3.83E+00	1.27E+01	1.14E+00	3.30E+02	6.23E+00	4.72E+01	1.56E+00	1.19E-02

±σ (cps)	^{37}Ar (cps)	±σ (cps)	^{36}Ar (cps)	±σ (cps)
9.21E-01	3.55E+02	5.67E+00	5.63E+01	1.25E+00
8.91E-01	3.51E+02	5.68E+00	5.46E+01	1.35E+00
8.91E-01	3.49E+02	5.68E+00	5.36E+01	1.35E+00
8.81E-01	3.48E+02	4.78E+00	5.17E+01	1.35E+00
8.81E-01	3.50E+02	4.78E+00	5.16E+01	1.35E+00

±σ (cps)	^{37}Ar (cps)	±σ (cps)	^{36}Ar (cps)	±σ (cps)
9.31E-01	3.58E+02	5.01E+00	5.55E+01	1.21E+00
9.31E-01	3.57E+02	5.01E+00	5.42E+01	1.21E+00
9.31E-01	3.57E+02	5.01E+00	5.17E+01	1.21E+00
9.28E-01	3.54E+02	4.97E+00	5.18E+01	1.26E+00
9.28E-01	3.51E+02	4.97E+00	5.32E+01	1.26E+00

±σ (cps)	^{37}Ar (cps)	±σ (cps)	^{36}Ar (cps)	±σ (cps)
2.86E-01	2.85E+02	4.10E+00	1.39E+01	6.83E-01
4.63E-01	2.84E+02	4.13E+00	1.59E+01	8.00E-01
4.63E-01	2.81E+02	4.13E+00	2.13E+01	8.00E-01
9.40E-01	3.46E+02	5.68E+00	5.73E+01	1.31E+00
9.40E-01	3.41E+02	5.68E+00	5.66E+01	1.31E+00

sochrons

±σ	$^{36}Ar/^{40}Ar$	±σ
-2.16E-01	1.70E-03	3.23E-02
2.12E-03	-1.91E-04	-8.68E-04
1.64E-04	3.05E-04	5.21E-05
2.08E-04	-5.96E-05	-5.68E-05
1.60E-04	1.81E-05	5.13E-05
8.77E-04	1.51E-04	3.92E-04
1.81E-03	6.47E-04	7.81E-04
1.36E-03	1.03E-03	6.63E-04
1.57E-03	-6.27E-05	-7.90E-04
2.39E-03	-1.47E-03	-1.12E-03
1.81E-03	1.32E-03	8.11E-04
1.45E-02	2.51E-03	4.52E-03
3.69E-03	1.06E-03	1.49E-03
7.10E-03	-1.51E-03	-2.60E-03
2.25E-04	8.54E-05	8.31E-05

sochrons

±σ	$^{36}Ar/^{40}Ar$	±σ
2.17E-04	2.61E-04	6.82E-05
4.28E-04	2.21E-04	1.43E-04
1.39E-04	1.04E-04	4.99E-05
9.52E-04	3.90E-04	3.86E-04
2.34E-03	8.04E-04	1.02E-03
3.69E-04	3.05E-04	1.17E-04
4.59E-04	-2.15E-05	-1.56E-04
7.02E-04	3.49E-04	2.87E-04

sochrons

±σ	$^{36}Ar/^{40}Ar$	±σ
-4.76E-02	-1.44E-03	-1.40E-02
1.46E-03	6.16E-04	5.75E-04
6.79E-04	8.94E-05	2.76E-04
7.80E-05	2.56E-04	1.93E-05
9.28E-05	2.67E-05	2.29E-05
6.45E-05	1.87E-05	1.48E-05
4.02E-04	4.27E-05	1.42E-04
3.13E-04	4.82E-06	1.17E-04
1.55E-04	-6.85E-06	-4.91E-05
6.46E-04	-1.53E-04	-2.33E-04

Burial and exhumation history of the Daday Unit (Central Pontides, Turkey): implications for the closure of the Intra-Pontide oceanic basin.

Frassi C., Marroni M., Pandolfi L., Göncüoğlu M. C., Ellero A., Ottria G., Sayit K., McDonald C. S., Balestrieri M. L., Malasoma A.

Sample: 8.7.11 | Lab #: 837-02 | *J* : 0.00106155 ± 0.00000481206

Material: White Mica

Irradiation coordinates: 14F7

N	Power (W)	^{40}Ar (moles)	^{40}Ar (ISO)[3] (cps)	±σ (cps)	^{40}Ar (PLT)[4] (cps)	±σ (cps)	^{39}Ar (cps)	±σ (cps)	^{38}Ar (cps)	±σ (cps)	^{37}Ar (cps)	±σ (cps)
A	4.0	5.33E-15	2.80E+05	1.82E+02	2.75E+05	4.15E+02	3.34E+03	1.01E+01	5.32E+00	1.71E+00	N.D.	5.89E+02
B	4.5	1.01E-14	5.28E+05	2.51E+02	5.26E+05	4.24E+02	6.11E+03	1.31E+01	2.62E+00	2.26E+00	N.D.	6.16E+02
C	5.0	9.66E-15	5.07E+05	2.22E+02	5.06E+05	4.25E+02	5.87E+03	1.31E+01	8.23E-01	2.27E+00	7.32E+02	6.03E+02
D	5.1	1.54E-15	8.06E+04	8.33E+01	8.02E+04	3.52E+02	9.30E+02	5.48E+00	N.D.	1.09E+00	1.32E+03	6.51E+02
E	5.2	8.44E-16	4.43E+04	6.65E+01	4.44E+04	3.70E+02	5.21E+02	4.20E+00	N.D.	1.07E+00	4.41E+02	6.09E+02
F	6.0	7.76E-16	4.07E+04	5.75E+01	4.06E+04	3.40E+02	4.73E+02	3.81E+00	5.04E-01	1.03E+00	N.D.	6.51E+02
G	7.0	6.24E-16	3.27E+04	5.12E+01	3.29E+04	3.28E+02	3.86E+02	3.73E+00	N.D.	7.86E-01	N.D.	6.03E+02
h	8.0	4.68E-16	2.46E+04	5.03E+01	2.41E+04	3.30E+02	2.82E+02	3.16E+00	4.95E-01	6.89E-01	3.28E+01	6.29E+02
I	8.5	2.82E-16	1.48E+04	4.25E+01	1.48E+04	3.37E+02	1.80E+02	2.40E+00	N.D.	7.01E-01	2.27E+02	6.16E+02
J	9.0	2.26E-16	1.19E+04	4.19E+01	1.18E+04	3.25E+02	1.36E+02	2.23E+00	6.51E-01	7.70E-01	N.D.	6.21E+02
K	11.0	2.51E-16	1.32E+04	4.28E+01	1.36E+04	3.35E+02	1.59E+02	2.60E+00	N.D.	7.35E-01	N.D.	5.95E+02
L	15.0	4.36E-16	2.29E+04	5.24E+01	2.33E+04	3.37E+02	2.73E+02	2.88E+00	N.D.	8.32E-01	N.D.	5.82E+02

Plateau Age (Steps B-L)

Sample: 8.7.11 | Lab #: 837-03 | J: 0.00106155 ± 0.00000481206

Material: White Mica

Irradiation coordinates: 14F7

N	Power (W)	^{40}Ar (moles)	^{40}Ar (ISO)[3] (cps)	±σ (cps)	^{40}Ar (PLT)[4] (cps)	±σ (cps)	^{39}Ar (cps)	±σ (cps)	^{38}Ar (cps)	±σ (cps)	^{37}Ar (cps)	±σ (cps)
A	3.5	3.51E-15	1.85E+05	1.32E+02	1.82E+05	3.77E+02	2.28E+03	7.86E+00	5.86E+00	1.45E+00	5.99E+02	6.50E+02
B	4.0	8.41E-15	4.44E+05	2.02E+02	4.42E+05	4.22E+02	5.15E+03	1.11E+01	1.67E+00	2.11E+00	3.20E+02	6.23E+02
C	4.3	6.29E-15	3.32E+05	1.62E+02	3.33E+05	3.66E+02	3.82E+03	9.15E+00	N.D.	1.82E+00	N.D.	6.10E+02
D	4.5	2.81E-15	1.48E+05	1.02E+02	1.49E+05	3.40E+02	1.73E+03	7.26E+00	N.D.	1.25E+00	N.D.	5.87E+02
E	4.8	6.33E-15	3.34E+05	1.22E+02	3.34E+05	3.64E+02	3.88E+03	9.95E+00	N.D.	1.92E+00	N.D.	6.24E+02
F	5.0	8.45E-16	4.45E+04	6.46E+01	4.58E+04	3.36E+02	5.30E+02	4.29E+00	N.D.	8.89E-01	N.D.	6.12E+02
G	5.5	6.17E-16	3.26E+04	5.06E+01	3.15E+04	3.60E+02	3.85E+02	3.61E+00	5.03E-01	9.23E-01	1.06E+03	6.29E+02
H	6.0	4.98E-16	2.62E+04	5.32E+01	2.58E+04	3.64E+02	3.07E+02	3.12E+00	N.D.	9.93E-01	1.30E+03	6.16E+02
I	7.5	5.20E-16	2.74E+04	4.97E+01	2.48E+04	3.65E+02	3.33E+02	2.84E+00	5.17E+00	9.07E-01	1.67E+03	6.43E+02
J	9.0	4.39E-16	2.32E+04	5.04E+01	2.16E+04	3.41E+02	2.81E+02	2.94E+00	3.57E+00	8.69E-01	N.D.	6.52E+02

K	11.0	3.73E-16	1.97E+04	5.13E+01	1.98E+04	3.22E+02	2.39E+02	2.74E+00	3.82E+00	8.68E-01	1.08E+03	6.38E+02
L	15.0	3.03E-16	1.60E+04	4.27E+01	1.59E+04	3.38E+02	1.91E+02	2.94E+00	1.56E-01	8.08E-01	6.79E+02	6.11E+02

Plateau Age (Steps D-F)

Standards: HD-B1 | Lab #: 831 | Age: 24.18 Ma

Irradiation coordinates: 14F1

N	Power (W)	^{40}Ar (moles)	^{40}Ar (cps)	±σ (cps)	^{39}Ar (cps)	±σ (cps)	^{38}Ar (cps)	±σ (cps)	^{37}Ar (cps)	±σ (cps)	^{36}Ar (cps)	±σ (cps)
1	5.0	3.30E-16	1.05E+04	6.44E+01	5.15E+02	6.32E+00	5.58E+00	1.36E+00	1.40E+02	6.39E+02	1.19E+01	1.74E+00
2	5.0	4.06E-16	1.29E+04	6.63E+01	8.06E+02	7.26E+00	1.07E+01	1.36E+00	7.92E+02	7.79E+02	8.41E+00	1.70E+00
3	5.0	1.85E-15	5.88E+04	8.66E+01	4.07E+03	1.34E+01	5.56E+01	2.21E+00	-3.47E+01	6.90E+02	1.82E+01	1.74E+00
4	5.0	3.34E-15	1.06E+05	9.84E+01	7.19E+03	1.63E+01	1.01E+02	2.29E+00	-2.90E+02	7.27E+02	4.69E+01	1.86E+00
5	5.0	1.97E-15	6.26E+04	8.92E+01	4.62E+03	1.34E+01	6.30E+01	1.38E+00	1.15E+03	6.47E+02	1.24E+01	1.67E+00

Weighted mean *J* : 0.00104950 ± 0.0000049113

Standards: HD-B1 | Lab #: 833 | Age: 24.18 Ma

Irradiation coordinates: 14F3

N	Power (W)	^{40}Ar (moles)	^{40}Ar (cps)	±σ (cps)	^{39}Ar (cps)	±σ (cps)	^{38}Ar (cps)	±σ (cps)	^{37}Ar (cps)	±σ (cps)	^{36}Ar (cps)	±σ (cps)
1	5.0	1.97E-14	6.27E+05	2.92E+02	4.72E+04	4.12E+01	6.09E+02	4.85E+00	N.D.	7.43E+02	2.58E+01	1.80E+00
2	5.0	1.13E-14	3.60E+05	2.02E+02	2.68E+04	3.02E+01	3.47E+02	3.27E+00	1.02E+03	6.97E+02	5.36E+01	1.90E+00
3	5.0	7.55E-15	2.40E+05	1.52E+02	1.86E+04	2.62E+01	2.39E+02	3.00E+00	N.D.	5.86E+02	1.98E+01	1.58E+00
4	5.0	5.69E-15	1.81E+05	1.27E+02	1.36E+04	2.23E+01	1.77E+02	2.89E+00	N.D.	6.08E+02	2.58E+01	1.72E+00
5	5.0	4.47E-15	1.42E+05	1.38E+02	1.06E+04	1.93E+01	1.39E+02	2.38E+00	6.91E+02	6.43E+02	1.67E+01	1.69E+00

Weighted mean *J* : 0.00104470 ± 0.0000099887

Standards: HD-B1 | Lab #: 835 | Age: 24.18 Ma

Irradiation coordinates: 14F5

N	Power (W)	^{40}Ar (moles)	^{40}Ar (cps)	±σ (cps)	^{39}Ar (cps)	±σ (cps)	^{38}Ar (cps)	±σ (cps)	^{37}Ar (cps)	±σ (cps)	^{36}Ar (cps)	±σ (cps)
1	5.0	4.95E-15	1.57E+05	1.42E+02	1.16E+04	2.75E+01	1.49E+02	1.53E+00	N.D.	1.06E+02	3.38E+01	1.18E+00
2	5.0	2.07E-14	6.57E+05	4.30E+02	4.93E+04	6.13E+01	6.36E+02	3.11E+00	N.D.	9.96E+01	1.14E+02	1.64E+00
3	5.0	3.85E-15	1.22E+05	1.02E+02	9.27E+03	1.96E+01	1.20E+02	1.42E+00	N.D.	1.02E+02	1.25E+01	1.03E+00
4	5.0	2.07E-15	6.56E+04	7.47E+01	4.63E+03	1.34E+01	6.98E+01	2.04E+00	1.20E+01	6.40E+02	1.89E+01	1.85E+00

5	5.0	7.03E-15	2.23E+05	1.72E+02	1.63E+04	2.53E+01	2.19E+02	2.97E+00	5.12E+02	7.40E+02	5.19E+01	1.81E+00

Weighted mean J : 0.00106520 ± 0.0000013385

Explanations

D[1]: Mass discrimination per AMU based on power law

Blank Type[2]: Ave = average; LR = linear regression versus time

^{40}Ar (ISO)[3] - non air corrected 40Ar for isochron calculations

^{40}Ar (PLT)[4] - Air corrected 40Ar for plateau calculations

N.D. : values are indistinguishable from the background measurements

Constants Used

Atmospheric argon ratios

$(^{40}Ar/^{36}Ar)_A$	295.5 ± 0.50	Nier (1950)
$(^{40}Ar/^{38}Ar)_A$	0.1880 ± 0.0001	Nier (1950)

Interfering isotope production ratios

$(^{40}Ar/^{39}Ar)_K$	(7.30 ± 0.90)E-04
$(^{38}Ar/^{39}Ar)_K$	(1.22 ± 0.00)E-02
$(^{37}Ar/^{39}Ar)_K$	(2.24 ± 0.16)E-04
$(^{39}Ar/^{37}Ar)_{Ca}$	(6.95 ± 0.09)E-04
$(^{38}Ar/^{37}Ar)_{Ca}$	(1.96 ± 0.08)E-05
$(^{36}Ar/^{37}Ar)_{Ca}$	(2.65 ± 0.02)E-04
$(^{36}Cl/^{38}Cl)_{Cl}$	263 ± 2

Decay Constants

$^{40}K\ \lambda_\varepsilon$	(5.81 ± 0.17)E-11	Steiger & Jäger, 1977
$^{40}K\ \lambda_\beta$	(4.96 ± 0.08)E-10	Steiger & Jäger, 1977
^{39}K	(2.58)E-3 a^{-1}	Stoenner et al. (1965)
^{37}K	7.232 a^{-1}	Stoenner et al. (1965)
$^{36}Cl\ \lambda_\beta$	(2.305)E-6 a^{-1}	Endt (1998)

D^{1} : 0.986139 ± 0.000340 Heating: 10 s

										Blank Corrections			
^{36}Ar (cps)	±σ (cps)	$\%^{40}Ar^*$	$^{40}Ar^*/^{39}Ar_K$	±σ	Age (Ma)	±σ (Ma)	±2σ (Ma)	±σ (-J) (Ma)	Ca/K	Blank Type[2]	^{40}Ar (cps)	±σ (cps)	^{39}Ar (cps)
1.61E+01	1.26E+00	98.2	82.29000	0.27712	149.93	0.67	1.34	0.48	-0.03	LR	7.94E+03	2.57E+01	2.12E+01
6.29E+00	1.16E+00	99.6	86.20000	0.19698	156.76	0.59	1.18	0.34	-0.12	LR	7.68E+03	2.57E+01	2.11E+01
4.56E+00	1.23E+00	99.7	86.22000	0.20509	156.80	0.60	1.20	0.36	0.27	LR	7.55E+03	2.57E+01	2.10E+01
1.30E+00	1.16E+00	99.5	86.20000	0.63316	156.76	1.20	2.40	1.10	2.71	LR	7.16E+03	2.65E+01	2.11E+01
-3.15E-01	1.23E+00	100.1	85.20000	0.98784	155.02	1.79	3.58	1.72	1.56	LR	7.03E+03	2.65E+01	2.12E+01
3.93E-01	1.13E+00	99.7	85.76000	0.99694	155.99	1.80	3.60	1.74	0.16	LR	6.97E+03	2.65E+01	2.13E+01
-3.59E-01	1.10E+00	100.3	85.12000	1.18257	154.87	2.12	4.24	2.06	-0.66	LR	7.35E+03	2.26E+01	2.01E+01
1.81E+00	1.10E+00	98.2	85.45000	1.51246	155.45	2.68	5.36	2.64	0.25	LR	7.15E+03	2.26E+01	2.04E+01
-2.12E-01	1.13E+00	100.3	82.57000	2.17511	150.43	3.83	7.66	3.80	1.98	LR	7.05E+03	2.26E+01	2.05E+01
1.47E-01	1.09E+00	98.5	87.02000	2.79189	158.19	4.88	9.76	4.86	-2.75	LR	6.73E+03	2.31E+01	2.02E+01
-1.41E+00	1.13E+00	101.7	85.63000	2.53819	155.77	4.45	8.90	4.42	-2.91	LR	6.67E+03	2.31E+01	1.99E+01
-1.31E+00	1.13E+00	100.2	85.29000	1.52428	155.18	2.70	5.40	2.66	-0.93	LR	6.54E+03	2.31E+01	1.94E+01
					156.66	**0.46**	**0.92**						

D^{1} : 0.984617 ± 0.0003576 Heating: 10 s

										Blank Corrections			
^{36}Ar (cps)	±σ (cps)	$\%^{40}Ar^*$	$^{40}Ar^*/^{39}Ar_K$	±σ	Age (Ma)	±σ (Ma)	±2σ (Ma)	±σ (-J) (Ma)	Ca/K	Blank Type[2]	^{40}Ar (cps)	±σ (cps)	^{39}Ar (cps)
1.06E+01	1.20E+00	98.3	80.03000	0.32195	145.98	0.72	1.44	0.56	0.51	LR	7.99E+03	2.49E+01	2.12E+01
7.30E+00	1.25E+00	99.5	85.87000	0.20181	156.19	0.59	1.18	0.35	0.15	LR	7.99E+03	2.49E+01	2.13E+01
-1.85E+00	1.11E+00	100.1	87.15000	0.23002	158.42	0.63	1.26	0.40	-0.38	LR	7.99E+03	2.49E+01	2.13E+01
-3.41E+00	1.10E+00	100.6	86.57000	0.41401	157.40	0.87	1.74	0.72	-0.69	LR	7.61E+03	2.38E+01	2.15E+01
-4.20E-03	1.16E+00	99.9	85.92000	0.23922	156.27	0.63	1.26	0.42	-0.29	LR	7.42E+03	2.38E+01	2.15E+01
-4.31E+00	1.12E+00	102.6	86.50000	0.94499	157.28	1.71	3.42	1.65	-3.27	LR	7.03E+03	2.38E+01	2.16E+01
3.76E+00	1.20E+00	97.2	81.66000	1.20593	148.83	2.16	4.32	2.11	4.61	LR	7.20E+03	2.49E+01	1.97E+01
1.45E+00	1.22E+00	98.4	84.16000	1.46321	153.21	2.60	5.20	2.55	7.24	LR	7.11E+03	2.49E+01	1.94E+01
8.85E+00	1.22E+00	91.1	74.53000	1.26731	136.32	2.27	4.54	2.23	8.52	LR	6.92E+03	2.49E+01	1.89E+01
5.33E+00	1.14E+00	94.4	76.78000	1.45403	140.27	2.59	5.18	2.56	-5.77	LR	6.71E+03	2.45E+01	1.85E+01

-5.40E-01	1.08E+00	101.8	83.20000	1.65529	151.53	2.93	5.86	2.89	7.73	LR	6.68E+03	2.45E+01	1.89E+01
2.96E-01	1.13E+00	99.2	83.22000	2.17854	151.56	3.83	7.66	3.81	6.09	LR	6.65E+03	2.45E+01	1.93E+01
					156.59	**0.71**	**1.42**						

D^{1}: 0.9977846 Heating: 10 s

%^{40}Ar*	^{40}Ar*/^{39}Ar$_K$ ±σ		J	±σ	Ca/K	Blank Type[2]	^{40}Ar (cps)	±σ (cps)	^{39}Ar (cps)	±σ (cps)	^{38}Ar (cps)	±σ (cps)
66.4	13.49864	1.02768	9.9960E-04	########	0.48	LR	8.63E+03	5.99E+01	2.54E+02	2.98E+00	1.47E+01	9.21E-01
81.2	12.97701	0.64692	1.0398E-03	########	1.76	LR	8.48E+03	5.79E+01	2.55E+02	3.10E+00	1.37E+01	8.91E-01
90.8	13.08874	0.13613	1.0309E-03	########	-0.02	LR	8.39E+03	5.79E+01	2.52E+02	3.10E+00	1.38E+01	8.91E-01
86.9	12.81535	0.08346	1.0529E-03	########	-0.08	LR	8.20E+03	3.59E+01	2.51E+02	3.45E+00	1.46E+01	8.81E-01
94.3	12.74341	0.11505	1.0588E-03	########	0.44	LR	8.20E+03	3.59E+01	2.54E+02	3.45E+00	1.51E+01	8.81E-01

D^{1}: 0.9980028 Heating: 10 s

%^{40}Ar*	^{40}Ar*/^{39}Ar$_K$ ±σ		J	±σ	Ca/K	Blank Type[2]	^{40}Ar (cps)	±σ (cps)	^{39}Ar (cps)	±σ (cps)	^{38}Ar (cps)	±σ (cps)
98.8	13.08368	0.01735	1.0313E-03	#########	0.00	LR	9.00E+03	3.73E+01	2.56E+02	3.36E+00	1.34E+01	9.31E-01
95.6	12.81752	0.02669	1.0527E-03	#########	0.07	LR	8.84E+03	3.73E+01	2.57E+02	3.36E+00	1.34E+01	9.31E-01
97.5	12.52863	0.03179	1.0770E-03	#########	-0.01	LR	8.50E+03	3.73E+01	2.58E+02	3.36E+00	1.35E+01	9.31E-01
95.7	12.73508	0.04411	1.0595E-03	#########	-0.14	LR	8.47E+03	7.51E+01	2.59E+02	3.52E+00	1.31E+01	9.28E-01
96.6	12.89272	0.05438	1.0466E-03	#########	0.11	LR	8.61E+03	7.51E+01	2.59E+02	3.52E+00	1.26E+01	9.28E-01

D^{1}: 0.9966905 ± 0.0003579 Heating: 10 s

%^{40}Ar*	^{40}Ar*/^{39}Ar$_K$ ±σ		J	±σ	Ca/K	Blank Type[2]	^{40}Ar (cps)	±σ (cps)	^{39}Ar (cps)	±σ (cps)	^{38}Ar (cps)	±σ (cps)
93.6	12.62367	0.04422	1.0689E-03	#########	-0.01	LR	3.94E+03	2.10E+01	8.45E+02	5.13E+00	2.31E+00	2.86E-01
94.9	12.63119	0.02119	1.0682E-03	#########	-0.01	LR	6.09E+03	3.29E+01	9.62E+02	6.71E+00	4.11E+00	4.63E-01
97.0	12.77003	0.04408	1.0566E-03	#########	-0.03	LR	1.07E+04	3.29E+01	1.20E+03	6.71E+00	8.12E+00	4.63E-01
91.5	12.94470	0.12556	1.0424E-03	#########	0.00	LR	9.27E+03	4.06E+01	2.60E+02	3.43E+00	1.34E+01	9.40E-01

93.1	12.70961	0.03981	1.0617E-03	#########	0.05	LR		9.11E+03	4.06E+01	2.60E+02	3.43E+00	1.32E+01	9.40E-01

Ratios for Isochrons

±σ (cps)	^{38}Ar (cps)	±σ (cps)	^{37}Ar (cps)	±σ (cps)	^{36}Ar (cps)	±σ (cps)	^{39}Ar/^{40}Ar	±σ	^{36}Ar/^{40}Ar	±σ
9.48E-01	5.56E+00	6.24E-01	7.42E+01	2.20E+00	3.00E+01	8.44E-01	1.19E-02	3.68E-05	5.76E-05	4.51E-06
9.48E-01	5.32E+00	6.24E-01	7.34E+01	2.20E+00	2.86E+01	8.44E-01	1.16E-02	2.53E-05	1.19E-05	2.19E-06
9.48E-01	5.20E+00	6.24E-01	7.30E+01	2.20E+00	2.80E+01	8.44E-01	1.16E-02	2.62E-05	8.99E-06	2.42E-06
8.95E-01	5.16E+00	6.63E-01	7.10E+01	2.24E+00	2.69E+01	7.83E-01	1.15E-02	6.91E-05	1.61E-05	1.43E-05
8.95E-01	5.36E+00	6.63E-01	6.98E+01	2.24E+00	2.70E+01	7.83E-01	1.18E-02	9.65E-05	-7.11E-06	-2.78E-05
8.95E-01	5.46E+00	6.63E-01	6.92E+01	2.24E+00	2.71E+01	7.83E-01	1.16E-02	9.51E-05	9.66E-06	2.79E-05
9.59E-01	5.83E+00	4.56E-01	6.78E+01	2.39E+00	2.75E+01	7.98E-01	1.18E-02	1.15E-04	-1.10E-05	-3.35E-05
9.59E-01	5.72E+00	4.56E-01	6.83E+01	2.39E+00	2.64E+01	7.98E-01	1.14E-02	1.30E-04	7.34E-05	4.48E-05
9.59E-01	5.66E+00	4.56E-01	6.85E+01	2.39E+00	2.58E+01	7.98E-01	1.22E-02	1.66E-04	-1.44E-05	-7.65E-05
9.88E-01	5.79E+00	5.36E-01	6.99E+01	2.32E+00	2.54E+01	8.12E-01	1.14E-02	1.93E-04	1.24E-05	9.21E-05
9.88E-01	5.91E+00	5.36E-01	7.04E+01	2.32E+00	2.57E+01	8.12E-01	1.20E-02	2.01E-04	-1.07E-04	-8.55E-05
9.88E-01	6.14E+00	5.36E-01	7.14E+01	2.32E+00	2.64E+01	8.12E-01	1.19E-02	1.28E-04	-5.71E-05	-4.91E-05

Ratios for Isochrons

±σ (cps)	^{38}Ar (cps)	±σ (cps)	^{37}Ar (cps)	±σ (cps)	^{36}Ar (cps)	±σ (cps)	^{39}Ar/^{40}Ar	±σ	^{36}Ar/^{40}Ar	±σ
8.18E-01	6.40E+00	5.17E-01	7.02E+01	2.31E+00	3.09E+01	8.19E-01	1.23E-02	4.33E-05	5.71E-05	6.45E-06
8.18E-01	6.58E+00	5.17E-01	7.16E+01	2.31E+00	3.11E+01	8.19E-01	1.16E-02	2.54E-05	1.64E-05	2.83E-06
8.18E-01	6.68E+00	5.17E-01	7.22E+01	2.31E+00	3.11E+01	8.19E-01	1.15E-02	2.81E-05	-5.56E-06	-3.35E-06
8.08E-01	6.74E+00	5.76E-01	7.31E+01	2.41E+00	3.04E+01	8.09E-01	1.16E-02	4.96E-05	-2.30E-05	-7.39E-06
8.08E-01	6.68E+00	5.76E-01	7.29E+01	2.41E+00	3.00E+01	8.09E-01	1.16E-02	3.01E-05	-1.26E-08	-3.47E-06
8.08E-01	6.56E+00	5.76E-01	7.24E+01	2.41E+00	2.92E+01	8.09E-01	1.19E-02	9.77E-05	-9.68E-05	-2.51E-05
8.48E-01	4.76E+00	6.55E-01	6.72E+01	2.34E+00	2.53E+01	9.00E-01	1.18E-02	1.12E-04	1.15E-04	3.70E-05
8.48E-01	3.96E+00	6.55E-01	6.70E+01	2.34E+00	2.41E+01	9.00E-01	1.17E-02	1.21E-04	5.53E-05	4.64E-05
8.48E-01	2.38E+00	6.55E-01	6.66E+01	2.34E+00	2.17E+01	9.00E-01	1.21E-02	1.06E-04	3.22E-04	4.46E-05
8.64E-01	1.53E+00	5.59E-01	6.62E+01	2.30E+00	2.02E+01	7.52E-01	1.21E-02	1.29E-04	2.30E-04	4.93E-05

8.64E-01	2.99E+00	5.59E-01	6.61E+01	2.30E+00	2.22E+01	7.52E-01	1.21E-02	1.43E-04	-2.74E-05	-5.47E-05
8.64E-01	4.44E+00	5.59E-01	6.60E+01	2.30E+00	2.41E+01	7.52E-01	1.20E-02	1.86E-04	1.85E-05	7.08E-05

^{37}Ar (cps)	±σ (cps)	^{36}Ar (cps)	±σ (cps)
3.55E+02	5.67E+00	5.63E+01	1.25E+00
3.51E+02	5.68E+00	5.46E+01	1.35E+00
3.49E+02	5.68E+00	5.36E+01	1.35E+00
3.48E+02	4.78E+00	5.17E+01	1.35E+00
3.50E+02	4.78E+00	5.16E+01	1.35E+00

^{37}Ar (cps)	±σ (cps)	^{36}Ar (cps)	±σ (cps)
3.58E+02	5.01E+00	5.55E+01	1.21E+00
3.57E+02	5.01E+00	5.42E+01	1.21E+00
3.57E+02	5.01E+00	5.17E+01	1.21E+00
3.54E+02	4.97E+00	5.18E+01	1.26E+00
3.51E+02	4.97E+00	5.32E+01	1.26E+00

^{37}Ar (cps)	±σ (cps)	^{36}Ar (cps)	±σ (cps)
2.85E+02	4.10E+00	1.39E+01	6.83E-01
2.84E+02	4.13E+00	1.59E+01	8.00E-01
2.81E+02	4.13E+00	2.13E+01	8.00E-01
3.46E+02	5.68E+00	5.73E+01	1.31E+00

3.41E+02	5.68E+00	5.66E+01	1.31E+00

Geological Magazine

Supplementary Material

Burial and exhumation history of the Daday Unit (Central Pontides, Turkey): implications for the closure of the Intra-Pontide oceanic basin.

Frassi C., Marroni M., Pandolfi L., Göncüoğlu M. C., Ellero A., Ottria G., Sayit K., McDonald C. S., Balestrieri M. L., Malasoma A.

Supplementary Table S7. Apatite Fission-track data

Sample	ρ_d	ρ_s	ρ_i	n_g	$P(\chi^2)$	**Central Age±1σ**	U	MTL±1σ	MTL *c*-axis±1σ	s.d.	n_{Tints}	Dpar	s.d.
	n_d	n_s	n_i		(%)	**(Ma)**	(μg/g)	(μm)	(μm)	(μm)		(μm)	(μm)
FT4	7.16 5612	3.24 476	7.32 1076	27	96.7	**57.7±3.8**	12.2	14.1±0.2	14.9±1.0	1.6	50	1.9(80)	0.42
FT6	7.63 5612	10.8 321	24.3 722	23	83.7	**58.0±4.4**	43.7	13.5±1.4	14.4±1.0	1.4	99	2.0(98)	0.33

FT4: garnet-bearing micaschist
FT6: metarenite

Notes: Ages determined by external detector method using a zeta value $\zeta = 360 \pm 11$ for dosimeter CN5 (referred to Fish Canyon Tuff and Durango apatite standards, Hurford, 1990. ρ_d, ρ_i: standard and induced track densities measured on mica external detectors; ρ_s: spontaneous track densities on internal mineral surfaces, track densities are given in 10^5 tracks cm^{-2}; n_d, n_i and n_s: number of tracks on external detectors and on mineral surfaces; n_g: number of counted mineral grains; $P(\square^2)$: ($\square^2$) probability (Galbraith, 1981); Central age calculated using TRACKKEY program (Dunkl, 2002); MTL: mean length of confined tracks length distribution ± standard error, s.d.: standard deviation, n_{TINTs}: number of measured lengths; only TINTs (tracks reached by the etching because they intercept a surface track, Bhandari et al., 1971) were measured. MTL c-axis: mean length of the distribution of measured confined track lengths normalized for track angle using c-axis projection (Ketcham et al., 2007a, 2009); Dpar: mean etch pit diameter parallel to the *c*-axis and number of total measured Dpar for sample standard.